Influence of the nature of fibrinogen on the structure and mechanics of fibrin clots

Xabel Garcia Gonzalez

Communauté
UNIVERSITÉ Grenoble Alpes

THÈSE

Pour obtenir le grade de

DOCTEUR DE LA COMMUNAUTÉ UNIVERSITÉ GRENOBLE ALPES

Spécialité : **Mécanique des Fluides, Procédés, Energétique**

Arrêté ministériel : 25 mai 2016

Présentée par

Xabel GARCÍA GONZÁLEZ

Thèse dirigée par **Benoît POLACK** et
codirigée par **François CATON**

préparée au sein du **Laboratoire Rhéologie et Procédés UMR 5520**
dans **l'École Doctorale Ingénierie - Matériaux, Mécanique, Environnement, Energétique, Procédés, Production**

Influence de la nature du fibrinogène sur la structure et la mécanique du caillot de fibrine

Thèse soutenue publiquement le **14 décembre 2016,**
devant le jury composé de :

M. Robert PEYROUX
CR, Université de Grenoble Alpes, Président
M. Philippe de MAZANCOURT
PUPH, Université de Versailles Saint Quentin, Rapporteur
M. Xiong WANG
PU, Université de Lorraine, Rapporteur
M. Jean-François PALIERNE
CR1, ENS-Lyon, Membre
M. François CATON
CR1, Université de Grenoble Alpes, Co-Directeur
M. Benoît POLACK
PU, Université de Grenoble Alpes, Directeur

Index

Chapter 2

Introduction

The polymerization of fibrinogen monomers into fibrin to form a clot is an essential biological process that insures the stopping of bleeding in case of damaged blood vessels.

Figure 1. Schematic of a clot formed by red cells embedded in the fibrin network

The importance of blood coagulation, and in particular of the fibrin clot, resides in the maintenance of an equilibrium. On the one hand, fibres must be resistant enough to avoid the excessive bleeding caused by a haemorrhage and to withstand mechanical perturbations such as blood flow at the site of vascular injury. On the other hand, excessive coagulation may obstruct blood flow through the circulatory system, *i.e.* the formation of a thrombus. Abnormal clots which disrupt normal blood flow cause deprivation of oxygen to a tissue, which can lead to its death, also known as infarction.

The mechanical properties of such clots should also determine if they could break free and migrate in the circulation, forming an embolus. This embolus may obstruct an artery in the lung (pulmonary embolism), the heart (myocardial infarction), in the brain (stroke) or a peripheral artery in a limb (distal embolism). Therefore, the determination

and modelling of the relation between the structure of fibrin clots and their rheological properties is of great importance.

Fibrin clot formation has been studied since the XVIIIth century and the properties of fibrin clots are closely related to various genetic and environmental factors such as pH, temperature or ionic strength. Moreover, these factors influence not only the structure of fibrin and its function, but are also related with thrombotic diseases. However, several aspects of fibrin polymerization (such as lateral aggregation) and the mechanical properties of fibrin clots are not yet well understood.

It has been suggested that among the mentioned factors that influence fibrin structure and its mechanical properties, fibrinogen itself plays a major role. The aim of this thesis is to explore the influence of different physicochemical properties of fibrinogen, as well as the multi-scale structure and mechanical properties of fibrin.

First, we recapitulate the current understanding on the structure and mechanical properties of fibrin and the experimental techniques available to investigate them, focusing on the description of the experimental setups implemented to carry out this work (Chapters 1 and 2). Second, we investigate the role of fibrinogen on fibrin properties by using three different commercial fibrinogen sources. We determine the physicochemical disparities between the fibrinogens and we investigate whether or not they are responsible for the observed differences on fibrin structures in purified and plasmatic systems (Chapters 3 and 4). We then investigate the consequences of the different fibrinogen sources on the linear and nonlinear rheological properties of fibrin clots as well as the rupture scenarios of those clots (Chapter 5). Finally, we investigate if that the structural method used to characterize the fibre's nanostructure possess all the necessary characteristics to become a clinical structural biomarker for fibrin (Annex).

Chapter 1

State of the Art

In this chapter we describe briefly the coagulation mechanisms in the haemostatic processes and the factors that control it. We also review the current knowledge relative to the structure of the molecule of fibrinogen, its polymerization into fibrin fibres and the clot destruction during fibrinolysis. Finally, we discuss the actual state of the art concerning the mechanical properties of fibrin clot

1 Introduction

After wounding, the haemostatic system has for purpose to seal off and allow repairing of the damaged vasculature as well as the surrounding issue. Figure 2 illustrates the polymerization process and the length-scales concerned.

In the classical view of fibrin polymerization, the activation of fibrin monomers by thrombin leads to the formation of fibrin protofibrils. These protofibrils then aggregate laterally to form fibrin fibres which branch together to form a three dimensional network.

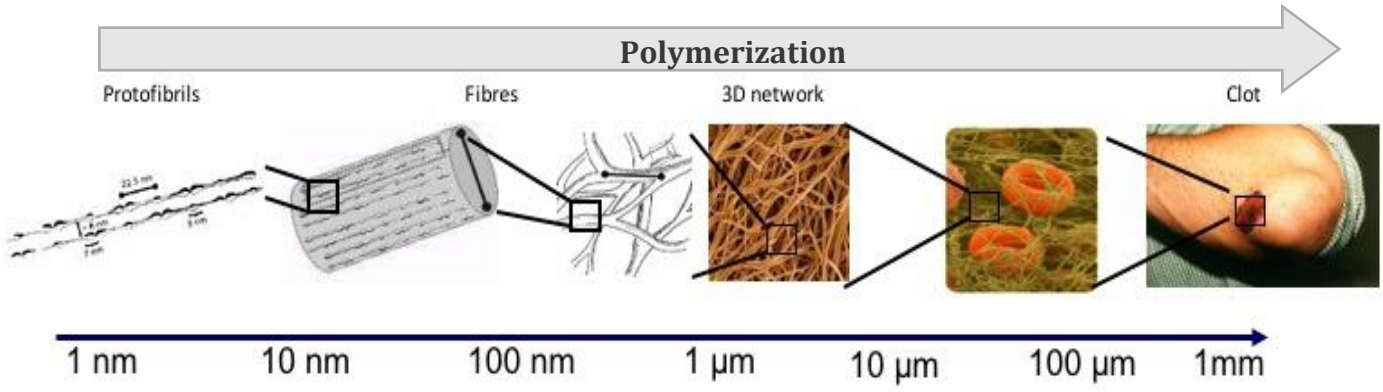

Figure 2. Fibrin clot from the nanometre to the millimetre. From left to right they are illustrated the longitudinal aggregation of fibrin monomers, the lateral aggregation of protofibrils to form a fibre, the three-dimensional network of fibres formed to seal off the damaged zone and the general view of a clot

2 Various phases of coagulation

Haemostasis enables an organism to close off damaged blood vessels, keep the blood in a fluid state and, finally, remove the blood clots after restoration of vascular integrity. The haemostatic system is a highly refined machinery in which blood clotting, also referred to as coagulation, has a prominent role [1].

There are two main components of haemostasis that happen simultaneously and are mechanistically intertwined. Primary haemostasis refers to platelet aggregation, that adhere to the site of injury and to each other, and platelet plug formation. Secondary haemostasis or coagulation refers to the deposition of insoluble fibrin generated by the proteolytic coagulation cascade (*cf.* Figure 3). This leads to the formation of a mesh that

is incorporated into and around the platelet plug to strengthen and stabilize the blood clot. The fibrinolysis pathway also plays a very significant role in haemostasis. The fibrinolytic system has to dissolve blood clots during the process of wound healing and, as well, has to prevent blood clots in healthy blood vessels [2].

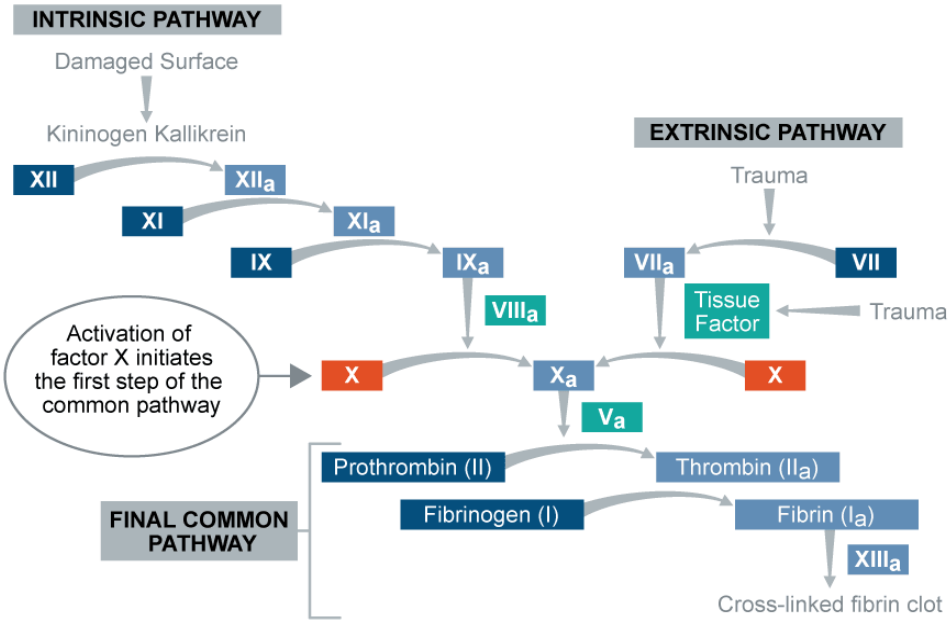

Figure 3. The coagulation cascade activates thrombin yielding fibrin monomers (Image from Coagadex)

3 Polymerization conditions

Henschen estimated that *"in healthy individuals, fibrinogen occurs in more than one million non-identical forms because of the many possible combinations of variations and the various form may show considerable differences in their functional properties*" [3]. Under physiological conditions, clot formation is a balance between fibrin development and crosslinking on one side, and fibrin degradation on the other. Structural conditions of fibrin clots may tip the scale against the formation of fibrin clots more resistant to fibrinolysis. This has major implications for thrombolytic therapy.

Fibrin clot formation depends on many factors. It is strongly influenced by alterations on environmental conditions such as the concentration of reagents [4], temperature, pH or ionic strength [5–7]. The physiological clotting conditions are the following:

$$7.32 < pH_{blood} < 7.42$$

$$36°C < T_{blood} < 37.5°C$$

$$280mOsm < Ionic\ Strength_{blood} < 300mOsm$$

$$2\ mg/ml < [Fibrinogen] < 4\ mg/ml$$

Many studies have been performed in order to investigate the modifications of the clotting process. Various molecules have been added to *in vitro* systems to determine their polymerization effects. Examples like calcium, dextran, albumin or aspirin are known to be able of changing clot properties. However, it is not known specifically which plasma components are responsible for the modulation of fibrin clots structure.

4 First discoveries: from antiquity until 1943

Hippocrates, Aristotle, and Galen were fully aware of the fact that freshly drawn blood usually clots within minutes. They described in detail many internal and superficial bleeding tendencies. A common observation was that blood congealed on cooling. It was thought that by leaving a wound in contact with air, the blood cooled, stopping the haemorrhage. However, they did not associate yet blood coagulability with a concept of haemostasis.

It was about two thousand years later, in the 1720's, when a French surgeon named Jean-Louis Petit noted that haemostasis after amputation of a limb was caused by blood clots forming in the vessels. In 1828, Fredrich Hopff noted that the well-known at the time familial bleeding tendency in males was associated with pronounced hypo-coagulability, which is now recognized as haemophilia [8].

Therefore, the recognition that coagulability was essential to prevent bleeding led to a massive increase in haemostasis research. In 1825, Buchanan compared blood

coagulation with milk, concluding that clots originate from a ferment and a protein. Later, in 1859, Denis proved that fibrin cannot exist in blood in the form of a liquid isomer, but in the form of a precursor of different characteristics: the concepts of *fibrinogen* and its polymerization into fibrin were then introduced.

Hammarsten first precipitated fibrinogen from blood plasma by half saturating it with respect to sodium chloride. This method has ever since been the classical procedure in the preparation of fibrinogen [9]. Hammarsten proved also that fibrinogen is the only protein that leads to the formation of fibrin under the enzymatic action of another protein: *thrombin*.

These advances led, in 1905, to the classic theory of coagulation described by Morawitz, who assembled four *coagulation factors* in a scheme of coagulation. Morawitz proposed that thrombin is activated by prothrombin in presence of other secreted substances by blood cells (platelets). This classic theory persisted for over 40 years.

The first microscopic investigations of the formation of fibrin structure were made in 1914 by Howell [10]. He observed the network structure of fibrin and studied the latter phases of fibrinogen-fibrin conversion with dark field illumination using a light microscopy. Howell described the end product as a "*meshwork of beautiful needles"*. Before the arrival of the electron microscopy, other light microscopy studies were performed by Mayer (1907), Cesana (1908) or Barrat (1920) for instance.

The modern understanding of the biochemical and physicochemical processes involving blood coagulation began in 1940's when several other coagulation factors were discovered. Also, fibrinogen became more available thanks to the application of plasma fractionation at large scales to produce it. Many studies have been realized in order to understand the polymerization mechanism of fibrinogen into fibrin fibres and the structure of these fibres. Here we list some of the main techniques used for the characterization of fibrinogen and fibrin:

- Chromatography and electrophorese
- Microscopy
- Light Scattering
- Turbidimetry
- X-ray and Neutron Scattering
- Rheology

Nowadays, the crystalline structure of the molecule of fibrinogen and fibrin fragments is mostly well known. However, there exists a lack of knowledge in the polymerization process of fibrin, especially on the lateral aggregation of protofibrils, and also in the relation of the ultrastructure of fibrin and the mechanical properties of the clots. Next, we resume the current knowledge on fibrinogen and fibrin ultrastucture and the mechanical properties of gels.

5 Fibrinogen structure

Fibrinogen, also named factor I (FI) in the clotting cascade (*cf.* Figure 3), is a fibrous adhesive glycoprotein represented on Figure 4. It is present in the plasma at concentrations ranging from 2 to 4 mg/ml (normal range). This protein is crucial in haemostasis because it is the precursor of fibrin monomers and it has an essential role in platelet aggregation and wound healing.

The structure of the molecule of fibrinogen has been extensively studied since the 1940s. X-ray scattering [11] and hydrodynamic studies [12,13] showed that fibrinogen is a fibrous centrosymetric protein of high molecular mass (=340kDa). Its structure is constituted by three aligned domains. The central part of the molecule (E-region) is slightly smaller (*c.a.* 5nm of diameter) while the exterior regions (D-regions) present a 6nm diameter to form a structure about 45nm in length. This was later confirmed by

Torbet's birefringence and diffraction studies [14,15]. Diffraction studies showed also that the three domains are attached by two coiled coils.

Electrophorese studies made by Henschen in 1964 [16] isolated three different peptide chains (noted as α, β and γ) with molar masses between 48 and 70 kDa. This suggests that fibrinogen is a dimeric molecule composed of three pairs of grouped chains in these two helical coiled-coil structures.

The whole amino-acid sequence of fibrinogen chains was determined by Lottspeich *et al*. and Doolittle *et al*. [17,18] confirming the total molar mass of the molecule of 340kDa as mentioned before. These studies gave also information about the existence of cleavable fibrinopeptides pairs (Fps A and B) in both extremities of α- and β-chains. The nomenclature used for fibrinogen (Aα, Bβ, $\gamma)_2$ arises from the combination of chains and peptides that are cleaved by thrombin to yield fibrin monomer, designated as $(\alpha, \beta, \gamma)_2$.

The cleavage of the two fibrinopeptide pairs localized in the central region of the molecule results in the beginning of the polymerization of fibrinogen into a network of fibrin fibres [19].

X-ray crystallographic studies have been performed during the last several years in order to report many structures of fibrinogen and fibrin fragments. This has provided a basis for a detailed model of the fibrinogen molecule and also fibrin protofibrils.

The multi-domain molecule of fibrinogen is considered as disordered. Crystallisation of a molecule like fibrinogen can be a problem because these molecules may not adopt the regular and periodic arrangements that are the key of the crystal lattice. Snipping the protein into core domains more compact and amenable to crystallization has been the main approach to reach success in the protein characterization.

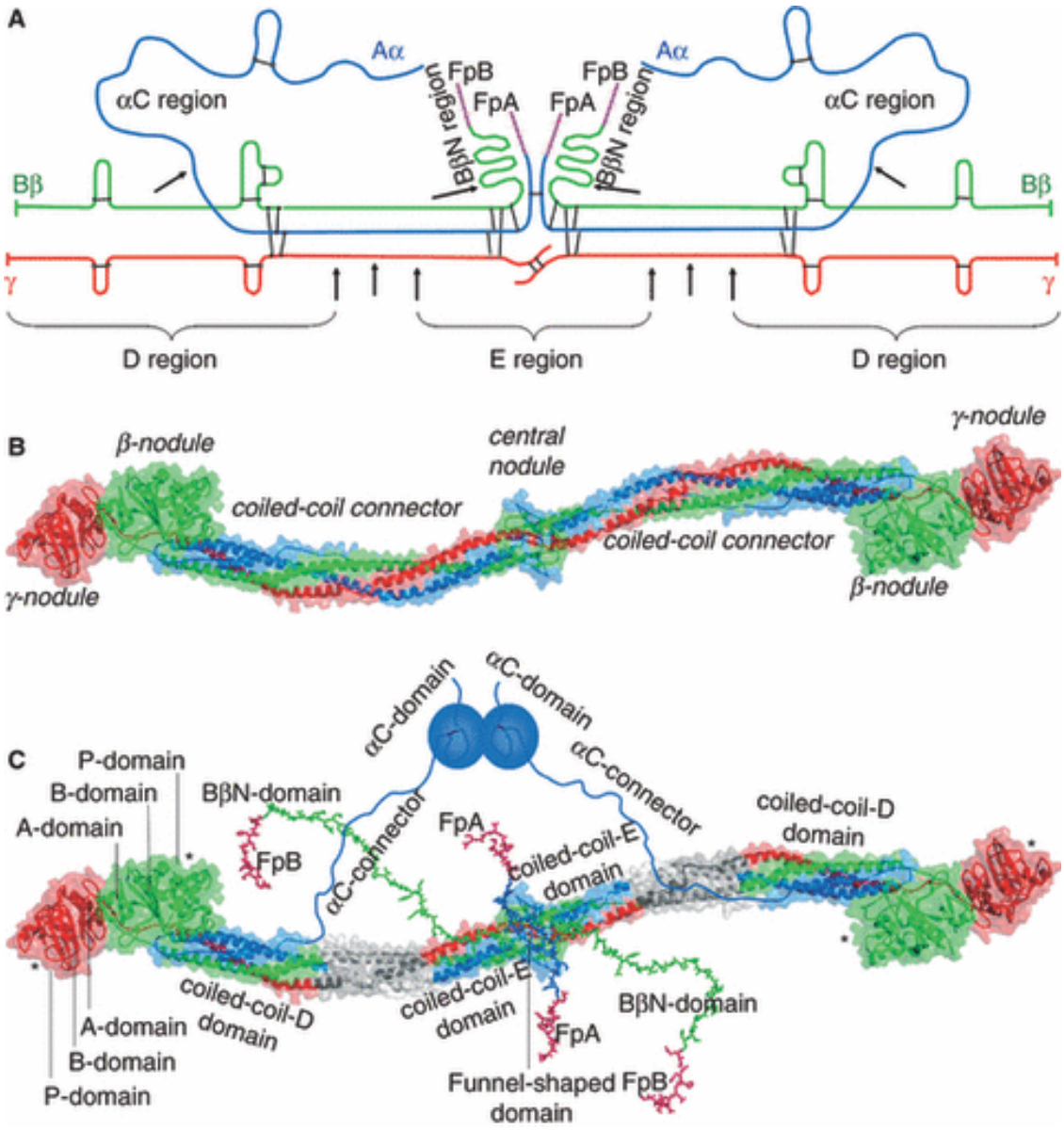

Figure 4. Fibrinogen structure by Medved [101]. ***(A) Polypeptide chain composition of fibrinogen. The individual chains, Aa, Bb and c, are blue, green and red. (B) Crystal structure of fibrinogen. (C) Same molecule as in (B) plus those regions that were not identified in the crystal structure***

In vitro, plasmin cleaves fibrinogen into different main fragments and many peptides. α and β chains are cleaved giving the first major product, also referred to as fragment X. Next, the coiled coils are cut leading to the apparition of the two terminal fragments (D fragments) and the central core domain (E fragment). For the case of cross-linked fibrin, the obtained fragments are quite the same, with the exception of the terminal fragments D of two joined molecules, which remain together leading to the D-dimers.

Since 1972, when Tooney and Cohen [20] reported crystals from proteolyzed fibrinogen molecules equivalent to fragment X, many studies have advanced on the crystal structure of the fibrin molecule. Between 1995 and 2000 crystal studies from fibrinogen fragments were made revealing information about the fragments D and D-dimers [21]. This led to the question of the role of A- and B-knobs in the formation of fibrinogen aggregates. A-knobs (and a-holes) seem to be oriented in order to favour the joint of D-fragments. The position and role of B-knobs remains an unanswered question.

6 Fibrin structure

We now review the ultrastructure of fibrin, which requires a multi-scale approach. We present the current knowledge on the longitudinal aggregation of fibrin monomers to produce protofibrils, which then aggregate laterally to form fibres and also cross-link. We also describe the state of the art concerning to the formation of branched fibrin networks. Next, we take as well account of the main environmental factors that influence polymerization. Finally, we review the existing knowledge on the mechanical properties of fibrin clots.

6.1 Protofibrils formation and structure

The nanoscale of fibrin structure is related to the early stages of polymerization, where longitudinal assembly of fibrin monomers occurs to form protofibrils. It also involves the lateral aggregation of the protofibrils to form a fibre (*cf*. Figure 2). The events corresponding to the nanometric scale of the ultrastucture of fibrin is mainly studied with scattering measurements as well as with electron-microscopy imaging.

In 1939, the resolving power of electron microscopy allowed Wolpers and Ruska [22] to obtain the first electron images of a fibrin network from human plasma. They observed for the first time the ~25nm axial periodicity in the fibres. Hawn and Porter [23], in 1947, reached the same conclusion from purified bovine fibrinogen. Hall [24] studied as well human fibrin fibres obtaining a 24nm periodicity. In 1959, Hall [25] proposed, using TEM positive staining, a geometry of fibrinogen. At the same time, it was proposed a polymerization model where fibrin monomers associate through end-to-end aggregation and then side-to-side aggregation to form fibres. The geometry of the molecule and the polymerization model proposed are illustrated on Figure 5.

Karges, in 1970 [26], observed that positive staining TEM patterns represent the accumulation of polar groups along the fibre but not necessarily zones of great density. On the other hand, negative staining gives more information about mass distribution within the fibrin fibrils. At this point, Hall's polymerization model was questioned.

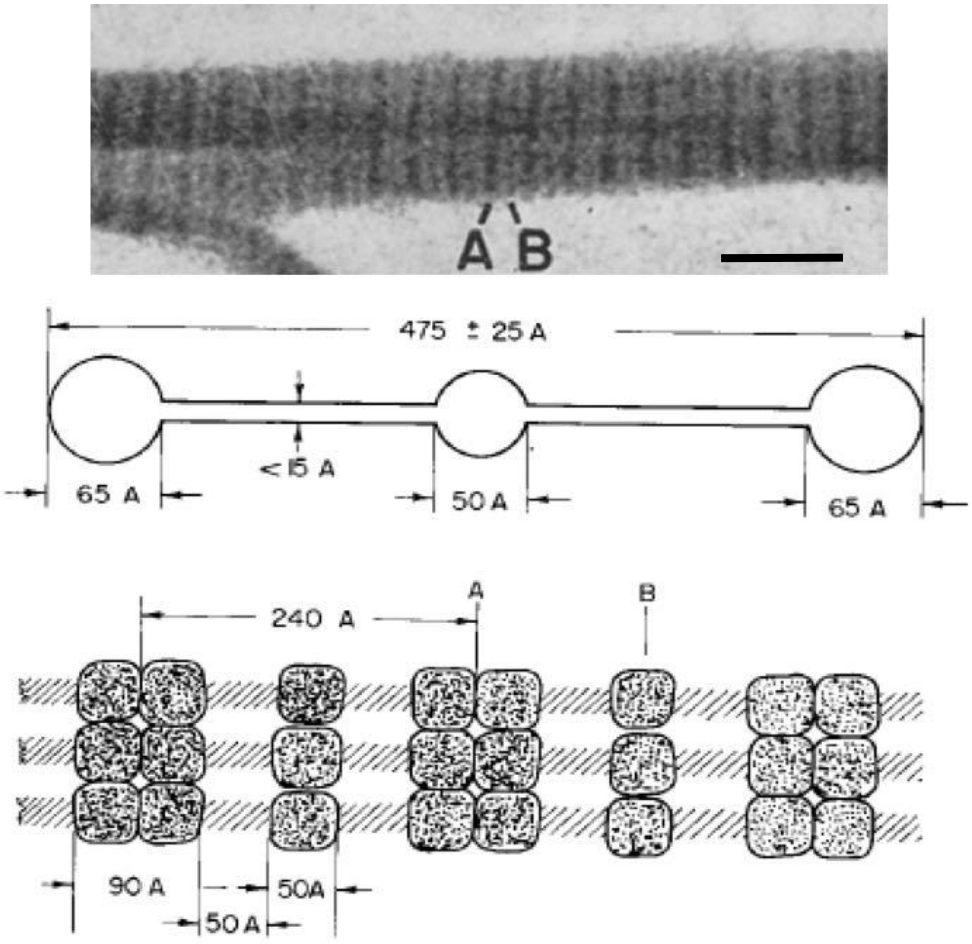

Figure 5. (Up) Fibre imaged by electron microscopy, scale bar: 100 nm. (Down) Geometry of fibrinogen molecule and polymerization model proposed by Hall [24].

In 1952, Ferry studied the polymerization of fibrin with light scattering [5,27]. Fibrinogen conversion into fibrin by mediation of thrombin was inhibited with hexamethylene glycol, which arrests the clotting and facilitates light scattering measurements. The intermediate polymer formed just before the gel point (*the stage at which the liquid becomes a gel*) was then studied. Ferry concluded that rod-like polymers are constituted by 15 monomers in average. It was then proposed a polymerization model where monomers first associate end-to-end in a half staggered way, as it is illustrated in Figure 6.

Figure 6. Two stranded protofibril made up of half-staggered monomers [43]

The linear aggregation of fibrin monomers is currently well established by the knob-hole model. Indeed, polymerization starts with the cleavage of fibrinogen's fibrinopeptide A pairs (also noted FpA). FpAs mask knobs "A" that are complementary to the holes "a", which are always exposed, although the Fps and knobs are not visible in X-ray crystallographic structures of fragment E [28]. Two fibrin monomers interact with each other in a half-staggered manner, so that knob "A" fits into hole "a" [29,30]. Because of the dimeric nature of the molecule, there are two "A"-"a" knob-hole interactions holding the two monomers together. This explains the linear aggregation of fibrin monomers.

Cohen and Weisel [31,32] studied fibrin polymerization performing negative staining electron microscopy. They confirmed Ferry's previous polymerisation model from light scattering experiments. The schematized model, which is illustrated on the inset of Figure 7, also proposes that the arrangement of fibrin monomers consists on two half-staggered filaments of molecules bonded end-to-end.

Hantgan and Fowler [29] performed as well negative staining measurements using electron microscopy. They duplicated their previous results obtained from light scattering experiments [4] The trinodular fibrinogen molecules are cross-linked through their outer nodules in an end-to-end, non-overlapping fashion. The defined D-D(-regions) contacts show clearly longitudinal aggregation and D-E(-regions) contacts are responsible of the staggered aggregation. The nature of the D-D contacts remains here speculative because of the little structural evidence for the arrangement of protofibrils within the fibrin fibres or for the position of the contacts between them.

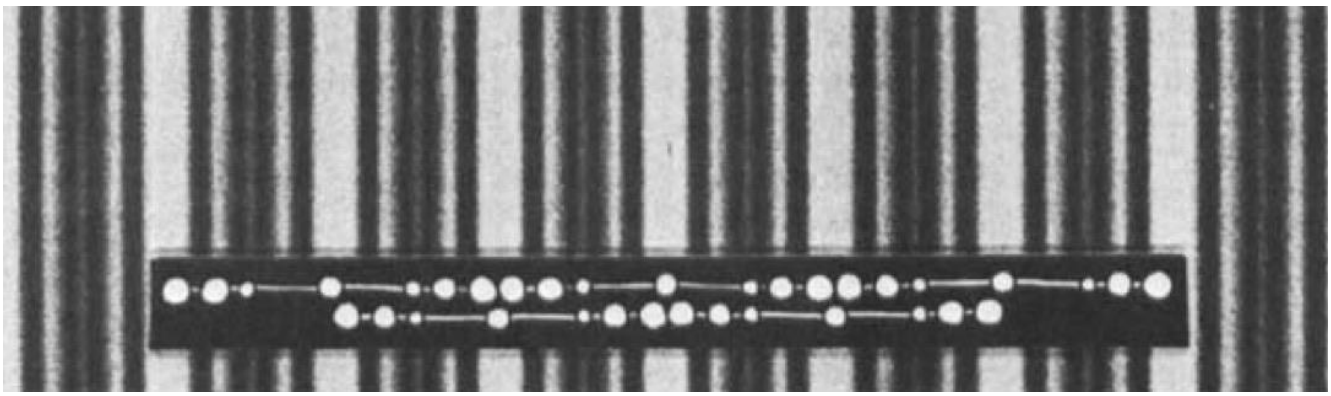

Figure 7. Main: TEM negative stain shows monomer assemblage with a periodicity of 22.5nm. Inset: Polymerization model proposed in agreement with Ferry's model. [32]

Several years later, in the 2000's, the appearance of *Stop Flow Multi Angle Light Scattering* systems allowed the study of the polymerization of fibrinogen in physiological conditions with a temporal resolution of 0.25 s. Bernocco and Ferri [33–35] performed experiments with this light scattering system. Results were compared with numerical simulations of the distribution of rod-like polymers, formed by random association of mono and bi-functional molecules. This led to a distribution previously proposed by Janmey [36] (later exposed on section 7). Four polymerization models were here considered by Bernocco and Ferri:

- End-to-end association forming a rigid single strand.
- End-to-end association forming a flexible single strand.
- Half-staggered association of two rigid strands.
- Half-staggered association of two flexible strands.

Comparison of numerical and experimental light scattering results concluded that the first polymers formed during polymerization are composed by two half-staggered flexible strands. This main composition of fibres may be however compatible with small quantities of single strands. This results is however dubious because of the not obtained linearity which is requited to apply Casassa's and Zimm's plots [37] to analyse experimental results.

6.2 Protofibrils association

Several hypotheses exist to explain lateral aggregation. In the 1980s electronic microscopy experiments from Weisel [32] suggested that the lateral aggregation of protofibrils is caused by molecular interactions on the D-domain.

One popular hypothesis is to devote the control of lateral aggregation to the cleavage of the second pair of fibrinopeptides (FpB) which exposes the knobs “B” at a considerably slower rate than FpA. Indeed, with FpA cleavage alone, clots are made up of thinner fibres than those initiated by the cleavage of both Fps. It has been hypothesized that knob “A”-hole “a” interactions are responsible for the interactions within a protofibril, while the knob “B”-hole “b” are responsible for lateral aggregation [38]. However, lateral aggregation can occur without FpB cleavage which is not consistent with this hypothesis [39,40].

Another hypothesis is that the oligomers must reach a certain length before they can aggregate laterally, so protofibrils are basically longer oligomers [29]. Longitudinal organisation of monomers has been well established but the lateral organisation of protofibrils remains still unclear. The model proposed by Fowler [29] for linear and lateral aggregation is illustrated in Figure 8:

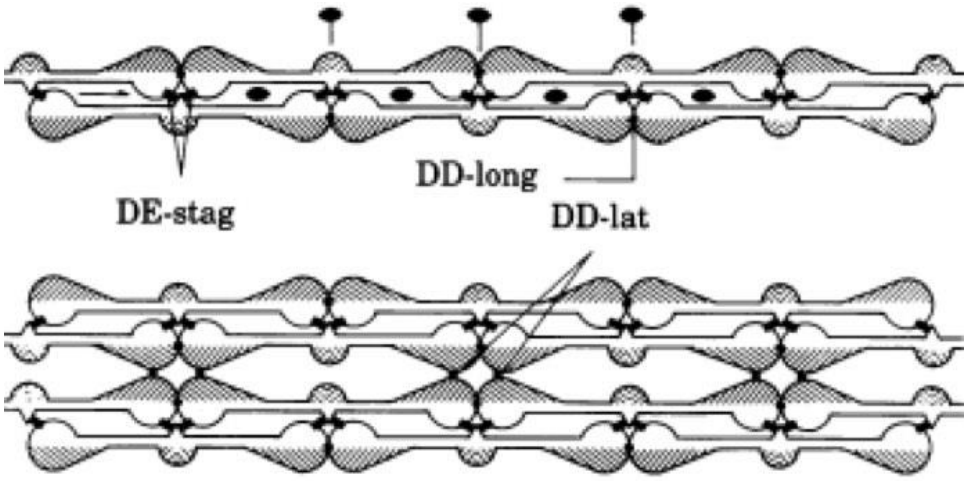

Figure 8. . Linear and lateral aggregation model proposed by Fowler et al. [29]

In 2000, Yang [38] introduced a model of fibrin formation, including longitudinal and lateral aggregation, which led to a proposal of the resulting fibrin network (*cf.* section 6.4). This model is based on packing interactions observed in crystal structures of the fragments D and D-dimers complexed, crystallized in presence or absence of two synthetic peptides that correspond to natural A and B knobs. This was studied before by Doolitle *et al.* [21,41]. This model, is in agreement with Ferry's previous work based on light scattering experiments [5] and it can be resumed in three steps:

- FpA cleavage exposes the A-knobs in the central domain of the fibrinogen molecule which form a liaison with the a-holes on the D-domain. The repetitive interaction of pairs of A-knobs with the associated ends of companion fibrinogen molecules leads to a two-molecule thick oligomer with a half-molecule stagger. These oligomers, previously defined as protofibrils, tend to average 15 units. [42] .
- γ-γ dimers are formed between D domains when reinforced by the factor XIIIa cross-linking (*cf.* section 6.3 of this Chapter).
- Lateral assembly of protofibrils, which remains unclear. γC-γC interactions allow fibre development while FpB cleavage may strongly encourage this lateral aggregation.

Yang's study also hypothesized about the systematic addition of protofibrils that polymerize into a fibrin network. Figure 9 illustrates, from different angles, the aggregation structure of a single protofibril (knob-hole interactions) and the lateral association of two protofibrils (denoted as PF1 and PF2).

Because of the periodicity of 22.5nm is maintained as new protofibrils are added to the fibres [43], they must be stretched as their path length increases as fibres grow thicker. It has been hypothesized that the cessation of lateral aggregation may occur when the energy necessary to stretch new protofibrils is larger than the bonding energy.

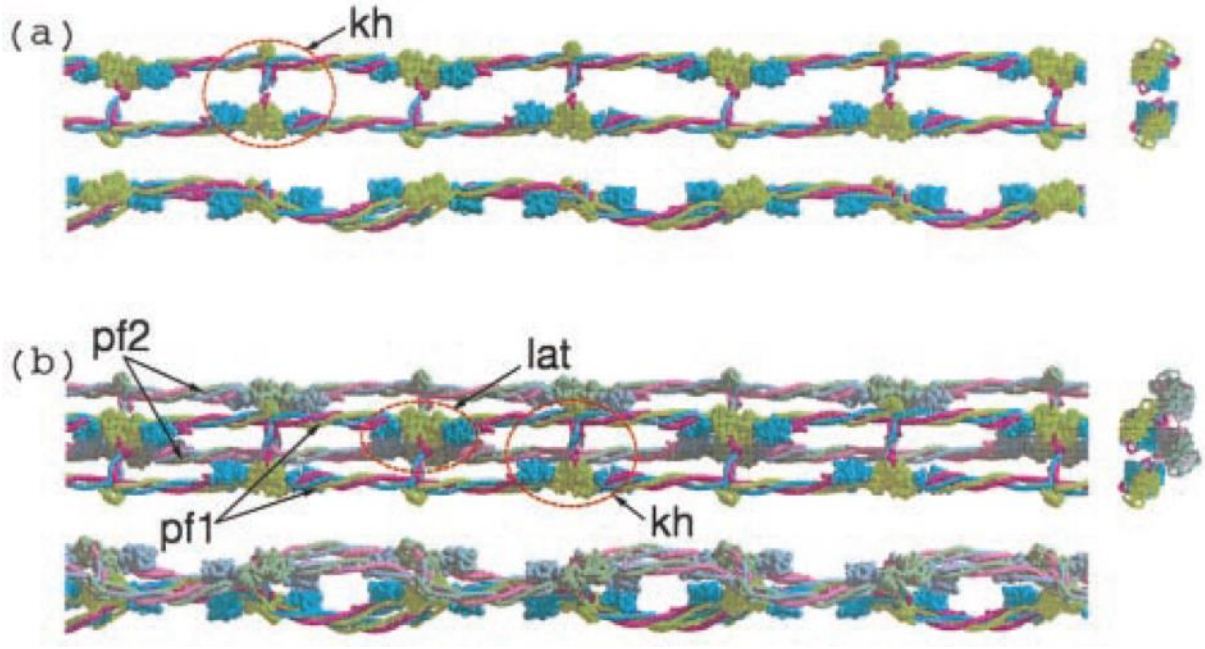

Figure 9. (A)Three views (top, side, and end-on) of a single protofibril formed by knob-hole (kh) interactions. Light green, α--chains; blue, β -chains, red, γ -chains.End-on view is shown at the right side. (B) Lateral association (lat) of two protofibrils (PF1 and PF2, top and side views; end-on view is shown at right).[38]

In 1986 and 1987, Weisel *et al.* [44,45] studied negatively contrasted fibrin samples in electron microscopy for different polymerization conditions, specially NaCl concentration, pH and temperature. For a physiologic range of fibrinogen concentrations, polymerization was triggered either with thrombin (in order to cleave both FpA and FpB from fibrinogen), baxothrombin (to cleave only the FpA) or venzyme (to cleave only the FpB).

All imaged samples present a 22.5nm periodicity. As well, low pH and low ionic strength seem to stimulate lateral aggregation when both fibrinopeptides are cleaved. The diameter of the fibres remained nearly constant under most of the experimental conditions tested, with the exception of very high ionic strengths where the diameter measured was considerably smaller. Weisel [45] suggested that fibres are constituted by twisted protofibrils, which may control the final diameter of the fibres.

Confocal microscopy was first used by Blombäck *et al.* in 1989 [46]. This study presented the feasibility of obtaining information of fibrin gels with this type of

microscopy while taking into account its limitations. Measurements were performed for a varied range of fibrinogen concentrations (from 0.5 to 4 mg/ml), salt concentrations and ionic strengths. Straight rod-like structures which come together at dense nodes were observed in confocal microscopy.

In contradiction with previous electron microscopy in dried-freeze samples results [47], the expected highly ordered structures were not visualized here. High ionic strength (0.24M NaCl) images showed fine structures contoured by blurred zones. Increasing ionic strength (0.33M NaCl) images presented almost only blurred zones. For lower ionic strengths, increasing thrombin concentration led, as expected, to shortening of node to node distances, smaller liquid spaces and decrease in turbidity, indicating probably thinner fibres. Confocal microscopy was again used by Blombäck *et al.* in 1994 [48] to make further experiments with recalcified plasma.

6.3 Cross-linking

The coagulation Factor XIII (FXIII) is the responsible of the covalent cross-linking of fibrin. FXIII is a heterodimeric structure, consisting in two A-and two B-subunits, that circulates on plasma bounded to fibrinogen by its B-subunit. FXIII becomes activated (noted as FXIIIa) by thrombin at the same time as the fibrinopeptides are cleaved from fibrinogen [49].

The remaining A-subunit of FXIIIa cross-links the α- and γ- chains, but not the β-chain. Fibrin formation accelerates the thrombin cleavage of FXIII activation peptides helping to achieve great coordination of events during the polymerization process. The cross-linking process is schematized in Figure 10.

Cross-linking is not only important in fibrin polymerization, but also plays a very important role in the regulation of fibrinolysis, a process interfered with by the presence of α-chain cross-links. The presence of Factor XIIIa can also influence slightly the viscoelastic properties of the clot fibrin clot [50–52].

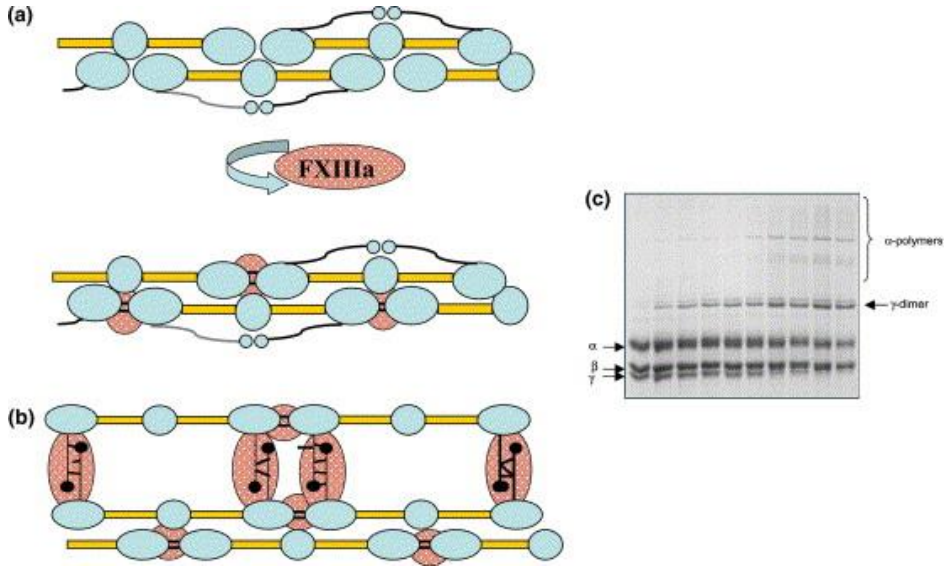

Figure 10: Fibrin crosslinking: activated FXIIII introduces ε-(glutamyl) lysine isopeptide bonds between the C-terminal γ-chain crosslinking sites in the protofibrils to rapidly form γ-dimers (a). Crosslinking of the α-chain to other α– chains occurs more slowly. Image from Standeven et al.[49]

6.4 Fibrin fibres structure

During 1980's Ferry *et al.* performed several studies with Small Angle X-ray Scattering (SAXS) in order to characterize the structure of fibrin fibres. In 1982, [53] they realized SAXS measurements of non-deformed fibrin clots founding a slight disagreement in the periodicity of the fibres from their birefringence experiments [54]. They measured 29nm and not the usual 25nm. It was in 1989 when Muller and Ferry [55] found repeating spaces at 24.5nm, 12nm and 8nm. These measurements correspond to the fundamental, first and second harmonics of fibrin longitudinal periodicity.

Also in the 1980's Torbet *et al*. [14] studied the oriented formation of fibrin gels by polymerization in strong magnetic fields, because of the diamagnetic anisotropy of the particles, when many monomers come together in an ordered way.

Near the beginning, there is little induced birefringence because the present fibrinogen molecules and fibrin monomers have only a small diamagnetic anisotropy (magnetic orienting energy is much less than thermal energy, or Brownian movement, and consequently they orient poorly). Birefringence increases then with polymerization. Many monomers come together in an ordered way and the diamagnetic anisotropy of

the aggregates is found to be many times that of a monomer, so the magnetic orienting energy is large enough to allow a high degree of orientation. Torbet established that when the polymerization proceeds too rapidly, the interlinked network develops before the nascent fibres have had time to fully orient themselves.

Low angle neutron diffraction pattern from magnetically oriented fibrin gels (at high fibrinogen concentration and heavy water buffer) and birefringence measurements were performed. In addition to the previously known 22.5nm repeatability, they concluded that the fibrin monomers are arranged in a regular three-dimension lattice with a high degree of crystallinity along the fibre axis. Results also suggest a tetragonal crystalline lattice where the unit cell has the dimensions: 18.4 x 18.4 x 44.6 nm. This consist on a square base of 18.4 nm and 44.6nm height, which corresponds to the length of fibres which associate themselves in a half-staggered manner thought the axis of the fibre (corresponding peak at 22.3 nm).

Posterior studies in 1983 and 1987 demonstrated that the scattering patterns of magnetically oriented fibres remain constant within the role of many factors. The dependence of calcium, factor XIII [15] was studied as well at high fibrinogen concentration (10 mg/ml) and for a range of thrombin concentrations (0.018 to 0.05 IU/ml). The polymerization activated either by thrombin or reptilase [56] was also investigated showing that the packing of molecules within the fibres is very similar independently on if FpAs and FpBs are both cleaved or if only the FpAs are cleaved.

The polymerization model introduced by Yang [38], and previously described on section 6.2 of this chapter is shown in Figure 11. This model led to the proposal of a unit cell configuration that has as dimensions 19 x 19x 45 nm. Here, two strands of any protofibril are 8nm apart. Because of the fibre vacancies in the fibre, there are only eight molecules by unit cell. The calculated solvent is 80% (the remaining 20% are proteins). Yang's work is in agreement with Hermans model [57] based on experimental (turbidity and light scattering) observations.

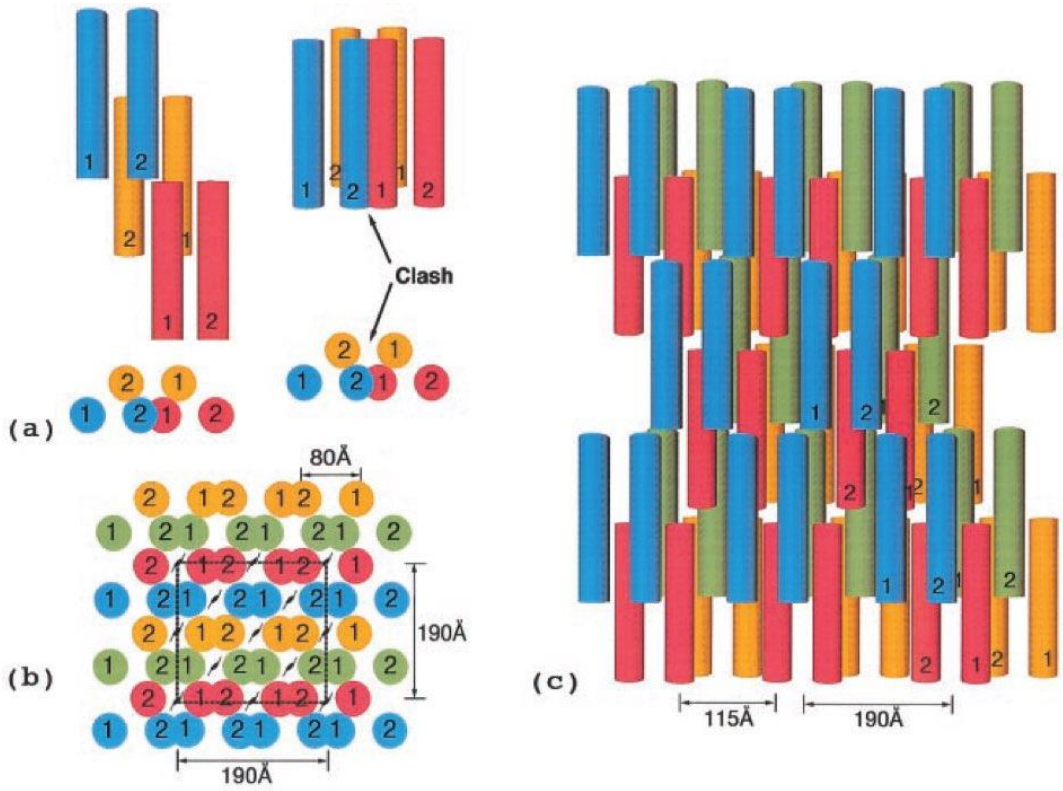

Figure 11. Yang's crystalline model of a fibre. (a) Three protofibrils aggregation in two strands (represented by 1 and 2). (b) and (c)are the top and side views of a fibre. Blue colour represents the first plane, red the second plane, green the third one and orange the fourth.

Atomic force microscopy (AFM) was used by Guthold in 2004 [58] to study the mechanical properties of fibrin fibres in quasi-physiological conditions. It was observed that the rupture force of fibrin fibres and their fluorescence light intensity increases as the diameter as a power law $d^{1.3}$. This led to the assumption that the number of molecules per fibre cross-section increases with diameter following the same power law and the inside of a fibrin fibre is a fractal with fractal dimension 1.3. This implies that the protein density of fibres decreases with increasing diameter, *i.e*. thicker fibres are, on average, less dense. A fractal dimension of 1,3 for a porous structure like fibrin is compatible with a small protein density and would explain the absence of lateral order of the fibres.

In 2009, Weigandt *et al*. [59] performed SANS and USANS experiments in D_2O solution for a wide range of fibrin concentration and constant low thrombin concentration. They used the scattering invariant as a method to determine, through a Guinier analysis, the average internal volume fraction of protein in the fibres, which

increased with initial monomer concentration (C), following a power law $C^{0.1}$. The determination of the average radius of the fibres showed a slight decrease with increasing concentration. In 2011, Weigandt [60] applied SANS and USANS measurements to study the origin of strain hardening in fibrin networks. This combining study of neutron scattering and rheology to test the structural properties of a fibrin clot over a wide range of deformation will be further discussed on section 9.

In 2010 Missori *et al.* [61] realized SAXS experiments in order to investigate the influence of specific anions on the architecture of protofibrils within fibrin fibres. They found significant differences in the longitudinal and lateral repeatability of fibrin fibres between the presence of Cl^- and F^- anions in solution.

Also in 2010, Yeromonahos *et al.* [7] determined the longitudinal and lateral structure of fibrin fibres in quasi-physiological conditions using spectrophotometry and X-ray scattering measurements. First, they obtained information about the radius and density of fibrin fibres, determining for instance the influence of ionic strength on fibrin structure.

X-ray scattering was used to validate the spectrophotometry method. The obtained scattering curve of a fibrin clot, is shown on Figure 12-up. The interpretation of SAXS spectra shows that the half staggered periodicity of 22.25nm and the broad peak observed for sizes between 6 and 19nm appear to be related to the lateral nanostructure of fibres. Complementary, this study proposes that the lateral structure would be a fractal with a dimension 5/3 (interpretation illustrated on Figure 12-down) which agrees with the previous work of Guthold *et al* [58]. The lateral protofibril arrangement is interpreted here as a crystal with many holes or as a fractal structure.

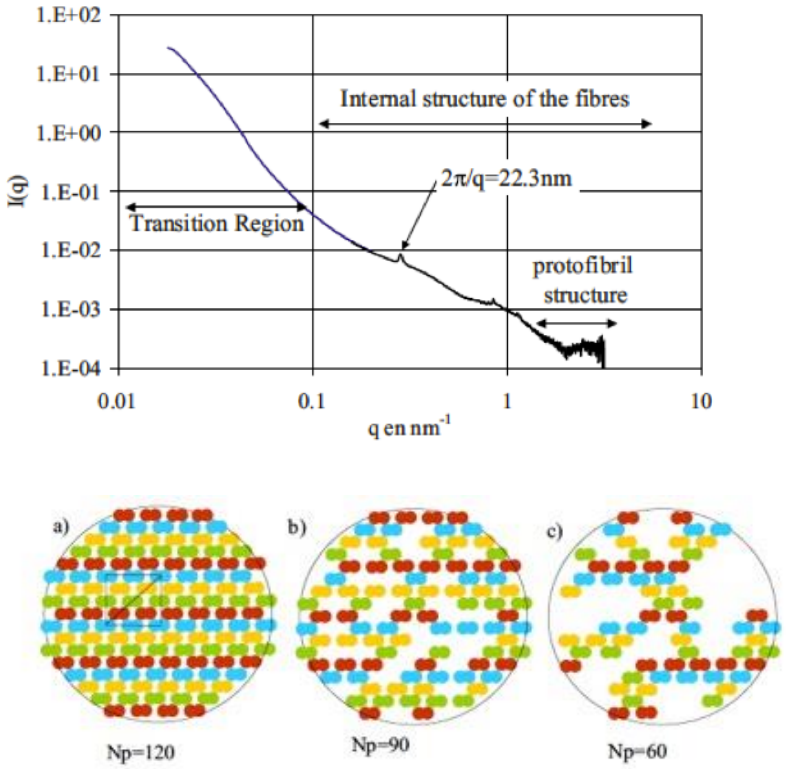

Figure 12. (Up) SAXS spectrum of a fibrin clot at [Fg]=1mg/mL; IIa=1UI/ml; 300mOsm. The arrows describe in detail the main features of the internal structure of the fibre.

(Down): Schematic of the internal structure of a fibre of radius 75nm. a) Crystalline structure with a number of protofibrils of 60 (maximum possible density). b) Structure with 25 % of protofibrils removed with respect to a). c) Structure with 50 % of protofibrils removed with respect to a)

Images from Yeromonahos et al. [100]

Whittaker [62], in 2009, applied polarized light microscopy methods using the anisotropic molecular structure of fibrin. The role of fibrin structures in thrombus integrity was then determined by quantifying the orientation of fibrin fibres and their anisotropy reproducing, *in vitro*, aneurysm-like and coronary arteries-like clots. The degree of fibrin organization differed significantly according to the location of clot formation; fibrin was most aligned in the aneurysms and least aligned in vitro whereas fibrin in the coronary clots had an intermediate organization.

In 2011, Yermolenko [63] visualized hydrated fibres with AFM microscopy. Images showed a periodicity of 24nm, in agreement with previous electron microscopy and X-ray diffraction results. This periodicity appears much more clearly on the case of

thin fibres and it becomes less clear with fibre's growth. It was proposed that thinner fibres are denser than thicker ones. The molecule packing decreases then with the increase of the fibres diameter.

In 2013, Lang *et al.* [64] developed a method to estimate the pore size of imaged biopolymer networks by determining the distribution of distances from random points in the fluid phase to the nearest fibre. The pore size distribution was found to follow a power law of $c^{-0.5}$, where c is the initial concentration of fibrinogen that will constitute the fibrin network. Similar results of the exponent law of $c^{-0.5}$ for the pore sizes were also obtained for instance by Piechocka *et al* [65].

6.5 Conclusions

Fibrin is formed from fibrinogen after activation by thrombin, which cleaves fibrinopeptides A and B yielding fibrin monomers. Monomers aggregate first linearly and then laterally to form fibres. It is commonly accepted that monomers aggregate first in half-staggered linear protofibrils with a periodicity of 22.5nm, which corresponds to the half length of a fibrin monomer. On the other hand, the lateral organization of fibrins is more controversial and it is still under debate.

The oriented formation of fibrin clots under strong magnetic fields has concluded, that, in addition to the 22.5nm repeatability, fibrin monomers arrange in a regular three dimensional lattice with a high degree of crystallinity along the fibre axis. Complementary, it has been proposed that the lateral structure of fibres can be a fractal with dimension 5/3.

7 Fibres growth and structure.

7.1 State of the art

We have reviewed the main aspects of fibrin fibres early formation that involve longitudinal and lateral aggregation. Next, we review the main work performed in order to investigate the kinetics and growth of fibrin fibres.

First studies on blood clot turbidity, which allowed to track the formation of a clot were made by Kinkle during the 1930's. In 1955, Casassa [37] published a method to study the light scattering of long rod-like particles, which was applied to the polymerization of fibrinogen. This model provides a quantitative link between the opacity of fibrin clots and the structural properties of fibrin through the calculation of the mass-to-length ratio of the fibres.

Ferry studied in detail [12,27] blood coagulation using turbidimetry techniques, aiming to observe the evolution of opacity during polymerization. Ferry also analysed the influence of several factors on coagulation (pH, ionic strength or reagent concentrations among others) defining which was defined as *coarse* (more opaque) and *fine* (more transparent) gels. With increase of pH and ionic strength the opacity goes through a minimum and the fibrin clots are considered as *fine gels*. Also with increasing pH, the gel time (which represents the time needed to visually observe the sample's change of opacity during the polymerization) goes through a minimum. Below pH 5.3 and above 10 the gel formation is inhibited. The measured clotting time at high pH is ascribed to the effect of electrostatic repulsion, probably between two fibrinogen molecules in end-to-end unions.

In 1952, Greene [6], followed Ferry's results [5] and performed light scattering experiments. He determined the influence of several environmental factors, as pH or temperature, on the radii of polymerized fibres as function of time. The ionic strength was kept constant at 0.15M. Experiments were performed at pH 7.15 and 5.85 finding significant variations on the final radii of the fibres after 30 minutes and 4 hours. Radii evolved in time from 65 to 70nm and from 87 to 120nm for both studied pH respectively. However, the range of fibrinogen concentrations tested did not show any major influence on the radii of the fibres.

In 1978, Carr [57] applied Casassa's work [37] to model the calculation of the mass-to-length ratio of fibrin fibres. At high pH and high ionic strength (corresponding to not gelled and just gelled fibrin clots), it was found that the mass-to-length ratio is the same as the one calculated by Ferry for one protofibril [5], *i.e.* 15 monomers associated end-to-end and half staggered.

Also, at pH 7.4, Carr compared the effect of ionic strength on the mass-to-length ratio. For an ionic strength of 0.35M, fibres are found to have a higher mass-to-length ratio, averaging three protofibrils associated laterally. However, at pH 7.4 and ionic strength of 0.1M, the fibres have a hundred times more protofibrils.

Hangtan and Hermans used stop-flow light scattering measurements in 1979 [4] to study fibrin polymerization kinetics and its structure. They postulated, also in agreement with Ferry [5], that assembly of fibrin occurs in two steps. The first step is end-to-end aggregation of fibrin monomers and the second is lateral association of protofibrils into fibres. The rate of linear aggregation of monomers is three times larger for low salt concentrations (0.1M) than for higher concentrations (0.5M). As well, lateral aggregation takes twelve times longer at 0.5M than at 0.1M. *Coarse gels* formed at low salt concentrations are shorter and thicker while *fine gels* formed at higher salt concentrations are longer and thinner.

The role of fibrinopeptides A and B was studied by initiating polymerization either with large concentrations of thrombin or baxothrombin (which only cleaves the fibrinopeptides A of fibrinogen). Hantgan and Hermans concluded that the FpB is not crucial for fibrin polymerization and does not affect linear aggregation of monomers. However, the fibrinopeptide B can accelerate lateral aggregation of fibres.

Based among others on Witlzius experimental data [66], Janmey *et al.* developed a theoretical model for the kinetics of the formation of fibrin oligomers which was supported with experimental light scattering data [36,42]. Janmey *et al.* calculated the size distribution of oligomers from the fraction of binding sites that have been uncovered by removal of A peptides, which was obtained from the concentrations of the reactants and the relevant kinetic constants. The model, and the experimental data, agree that the two fibrinopeptides A are removed at different rates, more concretely by

a factor of 16. This outcome was in disagreement with previous results from Landis and Waugh, who had proposed a factor of 40 [67].

In 1989, Blombäck [46] analysed the influence of fibrinogen and thrombin concentrations and of the ionic strength by using turbidity among other techniques. Blombäck found, accordingly with Carr's results, a decrease of the diameter of the fibres as the ionic strength increases (until 0,24M).

In 1991, Cristofaro [68] proposed a phenomenological model for the characterization of fibrin clotting. Cristofaro took account of three parameters in this model: the maximum increase in absorbance per unit time (ΔA_m) at the inflection point of the clotting curve, the time needed to reach the maximum increase (t_m) and the clotting time (t_c), which is the extrapolation of the slope at t_m. Cristofaro applied a large set of experimental conditions varying concentrations, pH or temperature among others. The t_m and the t_c are linked through a linear relationship independently of the experimental conditions. It exists a linear relation of the clotting time with the inverse of thrombin concentration, and with pH and temperature.

Weisel *et al.* [69] presented a kinetic model based on experimental observations. This model shows that when fibrinogen concentration increases, the coagulation time is shorter, and the maximum size of fibres increases. There are more and longer fibrin fibres. The dependence of the fibrin clot on fibrinogen concentration has a physiological importance because high fibrinogen levels are a risk factor for cardiovascular disease [70].

In the early 2000's, Ferri *et al.* [35,71] combined classic light scattering with Small Angle Light Scattering (SALS) to study the structure and also the kinetics of fibrin clot formation in physiological conditions. This work describes the kinetics of clot formation in three phases:

- After approximately the first minute of polymerization the phase of linear aggregation is concluded. The scaffold of the network is formed during this phase. An initial fibrinogen concentration of 0.24 mg/ml (respectively 0.8 mg/ml) and a thrombin/fibrinogen rate of 1/100 were tested. This led to 27μm length fibres (respectively 13μm) and a diameter of 5μm for both conditions.

- During the following ~40 minutes the length of the fibres remains invariable. However, the diameter of the fibres increases. For the initial fibrinogen concentration of 0.24 mg/ml a diameter of 130nm was measured, while for 0.8 mg/ml the diameter was found to be 190nm.
- After 40 minutes no changes were measured either in length or fibre diameter.

In 2004, Blombäck *et al.* [72] performed confocal microscopy imaging to determine the role of fibrinopeptides A and B on the architecture of the resulting networks. Images showed that the structure created, at the same *gel time*, for a "thrombin-activated clot" is more porous than the structure of a "reptilase-activated clot". Combined experiments in electrophorese also showed that for the same gel time, baxothrombin cleaves more fibrinopeptides A than thrombin (which also cleaves fibrinopeptides B during the process). Blombäck proposed then that the role of fibrinopeptides B is to promote branching between polymers.

The formation of thrombin-activated clots requires less fibrinopeptides A: less polymers need to be active for the interactions to occur, so the resulting network is more porous. Blombäck postulated that since this differences remain during the whole polymerization process; the structure of the network is governed by the events that occur before the gel time.

Chernysh and Weisel [73] used, in 2008, deconvolution microscopy in order to investigate fibrin networks in the hydrated state. The purpose was to visualize in real time the formation of the networks. Fluorescence results showed that 70% of the fibres reach their maximal length (10 to 20 μm) at the gel point. In contrast, at this point the diameter of the fibres was less than 25% of the maximal. These results were complemented with turbidity measurements to determine the different stages of polymerization.

They determined that when 15% of the maximal turbidity is reached, a first network is formed. At this point, fibres reach 25% of their final diameters, 80% of branching points are formed and 70% of the maximal length of fibres is attained. The maximal length of fibres is achieved at 60% of final turbidity. Lateral aggregation reaches a plateau coinciding with turbidity's plateau. The aggregation model proposed

by Chernish and Weisel supposes that the initial network is early formed and it evolves by addition of new fibres, and elongation and branching of existing fibres.

In 2011, Chernysh and Weisel [74] used confocal and electron microscopy to study the sequence of early events in clotting. At the beginning of the lag period most structures were found to be monomers. At the half time of this lag period they observed monomers, oligomers, protofibrils (structures composed by more than 8 monomers) and fibres, asserting that fibres are not the primary structures at this point. At the end of the lag period, there were primarily monomers and fibres, finally giving way to mainly fibres at the gel point.

In 2012, Domingues *et al.* [75] studied the influence of an alternative spliced form of γ-chains, noted as γ'. The role of γ'-chain was imaged during protofibril formation with AFM microscopy while final structures were studied with confocal and electron microscopy. Fibres produced with fibrinogen γ' show reduced protofibril packaging over a range of thrombin concentration leading to dramatic effects on protobrils content and protein density within the fibres. The inhibition of protofibril growth is visualized during early stages of polymerization. Due to fibirinogen γ', when two chains γ' come together, they disrupt the growth of the protofibril and modulate fibrin structure and strength.

In 2013 and 2014, Huang *et al.* [76,77] determined that the nature of fibrinogen plays a critical role on fibrin kinetics and polymerization. This work shows that the isolation of monomers by gel filtration chromatography of plasma and recombinant fibrinogens has a dramatic effect on the polydispersity profile of the preparations. Figure 13 illustrates the effect of gel filtration chromatography on the average radius of fibrinogen molecules.

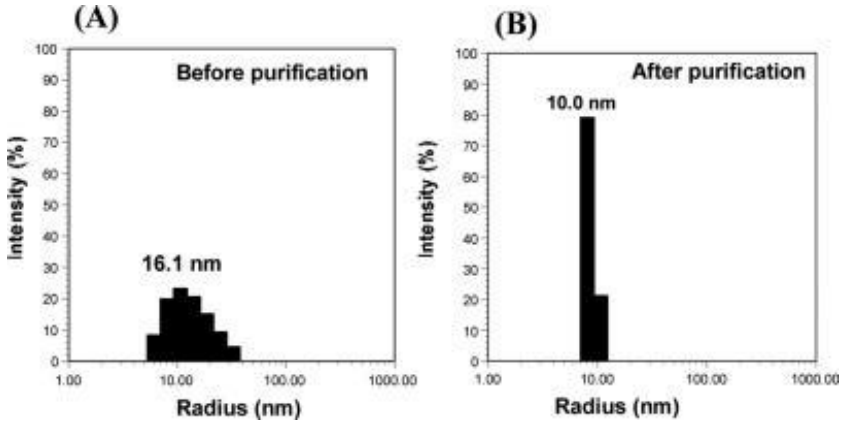

Figure 13. Hydrodynamic radius of a fibrinogen preparation before (A) and after (B) of gel filtration chromatography

The polymerization of fibrin from mono- and polydisperse fibrinogens was monitored by turbidity [76] and dynamic light scattering methods[77], as well as imaged by scanning electron microscopy. Surprisingly, turbidity measurements showed that monodisperse samples (at low concentrations of ~0.4 mg/ml) result on an increase of turbidity of a factor two compared to the initial polydispersity preparations and the polymerization curves were found to be independent between the initial and their respective isolated preparations.

The same polymerization conditions were later tested by DLS measurements, which is illustrated on Figure 14. This confirmed that monodisperse fibrinogen preparations form protofibrils slower; however, the formation of fibres occurs much faster than for the initial polydisperse preparations.

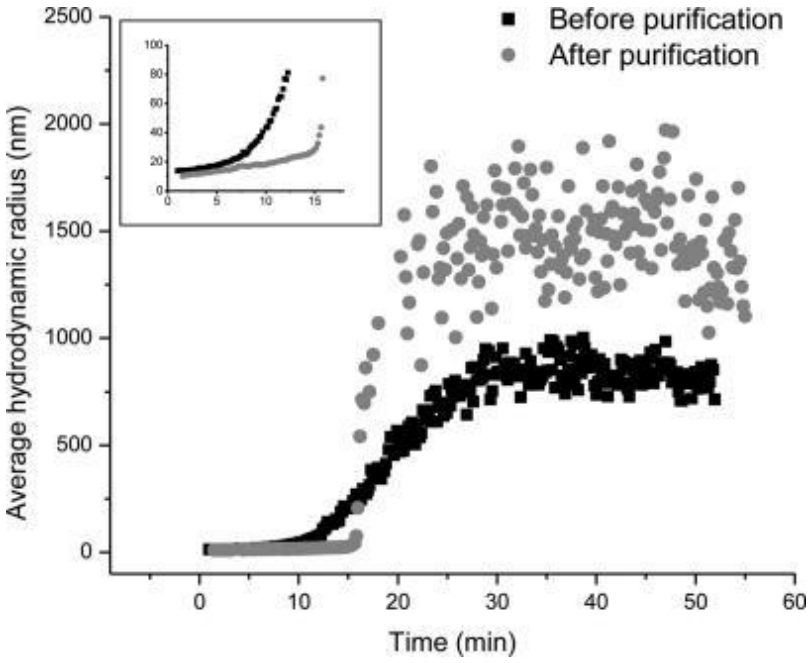

Figure 14. Polymerization of polydisperse and monodisperse fibrinogen preparations ([Fg] = 0.4 mg/ml; [IIa] = 0.1 IU/ml) monitored by DLS

7.2 Conclusions

The kinetics of fibres growth has been studied since 1930 by the use of turbidity methods. Moreover, the development of a model for rod-like particles to determine the mass-to-length ratio of the fibres has been a powerful tool for the study of the early stages of polymerization under a wide range of conditions. Since the beginning of the XXIth century, new small angle light scattering methods have allowed also to quantify the different phases of coagulation, since the early stages until the development of a fibres network.

Variations on pH and ionic strength have allowed to modify the kinetics and the structure of fibres and to understand the processes involved in coagulation. The formation of *coarse* (short and thick fibres) or *fine* (long and thing fibres) gels allowed to determine the first steps of polymerization: end-to-end aggregation on the first stage and lateral aggregation on the second.

The role of the fibrinopeptides A and B has been also largely studied during these years. Moreover, the determination of the cleavage rates and the role of the Fps, concluded that the FpB is not crucial for fibrin polymerization and does not affect linear aggregation of monomers but can accelerate lateral aggregation of fibres. Therefore, this has allowed to understand and control the architecture of fibrin fibres networks.

During last years, many groups have investigated the role of several parameters of fibres development. Here, we pay special attention to the work of Huang *et al.,* who determined, by isolating fibrinogen monomers, that the role of the nature of fibrinogen can be of great importance on the kinetics and final structure of fibrin clots.

8 Clot lysis

While being generated, fibrin activates the fibrinolytic system, playing an active role in the tissue plasminogen activator (tPA) mediated conversion of plasminogen to plasmin. Plasmin is going to bind to fibrin and degrade it into fragments that will be removed into the circulation.

Many physiological and pathological factors determine the structure of fibrin and, in consequence, they will have an influence on how these fibres are dissolved during lysis. Some examples that have been studied are, for instance, the influence on clot lysis of disfibrinogenemias, thrombin concentration [78], anticoagulants such as aspirin or heparin [79,80] or pathologies like, for example, myocardial infarction [79,81] .

We pay in this study special attention to the work of Gabriel *et al.* in 1992 [78], who applied Carr's turbidity method [57] to determine the rates of clot lysis. Gabriel determined the decrease in the fibre mass-to-length ratio during fibrinolysis showing that plasmin generation is proportional to fibre thickness. For a constant plasmin concentration, thin fibres are dissolved at a slower rate than thick fibres. Thin fibres composed by 5.25 monomers were found to be degraded at a rate of 0.09 monomers/minute while the degradation rate of thick fibres composed by 35 monomers was 1.3 monomers/minute.

Two effects of the thin fibres on fibrinolysis were observed by Gabriel *et al*. One is the slower rate of plasmin production and the other a slower rate of fibrin digestion by plasmin. The link between these two events could be explained by hypothesizing the decrease on the tPA binding sites in the fibres, the decrease or restricted access to plasmin binding sites or a combination of both.

The theory of a decrease of plasminogen binding to fibrin [78] has been strengthened from observations showing that clots with a fine fibrin (tight) conformation display a slower lysis rate than those with a coarse fibrin (loose) conformation. So far, neither a molecular nor a structural basis has been proposed to explain these differences.

Collet [82] performed confocal imaging to study the fibrinolysis. It was observed a progressive disaggregation of the fibrin fibres indicating that fibrinolysis proceeds by

transverse cutting rather than by progressive cleavage uniformly around the fibre. Plasma fibrin clots with a loose fibrin conformation made of thick fibres were found to lyse faster than those clots with tight fibrin conformation made of thin fibres. However, individual thick fibres were cleaved at slower rate than thin fibres.

Abnormal fibrin architecture is generally thought to be a determinant factor of hypofibrinolysis. However, because of the lack of structural knowledge of the process of fibrin digestion, the relations between fibrin architecture and hypofibrinolysis remain controversial [82].

9 Mechanical properties of fibrin

9.1 State of the art

The conversion of fibrinogen to fibrin has the physical consequence of an increase in rigidity. Finite stiffness appears when a continuous network is established at the gel point and it then increases over time as polymerization proceeds [19]. Fibrin must be rigid enough to stop bleeding but, at the same time, it has to be open for perfusion and penetration of cells. The mechanical properties of fibrin in a thrombus will determine how it responds to blood flow. (65,83,84).

A number of studies that examined the clinical consequences of altered clot structure have provided clear evidence that changes in clot structure are a risk factor for cardiovascular diseases [81]. In particular, the formation of tight networks of thin fibres and decreased porosity has been related with cardiovascular diseases.

The different responses of fibrin clots to a stress, such as reversible elastic deformation, irreversible plastic deformation or embolization can all have very important clinical outcomes. Clots of low stiffness could lead to bleeding while stiff clots may have a relation with coronary thrombosis [85].

The rigidity of fibrin structures was first quantified by Ferry *et al.* [51,86,87], who concluded that a finite elastic modulus (G') appears at the gel point when the network is first established. The network that is formed at the gel point is a skeleton that sets the plan for the clot structure by addition of further material [48]. Stiffness continues to increase at a similar rate as turbidity does. Figure 15 illustrates the evolution of rigidity as a function of time, which is represented by the elastic modulus, G' [dyne/cm^2].

Between 1973 and 1976, Ferry *et al.* [51,86,88] realized a series of studies on the rheology of fibrin clots. Rigidity of fibrin clots was found to depend on several environmental factors such as the pH, temperature or concentration. Moreover, the stiffness of the clot can take up to 24 hours to reach its maximum because of slow re-arrangements that take place, for instance, in the case of coarse unligated clots.

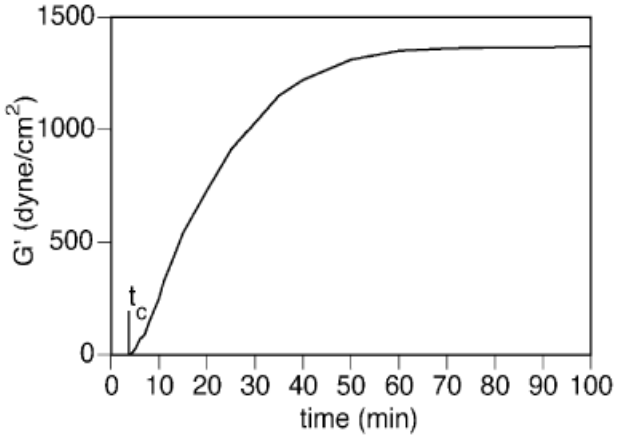

Figure 15: Elastic modulus as a function of time for fibrin clot formation with Factor XIIIa in quasi-physiological conditions. tc corresponds to the gelation time. Figure from Roberts et al [51] reploted by Weisel [84]

Roberts *et al.* [51,86] compared the mechanical properties of fine and coarse uncross-linked fibrin clots. They measured the *elastic* and *loss modulus* (*G'* and *G''* respectively) for small oscillation deformations and for a wide rage of frequencies (from 0.01 to 160Hz). The elastic modulus of fine, uncross-linked, clots is nearly constant as a function of frequency. On the other hand, coarse clots present a slight dependence on frequency. For low frequencies, the loss modulus (*G''*) is small and clots present mainly elastic deformation. At higher frequencies, *G''* increases and irreversible processes can become equal to reversible deformation, *i.e. G'=G''*. This is represented on Figure 16.

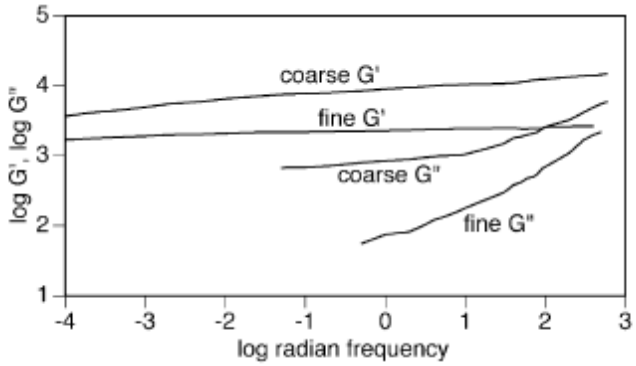

Figure 16. Elastic (G') and loss (G") moduli plotted against frequency for fine and coarse fibrin clots [84]

As Brown [89,90] observed, fibrinogen molecules can be stretched to an extension corresponding to a 100% strain. Fibrin clots are also highly extensible and can be greatly stretched before breaking. From Liu's work [91,92] combining AFM and fluorescence, we know that the role of individual fibres of the clot is crucial, but so are the structural rearrangements of the network when the stretching takes place.

In 1999, Ryan *et al*. [52] also studied the stiffness on fibrin clots from ligated and unligated clots. It was hypothesized that the main actor of the increase of stiffness on ligated clots is the α-chain crosslinking.

Bale and Ferry [93] studied the dependence of A and B binding sites on the mechanical properties of fibrin. Polymerization was initiated either by thrombin or ancrod (which only cleaves the FpB). The elastic moduli were found to be between 2 and 4 times larger on thrombin-activated clots than those clots formed by only FpA cleavage by ancrod.

In 1983, Janmey *et al.* [94] performed rheological measurements on purified *fine* fibrin clots, formed at high pH and high ionic strength. For low strains, stress is directly proportional to strain. The slope of the curve, corresponding to the elastic modulus, is constant. At large strains the slope increases dramatically, so the stiffness increases up to a factor of 20. This phenomenon is called *strain hardening* or *strain stiffening.*

In 2007, Janmey [95] performed shear deformation measurements for both fine and coarse fibrin clots and a negative normal stress was observed. This means that networks of semiflexible biopolymers, when sheared between two plates tend to pull the plates together. The negative normal stress can be as large as the shear stress. This property was supposed to be directly related to the nonlinear strain stiffening.

As explained on section 6.4 of this chapter, Weigandt *et al.* [59,60] performed Small Angle Neutron Scattering (SANS) and rheology measurements to investigate the structure and mechanical properties of high density fibrin clots. Fibrin clots were polymerized for a wide range of fibrinogen concentrations (diluted on *heavy water,* or D_2O, solvents). The nonlinear behaviour, obtained from the representation of the *instantaneous modulus* (here expressed as G_{inst}) as a function of strain, depends on

fibrinogen concentration and it is illustrated on Figure 17. For low fibrinogen concentrations (from 3 to 5 mg/ml) G_{inst} increases steadily with increasing strain. For higher fibrinogen concentrations (from 10 to 25 mg/ml), gels present a strain stiffening behaviour until they reach a shear strain (γ) of 10%, then the gels begin to soften until γ = 30%, and finally they strain-stiffen again until failure. Weigandt *et al* proposed that the nonlinear mechanical properties of fibrin clots are the result of a reduction of lateral entropic fluctuations at low strains and a transition between bending and stretching at higher strain values.

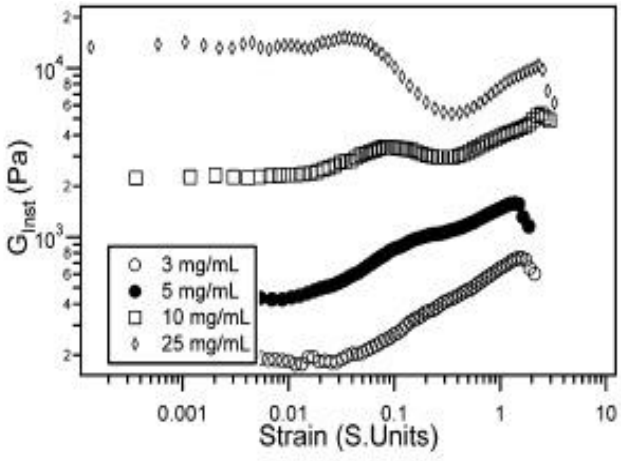

Figure 17. Nonlinear response of fibrin clots at 3, 5, 10 and 25 mg/ml. Image from Weigandt et al.

Piechocka *et al.* [65,83] performed rheological measurements to investigate the physical origin of the strength of fibrin gels. Increasing levels of shear strain induce a succession of elastic responses similar to those previously observed by Weigandt [60]. This work proposes a theoretical model to explain these observations in terms of the architecture of the fibres, which are considered as bundles of semiflexible protofibrils loosely connected by flexible linker chains. As can be seen on Figure 18., where is represented the differential modulus K^* (noted as the instantaneous modulus G_{inst} by Weingandt *et al.*) as a function of stress, this model proposes that the bundlelike structure of fibrin fibres accounts for the elastic properties of fibrin. However, it was not possible to determine which molecular regions cause the intrinsic nonlinearities of the fibres.

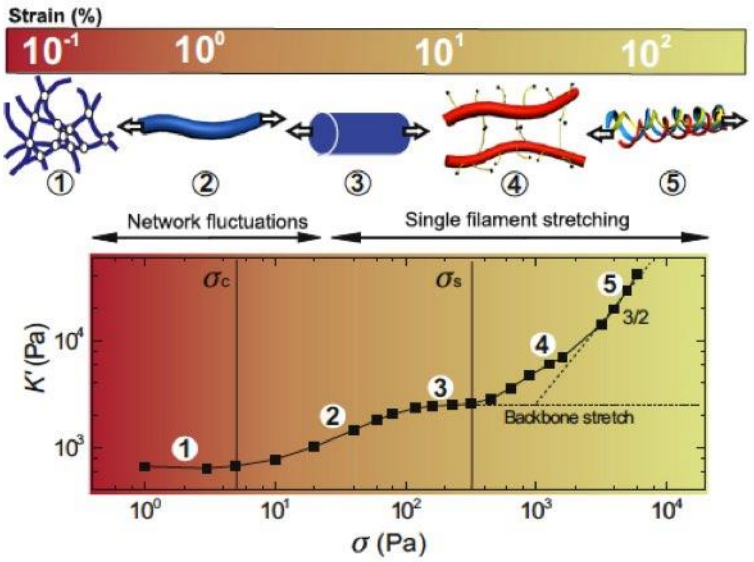

Figure 18.Strain stiffening response of fibrin gels [65]

Munster *et al.* [96] determined the strain history dependence of the nonlinear mechanical response of fibrin clots when large strains are repeatedly and symmetrically applied to the clot. Moreover, Munster *et al.* demonstrated that the dynamic evolution of this mechanical response is caused by a shift on the nonlinear stress-strain relationship at high strains. This repeated strain leads to a pronounced working behaviour of the fibrin networks. The imposed loading does not weaken the the underlying matrices but instead delays the occurrence of the strain stiffening.

By using also confocal microscopy it was demonstrated that this behaviour does not result from the damage of the clot (rupture of the fibres or detachment of the branch points), but from persistent lengthening of individual fibres caused by an interplay between fibre stretching and fibre buckling when networks are repeatedly stretched. Also, the role of covalent cross linking of fibrin (also for collagen) inhibits the shift of the nonlinear response, which suggests that the molecular origin of the lengthening of individual fibres may be slipping of monomers within the fibres. Thus, the internal plasticity of fibrin fibrous architecture leads to a material which adapts its mechanical response to the external perturbations.

In 2013, Munster *et al.* [97] also determined the structure of fibrin clots and the differences on the scenarios of failure (or rupture) of clots when they polymerize under the application of a mechanical perturbation at different strain amplitudes (from 0 to

90%). Results showed significant differences on the nonlinear characterization of fibrin clots depending on strain. An increase of the characteristic strain for the onset of nonlinearity, increased with increased perturbation amplitude. Several characteristic regimes, as was observed by Piechocka *et al.* [65](cf. Figure 18) appear for the nonlinear response. For increasing initial perturbations, the transitions between regimes were shifted to larger strains, and the clots attained failure successively later. Bundle formation with increasing strain perturbation causes inhomogeneities on the structure which can accommodate a proportionally larger deformation until they are straightened.

9.2 Conclusions

The observed increase of rigidity on fibrin clots during polymerization has led to an extended work of their mechanical properties. Fibrin clots are known to be viscoelastic materials However, they show exceptional nonlinear rheological properties such as stiffening as the strain increases as well as negative normal stresses.

Several models and experimental techniques have been developed to determine the origin of the relation between these nonlinear properties and the structure of fibrin. Nevertheless, the origin of the strain stiffening properties of fibrin, and its behaviour under repeated strain, are still under debate.

10 General Conclusion and outstanding questions

Since the first observations of fibrin clots on the XVIIIth century, the main objective has been to understand how fibrin polymerizes and to determine its functional properties in conditions as close as possible to *in vivo* in order to characterize, understand and ultimately cure coagulation-related pathologies.

As a matter of fact, several recent studies have highlighted the relation between cardiovascular pathologies and fibrin clots abnormal structure [98,99]. In addition, the mechanical properties of such clots should also determine if they could break free and migrate in the circulation, forming an embolus which can generate an embolism. Therefore, the characterization and modelling of the relation between the structure of fibrin clots and their rheological properties is of great importance. However, in most existing works on fibrin rheology, fibrin's nanostructure is held constant [59,60,65,96], since only fibrinogen concentration was varied. To investigate this structure-mechanics relationship, the fibrin clot's structure must be modified without changing the molecular interactions inside the fibres, and hence keeping the pH and ionic strength at their physiological values.

While this may seem very difficult to do, Huang *et al.* [76,77] determined that the nature of fibrinogen impacts strongly fibrin polymerization. In particular, the turbidity of a fibrin clot polymerized from fibrinogen monomers is twice larger than for a fibrin clot polymerized from the initial polydisperse fibrinogen preparation. Thus, fibrinogen polydispersity seems to provide a new control parameter of the structure of fibrin clots. The three main questions of this PhD are the following:

- Is the nanostructure of fibrin clots determined by the polydispersity profiles of the fibrinogens or is it due to some other compositional differences, such as co-purified proteins or γ' chains concentration?
- How is the structure modified at each length scale?
- How does the nanostructure influence the mechanical properties of fibrin clots?

To do so, we first determined the origin of the influence of the nature of fibrinogen by comparing three different commercial fibrinogens. We determined their physicochemical properties using gel filtration chromatography and mass spectroscopy. Second, we combined several experimental techniques such as SAXS, spectrophotometry and confocal microscopy to quantify the effect of polydispersity profiles of fibrinogens on the nano- and microstructure of fibrin clots. Finally, we characterized the linear and nonlinear rheological properties of fibrin clots obtained from mono and polydisperse fibrinogens.

References

1 Versteeg HH, Heemskerk JWM, Levi M, Reitsma PH. New Fundamentals in Hemostasis. *Physiol Rev* 2013; **93**.

2 Gale AJ. Continuing education course #2: current understanding of hemostasis. *Toxicol Pathol* 2011; **39**: 273–80.

3 Henschen-Edman AH. Fibrinogen non-inherited heterogeneity and its relationship to function in health and disease. *Ann N Y Acad Sci* Blackwell Publishing Ltd; 2006; **936**: 580–93.

4 Hantgan RR, Hermans J. Assembly of Fibrin. *Assembly* 1979; **254**: 11272–81.

5 Ferry JD. The Mechansim of Polymerization of Fibrinogen. *Proc Natl Acad Sci U S A* 1952; **38**: 566–9.

6 Greene RW. Light scattering studies of fibrin clots. *J Clin Invest* 1952; **31**: 969–75.

7 Yeromonahos C, Polack B, Caton F. Nanostructure of the fibrin clot. *Biophys J* Biophysical Society; 2010; **99**: 2018–27.

8 Riddel JP, Aouizerat BE, Miaskowski C, Lillicrap DP. Theories of blood coagulation. *J Pediatr Oncol Nurs* 2007; **24**: 123–31.

9 Florkin M. Studies in the physical chemistry of proteins VII. *Nature* 1952; **170**: 518–20.

10 Howell WH. The clotting of blood as seen with the ultramicroscope. *Am J Physiol -- Leg Content* 1914; **35**.

11 Bailey K, Astbury WT, Rudall KM. Fibrinogen and fibrin as members of the keratin-myosin group. *Nature* 1943; **151**: 716–7.

12 Shulman S, Ferry J. The The Conversion of Fibrinogen to Fibrin. II. Influence of pH and Ionic Strength on Clotting Time and Clot Opacity. American Chemical Society; 1949; .

13 Shulman S, Katz S, Ferry JD. The conversion of fibrinogen to fibrin: xiii. dissolution of fibrin and inhibition of clotting by various neutral salts. *J Gen Physiol* Rockefeller University Press; 1953; **36**: 759–66.

14 Torbet J, Freyssinet J-M, Hudry-Clergeon G. Oriented fibrin gels formed by polymerization in strong magnetic fields. *Nature* Nature Publishing Group; 1981; **289**: 91–3.

15 Freyssinet JM, Torbet J, Hudry-Clergeon G, Maret G. Fibrinogen and fibrin structure and fibrin formation measured by using magnetic orientation. *Proc Natl Acad Sci U S A* 1983; **80**: 1616–20.

16 Henschen A. Paper electrophoretic pattersn+ mobilities of unmodified sulfitolysed+ reduced-alkylated fibrinogen+ fibrin in buffered 6 M UREA. *Ark Kemi* ROYAL SWEDISH ACAD SCIENCES PUBL DEPT BOX 50005, S-104 05 STOCKHOLM, SWEDEN; 1964; **22**: 397.

17 Lottspeich F, Henschen A. Amino acid sequence of human fibrin. Preliminary note on the completion of the gamma-chain sequence. *Hoppe-Seyler's Zeitschrift für Physiol Chemie* 1977; **358**: 935–8.

18 Doolittle RF, Watt KWK, Cottrell BA, Strong DD, Riley M. The amino acid sequence of the α-chain of human fibrinogen. *Nature* 1979; **280**: 464–8.

19 Marder VJ, Aird WC, Bennet JS, Shulman S, GIlber C. White I. Hemostasis and Thrombosis. *J.B. Lippincott Company.* 1982.

20 Tooney NM, Cohen C. Microcrystals of a modified fibrinogen. *Nature* 1972; **237**: 23–5.

21 Doolittle RF, Spraggon G, Everse SJ. Crystal structures of fragment D from human fibrinogen and its crosslinked counterpart from fibrin. *Nature* Nature Publishing Group; 1997; **389**: 455–62.

22 Wolpers C, Ruska H. Strukturuntersuchungen zur Blutgerinnung. *Klin Wochenschr* 1939; **18**: 1077–81.

23 Van Zandt Hawn C. THE FINE STRUCTURE OF CLOTS FORMED FROM PURIFIED BOVINE FIBRINOGEN AND THROMBIN: A STUDY WITH THE ELECTRON MICROSCOPE. *J Exp Med* 1947; **86**: 285–92.

24 Hall BCE, Ph D, Slayter HS. The Fibrinogen Molecule : Its Size , Shape , and Mode of Polymerization. 1958; .

25 Hall CE. The Fibrinogen Molecule: Its Size, Shape, and Mode of Polymerization. *J Cell Biol* 1959; **5**: 11–27.

26 Karges HE, Kuhn K. The Cross Striation Pattern of the Fibrin Fibril. *Eur J Biochem* Blackwell Publishing Ltd; 1970; **14**: 94–7.

27 Ferry JD, Shulman S, Gutfreund K, Katz S. The Conversion of Fibrinogen to Fibrin. XI. Light Scattering Studies on Clotting Systems Inhibited by Hexamethylene Glycol1. *J Am Chem Soc* 1952; **74**: 5709–15.

28 Madrazo J, Brown JH, Litvinovich S, Dominguez R, Yakovlev S, Medved L, Cohen C. Crystal structure of the central region of bovine fibrinogen (E5 fragment) at 1.4-A resolution. *Proc Natl Acad Sci U S A* 2001; **98**: 11967–72.

29 Fowler WE, Hantgan RR, Hermans J, Erickson HP. Structure of the fibrin protofibril. *Proc Natl Acad Sci* 1981; **78**: 4872–6.

30 Medved' L, Ugarova T, Veklich Y, Lukinova N, Weisel J. Electron microscope investigation of the early stages of fibrin assembly. Twisted protofibrils and fibers. *J Mol Biol* 1990; **216**: 503–9.

31 Weisel JW, Phillips GN, Cohen C. A model from electron microscopy for the molecular structure of fibrinogen and fibrin. *Nature* 1981; **289**: 263—267.

32 Weisel JW, Phillips GN, Cohen C. THE STRUCTURE OF FIBRINOGEN AND FIBRIN: II. ARCHITECTURE OF THE FIBRIN CLOT. *Ann N Y Acad Sci* Blackwell Publishing Ltd; 1983; **408**: 367–79.

33 Bernocco S, Ferri F, Profumo A, Cuniberti C, Rocco M. Polymerization of Rod-Like Macromolecular Monomers Studied by Stopped-Flow, Multiangle Light Scattering: Set-Up, Data Processing, and Application to Fibrin Formation. *Biophys J* 2000; **79**: 561–83.

34 Ferri F, Greco M, Rocco M. On the determination of the average molecular weight, radius of gyration, and mass/length ratio of polydisperse solutions of polymerizing rod-like macromolecular monomers by multi-angle static light scattering. *Macromol Symp* WILEY-VCH Verlag; 2000; **162**: 23–44.

35 Ferri F, Greco M, Arcovito G, Bassi F, De Spirito M, Paganini E, Rocco M. Growth kinetics and structure of fibrin gels. *Phys Rev E* 2001; **63**: 31401.

36 Janmey PA. Kinetics of formation of fibrin oligomers. I. Theory. *Biopolymers* Wiley Subscription Services, Inc., A Wiley Company; 1982; **21**: 2253–64.

37 Casassa EF. Light Scattering from Very Long Rod-Like Particles and an Application to Polymerized Fibrinogen. *J Chem Phys* 1955; **23**: 596.

38 Yang Z, Mochalkin I, Doolittle RF. A model of fibrin formation based on crystal structures of fibrinogen and fibrin fragments complexed with synthetic peptides. *Proc Natl Acad Sci U S A* 2000; **97**: 14156–61.

39 Weisel JW. Fibrin assembly. Lateral aggregation and the role of the two pairs of fibrinopeptides. *Biophys J* 1986; **50**: 1079–93.

40 Mosesson MW, DiOrio JP, Müller MF, Shainoff JR, Siebenlist KR, Amrani DL, Homandberg GA, Soria J, Soria C, Samama M. Studies on the ultrastructure of fibrin lacking fibrinopeptide B (beta-fibrin). *Blood* American Society of Hematology; 1987; **69**: 1073–81.

41 Everse SJ, Spraggon G, Veerapandian L, Riley M, Doolittle RF. Crystal structure of fragment double-D from human fibrin with two different bound ligands. *Biochemistry* 1998; **37**: 8637–42.

42 Bale MD, Janmey PA, Ferry JD. Kinetics of formation of fibrin oligomers. II. Size distributions of ligated oligomers. *Biopolymers* Wiley Subscription Services, Inc., A Wiley Company; 1982; **21**: 2265–77.

43 Weisel JW. Fibrinogen and Fibrin. *Adv Protein Chem* 2005; **70**: 247–99.

44 Weisel JW. The electron microscope band pattern of human fibrin: Various stains, lateral order, and carbohydrate localization. *J Ultrastruct Res Mol Struct Res* 1986; **96**: 176–88.

45 Weisel JW, Nagaswami C, Makowski L. Twisting of fibrin fibers limits their radial growth. *Proc Natl Acad Sci U S A* 1987; **84**: 8991–5.

46 Blombäck B, Carlsson K, Hessel B, Liljeborg A, Procyk R, Åslund N. Native fibrin gel networks observed by 3D microscopy, permeation and turbidity. *Biochim Biophys Acta (BBA)/Protein Struct Mol* 1989; **997**: 96–110.

47 Blombäck B, Okada M, Forslind B, Larsson U. Fibrin gels as biological filters and interfaces. *Biorheology* 1984; **21**: 93–104.

48 Blombäck B, Carlsson K, Fatah K, Hessel B, Procyk R. Fibrin in human plasma: Gel architectures governed by rate and nature of fibrinogen activation. *Thromb Res* 1994; **75**: 521–38.

49 Standeven KF, Ariëns RAS, Grant PJ. The molecular physiology and pathology of fibrin structure/function. *Blood Rev* 2005; **19**: 275–88.

50 Shen LL, Hermans J, Mcdonagh J, Mcdonagh RP, Carr M, Hill C. Effects of calcium ion and covalent crosslinking on formation and elasticity of fibrin gels. *Thromb Res* 1975; **6**: 255–65.

51 Roberts WW, Kramer O, Rosser RW, Nestler FHM, Ferry JD. Rheology of fibrin clots I. *Biophys Chem* 1974; **1**: 152–60.

52 Ryan E a., Mockros LF, Weisel JW, Lorand L. Structural Origins of Fibrin Clot Rheology. *Biophys J* Elsevier; 1999; **77**: 2813–26.

53 Roska FJ, Ferry JD. Studies of Fibrin Film. II. Small-Angle X-Ray Scattering. *Biopolymers* 1982; **21**: 1833–45.

54 Roska FJ, Ferry JD. Studies of fibrin film. I. Stress relaxation and birefringence. *Biopolymers* Wiley Subscription Services, Inc., A Wiley Company; 1982; **21**: 1811–32.

55 Müller MF, Ferry JD, Lin JS. Small-angle X-ray scattering studies of fibrin film: comparisons of fine and coarse films prepared with thrombin and ancrod. *Biopolymers* 1989; **28**: 1011–8.

56 Torbet J. Fibrin assembly after fibrinopeptide A release in model systems and human plasma studied with magnetic birefringence. *Biochem J* 1987; **244**.

57 Carr ME, Hermans J. Size and Density of Fibrin Fibers from Turbidity. *Macromolecules* 1978; **11**: 46–50.

58 Guthold M, Liu W, Stephens B, Lord ST, Hantgan RR, Erie DA, Taylor RM, Superfine R. Visualization and Mechanical Manipulations of Individual Fibrin Fibers Suggest that Fiber Cross Section Has Fractal Dimension 1.3. *Biophys J* 2004; **87**: 4226–36.

59 Weigandt KM, Pozzo DC, Porcar L. Structure of high density fibrin networks probed with neutron scattering and rheology. *Soft Matter* 2009; **5**: 4321.

60 Weigandt KM, Porcar L, Pozzo DC. In situ neutron scattering study of structural transitions in fibrin networks under shear deformation. *Soft Matter* 2011; **7**: 9992.

61 Missori M, Papi M, Maulucci G, Arcovito G, Boumis G, Bellelli A, Amiconi G, De Spirito M. Cl- and F- anions regulate the architecture of protofibrils in fibrin gel. *Eur Biophys J* 2010; **39**: 1001–6.

62 Whittaker P, Przyklenk K. Fibrin architecture in clots: A quantitative polarized light microscopy analysis. *Blood Cells, Mol Dis* Elsevier Inc.; 2009; **42**: 51–6.

63 Yermolenko IS, Lishko VK, Ugarova TP, Magonov SN. High-resolution visualization of fibrinogen molecules and fibrin fibers with atomic force microscopy. *Biomacromolecules* 2011; **12**: 370–9.

64 Lang NR, Münster S, Metzner C, Krauss P, Schürmann S, Lange J, Aifantis KE, Friedrich O, Fabry B. Estimating the 3D Pore Size Distribution of Biopolymer Networks from Directionally Biased Data. *Biophys J* 2013; **105**: 1967–75.

65 Piechocka IK, Bacabac RG, Potters M, Mackintosh FC, Koenderink GH. Structural hierarchy governs fibrin gel mechanics. *Biophys J* Biophysical Society; 2010; **98**: 2281–9.

66 Wiltzius P, Dietler G, Kanzig W, Hofmann V, H??berli A, Straub PW. Fibrin aggregation before sol-gel transition. *Biophys J* 1982; **38**: 123–32.

67 Landis WJ, Waugh DF. Interactions of bovine fibrinogen and thrombin. Early events in the development of clot structure. *Arch Biochem Biophys* 1975; **168**: 498–511.

68 De Cristofaro R, Di Cera E. Phenomenological analysis of the clotting curve. *J Protein Chem* Kluwer Academic Publishers-Plenum Publishers; 1991; **10**: 455–68.

69 Weisel JW, Nagaswami C. Computer modeling of fibrin polymerization kinetics correlated with electron microscope and turbidity observations: clot structure and assembly are kinetically controlled. *Biophys J* The Biophysical Society; 1992; **63**: 111–28.

70 Meade TW, Brozovic M, Chakrabarti RR, Haines AP, Imeson JD, Mellows S, Miller GJ, North WRS, Stirling Y, Thompson SG. Haemostatic Function and Ischaemic Heart Disease: Principal Results of the Northwick Park Heart Study. *Lancet* 1986; **328**: 533–7.

71 Ferri F, Greco M, Arcòvito G, De Spirito M, Rocco M. Structure of fibrin gels studied by elastic light scattering techniques: Dependence of fractal dimension, gel crossover length, fiber diameter, and fiber density on monomer concentration. *Phys Rev E* 2002; **66**: 11913.

72 Blombäck B, Bark N. Fibrinopeptides and fibrin gel structure. *Biophys Chem* 2004; **112**: 147–51.

73 Chernysh IN, Weisel JW. Dynamic imaging of fibrin network formation correlated with other measures of polymerization. *Blood* 2008; **111**.

74 Chernysh IN, Weisel JW, Dc W. Dynamic imaging of fibrin network formation correlated with other measures of polymerization Plenary paper Dynamic imaging of fibrin network formation correlated with other measures of polymerization. *Blood* 2011; **111**: 4854–61.

75 Domingues MM, Macrae FL, Duval C, McPherson HR, Bridge KI, Ajjan RA, Ridger VC, Connell SD, Philippou H, Ariëns RAS. Thrombin and fibrinogen γ' impact clot structure by marked effects on intrafibrillar structure and protofibril packing. *Blood* 2016; **127**: 487–95.

76 Huang L, Lord ST. The isolation of fibrinogen monomer dramatically influences fibrin polymerization. *Thromb Res* Elsevier; 2013; **131**: e258-63.

77 Huang L, Hsiao JP-L, Powierza C, Taylor RM, Lord ST. Does topology drive fiber polymerization? *Biochemistry* American Chemical Society; 2014; **53**: 7824–34.

78 Gabriel DA, Muga K, Boothroyd EM. The effect of fibrin structure on fibrinolysis. *J Biol Chem* 1992; **267**: 24259–63.

79 Ajjan RA, Standeven KF, Khanbhai M, Phoenix F, Gersh KC, Weisel JW, Kearney MT, Ari??ns RAS, Grant PJ. Effects of aspirin on clot structure and fibrinolysis using a novel in vitro cellular system. *Arterioscler Thromb Vasc Biol* 2009; **29**: 712–7.

80 Yeromonahos C, Marlu R, Polack B, Caton F. Antithrombin-independent effects of heparins on fibrin clot nanostructure. *Arterioscler Thromb Vasc Biol* 2012; **32**: 1320–4.

81 Fatah K, Silveira A, Tornvall P, Karpe F, Blomback M, Hamsten A. Proneness to formation of tight and rigid fibrin gel structures in men with myocardial infarction at a young age. *Thromb Haemost* Schattauer; 1996; **76**: 535–40.

82 Collet JP, Park D, Lesty C, Soria J, Soria C, Montalescot G, Weisel JW. Influence of fibrin network conformation and fibrin fiber diameter on fibrinolysis speed: dynamic and structural approaches by confocal microscopy. *Arterioscler Thromb Vasc Biol* 2000; **20**: 1354–61.

83 Piechocka IK, Jansen KA, Broedersz CP, Kurniawan NA, MacKintosh FC, Koenderink GH. Multi-scale strain-stiffening of semiflexible bundle networks. *Soft Matter* Royal Society of Chemistry; 2016; **12**: 2145–56.

84 Weisel JW. The mechanical properties of fibrin for basic scientists and clinicians. *Biophys Chem* 2004; **112**: 267–76.

85 Collet JP, Allali Y, Lesty C, Tanguy ML, Silvain J, Ankri A, Blanchet B, Dumaine R, Gianetti J, Payot L, Weisel JW, Montalescot G. Altered Fibrin Architecture Is Associated With Hypofibrinolysis and Premature Coronary Atherothrombosis. *Arterioscler Thromb Vasc Biol* Lippincott Williams & Wilkins; 2006; **26**: 2567–73.

86 Gerth C, Roberts WW, Ferry JD. Rheology of fibrin clots II. Linear viscoelastic behavior in shear creep. *Biophys Chem* 1974; **2**: 208–17.

87 Ferry JD. Structure and Rheology of Fibrin Networks. *Biological and Synthetic Polymer Networks*. Dordrecht: Springer Netherlands; 1988. p. 41–55.

88 Nelb GW, Gerth C, Ferry JD, Lorand L. Rheology of fibrin clots: III. Shear creep and creep recovery of fine ligated and coarse unligated clots. *Biophys Chem* Elsevier; 1976; **5**: 377–87.

89 Brown André EX, Litvinov RI, Discher DE, Weisel JW. Forced Unfolding of Coiled-Coils in Fibrinogen by Single-Molecule AFM. *Biophys J* 2007; **92**: L39–41.

90 Brown AEX, Litvinov RI, Discher DE, Purohit PK, Weisel JW. Multiscale mechanics of fibrin polymer: gel stretching with protein unfolding and loss of water. *Science* 2009; **325**: 741–4.

91 Liu W. Fibrin Fibers Have Extraordinary Extensibility and Elasticity. *Science (80-)* 2006; **313**: 634–634.

92 Liu W, Carlisle CR, Sparks EA, Guthold M. The mechanical properties of single fibrin fibers. *J Thromb Haemost* 2010; **8**: 1030–6.

93 Bale MD, Muller MF. Rheological Studies of Creep and Creep Recovery of Unligated Fibrin Clots : Comparison of Clots Prepared with Thrombin and Ancrod. 1985; **24**: 461–82.

94 Janmey P a. Rheology of Fibrin Clots. VI. Stress Relaxation, Creep, and Differential Dynamic Modulus of Fine Clots in Large Shearing Deformations. *J Rheol (N Y N Y)* 1983; **27**: 135.

95 Janmey PA, McCormick ME, Rammensee S, Leight JL, Georges PC, MacKintosh FC. Negative normal stress in semiflexible biopolymer gels. *Nat Mater* 2007; **6**: 48–51.

96 Münster S, Jawerth LM, Leslie BA, Weitz JI, Fabry B, Weitz DA. Strain history dependence of the nonlinear stress response of fibrin and collagen networks. *Proc Natl Acad Sci U S A* National Academy of Sciences; 2013; **110**: 12197–202.

97 Münster S, Jawerth LM, Fabry B, Weitz DA. Structure and mechanics of fibrin clots formed under mechanical perturbation. *J Thromb Haemost* 2013; **11**: 557–60.

98 Undas A, Ariëns RAS. Fibrin clot structure and function: A role in the pathophysiology of arterial and venous thromboembolic diseases. *Arterioscler Thromb Vasc Biol* 2011; **31**: e88-99.

99 Dassi C. La Fibrinographie : Une méthode multi-longueurs d'ondes pour la détermination de la structure du caillot en plasma. University Joseph Fourier; 2016.

100 Yeromonahos C. Nanostructure des fibres de fibrine. University Joseph Fourier; 2011.

101 Medved L, Weisel JW. Recommendations for nomenclature on fibrinogen and fibrin. *J Thromb Haemost* 2009; **7**: 355–9.

Chapter 2

Materials and Methods

In this chapter we review the general aspects of the main experimental techniques and methods generally used to characterize the nature of fibrinogen and the structural and mechanical properties of fibrin. Finally, we also describe the different materials and experimental setups that we have implemented to carry out this PhD work

1 Introduction

In this Materials and Methods chapter, first we describe the protocols used for the preparation of samples during this PhD project. Second, we describe the physicochemical techniques used to characterize the nature of fibrinogen itself. Third, we portray the imaging techniques applied in order to visualize fibrin networks. We then describe the scattering systems used to study the longitudinal and lateral structure of fibrin fibres. Finally, we present the linear and nonlinear rheology methods used to study the mechanical properties of fibrin clots and their rupture scenarios.

2 Sample preparation

During this project, the following three different commercial fibrinogens were used:

- Clottafact (Laboratoire Français du Fractionnement et des Biotechnologies, Les Ulis, France)
- Fib1 (Enzyme Research Laboratories, Swansea, UK)
- Riastap (CSL Behring, Paris, France)

The fibrinogens were reconstituted using the manufacturer's guidelines and then dialyzed twice overnight against HEPES buffer (140 mM NaCl, 20 mM HEPES, 5 mM CaCl2, pH 7.4), aliquoted and kept frozen at -80°C. The concentration of each fibrinogen was obtained using the Clauss method [1].

The polymerization of the fibrin clots from these three different fibrinogen sources was activated with human thrombin purchased from Cryopep (Montpellier, France) as a 12 μL solution containing 298,9 IU. The solution was diluted to 200 IU/ml in a MES buffer (20mM MES, 50mM NaCl, pH 6.5), aliquoted and kept frozen at -80°C.

Before polymerization, a strict reconstitution protocol was established in order to obtain a good reproducibility of fibrin clots formation. First, fibrinogen aliquots are thawed at 37°C for 5 minutes and equilibrated at room temperature for another 5 minutes before use. Second, thrombin is thawed in a 37°C bath for 1 minute and diluted in HEPES buffer and immediately used.

Fibrin clots were formed by incubating fibrinogen (0.4, 1, 3 and 6mg/ml) with 0.1 IU/ml thrombin.

3 Physicochemical characterization of fibrinogens

Physicochemical and biochemical techniques are very important for the characterization of molecules such as fibrinogen. The gel filtration chromatography and mass spectrometry techniques provide information about the molecular distribution of the specimens and set the basis of posterior investigations on structure, kinetics and mechanical properties of fibrin.

3.1 Gel filtration chromatography

3.1.1 Method

Gel filtration separates proteins solely on the basis of differences in molecular size. Separation is achieved using porous beads embedded in a matrix. The molecules have different degrees of access to the porosity of the beads since smaller molecules diffuse further into the pores of the beads and therefore move through the matrix more slowly. Larger molecules enter less or not at all in the pores of the beads, moving between the beads more quickly.

The matrix is packed into a chromatographic column to which the sample mixture is applied. The separation is accomplished by passing an aqueous buffer through the column (mobile phase). Protein molecules that are confined in the volume outside the beads will be swept through the column by the mobile phase and the sample is thus eluted in decreasing order of size. The protein zones eluted are detected by an in-line UV monitor and the fractions are collected for subsequent specific analysis [2]. A schematized gel filtration system is illustrated in Figure 19.

3.1.2 Experimental setup

The three different fibrinogens (100 µg) were injected onto an UPLC BEH450 SEC column (300 x 4.6 mm, 1.7 µm) equilibrated at 30°C using an ACQUITY UPLC H-class bio system (Waters, Milford, MA, USA). The following mobiles phases were used: (a) NaH_2PO_4 100mM, (b) Na_2HPO_4 125mM, (c) NaCl 1M and (d) H_2O. The flow was set at 0.3 ml/min and the Auto Blend Plus function was used to mix the mobiles phases in order to reach a final mobile phase at pH 7.0 and 250mM NaCl to separate species based on size.

After separation, high molecular weight (HMW), fibrinogen monomers, and low molecular weight (LMW) species were detected by UV at 280nm.

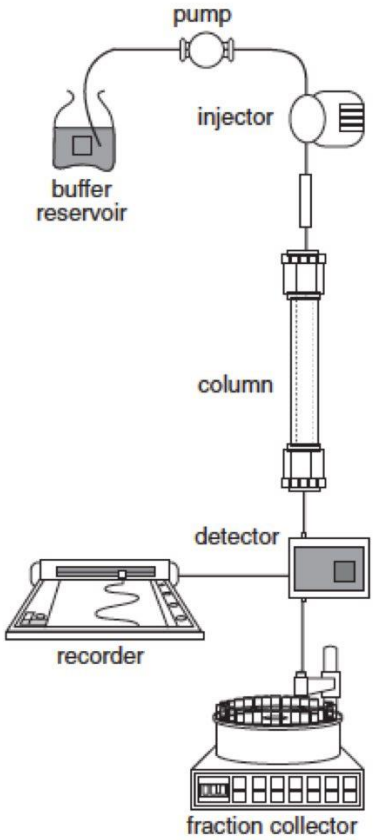

Figure 19. Chromatography system schematized

3.2 Mass spectrometry

3.2.1 Method

Mass spectrometry is an analytical technique used to quantify known materials, to identify unknown compounds within a sample and to elucidate the structure and chemical properties of different molecules.

The first step in the mass spectrometric analysis of compounds is the production of gas phase ions of the compound, basically by electron ionization. This molecular ion undergoes fragmentation. Each primary product ion derived from the molecular ion, in turn, undergoes fragmentation, and so on. The ions are separated in the mass

spectrometer according to their mass-to-charge ratio, and are detected in proportion to their abundance. A mass spectrum of the molecule is thus produced. It displays the result in the form of a plot of ion abundance versus mass-to-charge ratio. Ions provide information concerning the nature and the structure of their precursor molecule. In the spectrum of a pure compound, the molecular ion, if present, appears at the highest value of m/z (followed by ions containing heavier isotopes) and gives the molecular mass of the compound.

In Figure 20 we present a schematization of the major components of a mass spectrometry system:

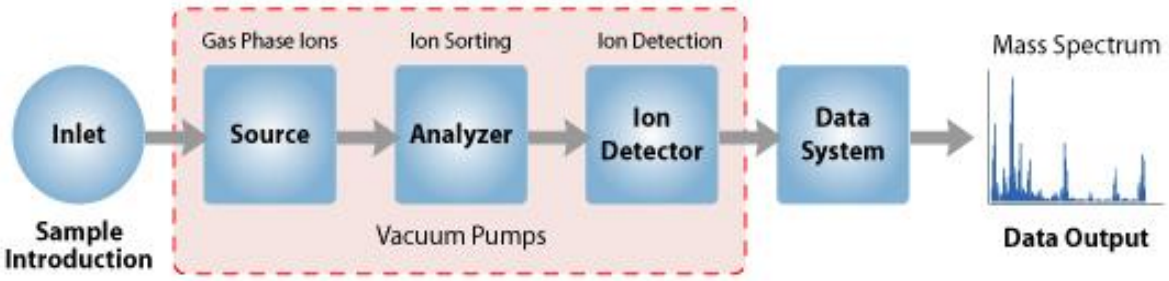

Figure 20. Mass spectrometry schema of functioning

3.2.2 Experimental setup

Fibrinogens (100 µg) were vacuum-dried and dissolved in 35µL of a 8M urea and 0.4mM ammonium carbonate solution pH 8.0. Reduction was done by adding 10µL of a 40mM dithiothreitol (DTT) solution in water and incubating the resulting mixture for 20 min at 50°C. After cooling at room temperature, 10µL of a 80mM iodoacetamide (IAM) solution in water were added and the solution was incubated at room temperature for 20 min in the dark. RP-HPLC was performed using an ACQUITY UPLC system (Waters, Milford, MA, USA). An amount of 20µg of sample was injected on a Pursuit 3 diphenyl reverse phase column (150 x 2.0mm, 3µm) equilibrated at 70°C and operated at a flow rate of 200µL/min (Agilent, Santa Clara, CA, USA). An aqueous solution containing 0.1% of trifluoroacetic acid (TFA) and acetonitrile (MeCN) containing 0.1% TFA were respectively used as buffer A and buffer B; proteins were eluted by using an increasing gradient of buffer B. After separation, fibrinogen reduced and alkylated chains were

detected by UV at 280nm and MS analysis was achieved by interfacing the UV detector output to a SYNAPT G2-S HDMS mass spectrometer (Waters, Milford, MA, USA) scanning from m/z 500 to 2000.

3.3 Experimental measurements

Gel filtration chromatography and mass spectrometry experiments were kindly performed by Guillaume Chevreux, head of of the "Laboratoire de Caractérisation Structurale" of LFB Biotechnologies.

4 Microscopy

4.1 Principles

Microscopy is a tool commonly used to produce images of microscopic features of objects or systems. This technique provides information in real space for two and three-dimensional samples.

Microscopes generally use two convex lenses to obtain magnification and the samples are illuminated with radiation. The system is usually formed by an objective lens, ocular lens tube, stage and reflector. Samples are placed on the stage and magnified through the objective lens. When the target is focused, a magnified image of the sample is observed through the ocular lens. This principle is illustrated in Figure 21.

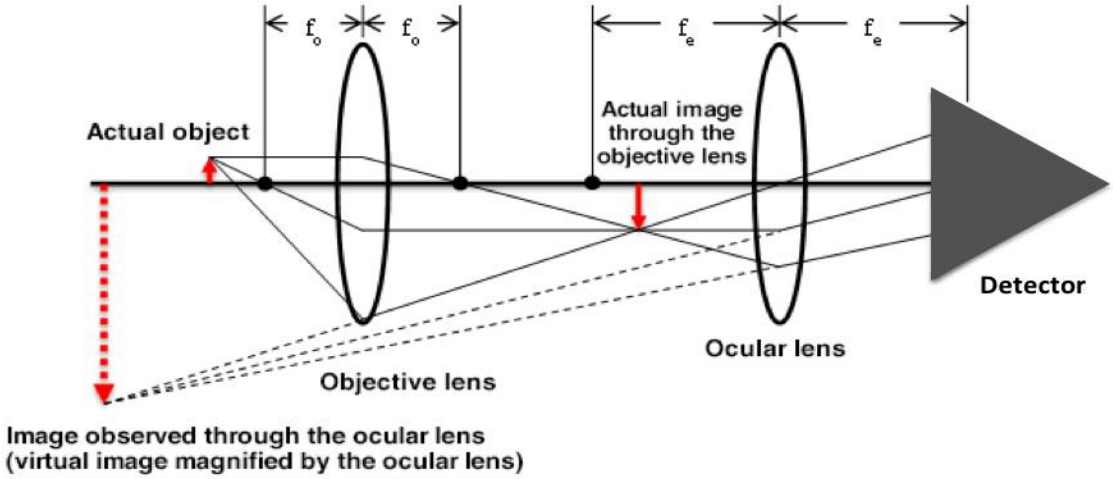

Figure 21. Schematized principle of magnified observation of a sample through an optical microscope

4.2 Types of microscopy

There exist three types of microscopy: *optical microscopy*, including fluorescence microscopy (classic, confocal and deconvolution), *electron microscopy* and *atomic force microscopy.*

4.2.1 Fluorescent Microscopy 3D: classic, confocal and deconvolution

Optical microscopy, appeared during the 17th century, implies that visible light is transmitted across the samples and a system of lenses in order to magnify images of small samples (as previously described in Figure 21). The resolution, or the ability of these microscopes to reveal adjacent structural details as distinct and separate is typically of 1μm.

Fluorescent microscopy is used to image structures previously marked with a fluorochrome. This technique is based on fluorescence, which is the property of certain elements to emit light after having absorbed electromagnetic radiation of higher energy. Fluorescent microscopy has an important limitation on the loss of contrast because of the fluorescence emitted through the planes adjacent to the focal plane.

Confocal microscopy is an optical imaging technique developed by Marvin Minsky in the 1950's to overcome some limitations of classic wide-field fluorescence microscopes. The depth of focus of conventional microscopes goes as far into the specimen as the light can penetrate, while a confocal microscope only "sees" images one depth level at a time. This optical imaging technique is based on point illumination, which eliminates out-of-focus light, giving highly resolved focal planes and high contrast images. Confocal microscopy also allows the scanning of a sample along the z-axis and, consequently, the reconstitution of a three dimensional image through the stacking of all focal planes. Figure 22 itemizes the structure of a confocal microscopy and schematizes its functioning.

The lateral resolution of confocal microscopes is typically of 200nm and the depth of field is 600nm. The main limitation of this technique is what is referred to as *photobleaching*: the process in which the molecular structure of a fluorochrome is altered as a result of absorption of excitation light, which renders the fluorochrome non-fluorescent.

Deconvolution microscopy appeared during the 1990's intending to surpass confocal microscopy limits. A pinhole is no longer used to suppress the out-of-focus planes, but images are treated with algorithmic techniques. This technique can use lower luminal intensities allowing to image simultaneously different focal planes of a sample and for a longer time.

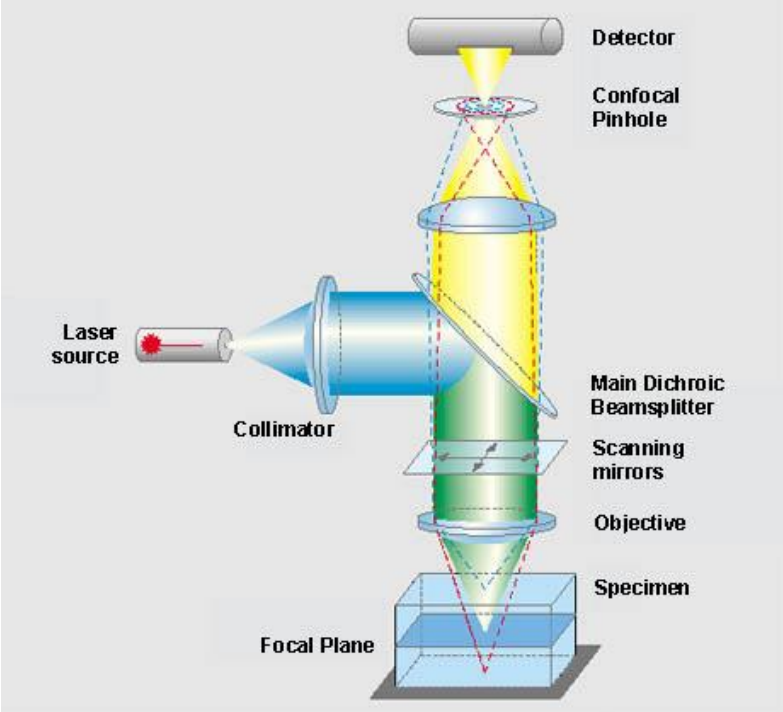

Figure 22. Confocal microscopy schema. Source: ETH Zurich

4.2.2 Experimental setup

Among the different imaging techniques described, in this thesis we chose to use confocal microscopy to perform two and three dimensional profiles of fibrin samples. This technique allows the visualization of fibrin networks organization at the micron scale. Fibrin samples were visualized with a TCS SP8 confocal microscopy (Leica, Wetzlar, Germany) combined with a 40x/1.3 NA or a 63x/1.4 NA oil immersion objectives and a 488nm laser.

Alexa488 labelled fibrinogen (Invitrogen, Breda, Nederland) was used as the fluorescent marker and mixed with the three characterized fibrinogens at a 1:10 ratio (the sample preparation of the fibrinogens is described on section 2 of this chapter). After activation by thrombin, samples were polymerized during 60 minutes at 37°C in

Secure Seal Hybridization Chambers (Grace Biolabs, Bend, OR, USA) to avoid evaporation.

Image stacks were obtained by scanning through the z-direction on increments of 0.25µm through the sample. The analysis of the images was performed with ImageJ and the pore size is calculated from binarized images with Matlab. Pores size were determined using Lang *et al.* method [3].

4.2.3 Electron microscopy

Electron microscopy, was created by Ruska and Knoll in the 1930's. It uses a beam of electrons to create an image of the studied sample. Instead of glass lenses, electron beams are controlled by a solenoid through which one can pass a current, thereby inducting an electromagnetic field. Electron microscopes are capable of much higher magnifications and have a greater resolving power than light microscopes. This allows observing much smaller objects in finer detail. The resolving power of an electron microscopy is directly related to the wavelength of the irradiation used to form an image since reducing wavelength increases resolution.

There are two types of electron microscopes:

Transmission Electron Microscopies (TEM) are the original form of electron microscopy. It involves a high voltage electron beam emitted by a cathode and formed by magnetic lenses. The emitted electron beam is transmitted only through very thin (and so semi-transparent for electrons) specimens, carrying information about the structure of the sample. Two dimensional, black and white images with a resolution close to the nanometre are produced.

Scanning Electron Microscopies (SEM) can be used to image much more massif samples. SEM produces images by detecting secondary electrons which are emitted from the surface due to excitation by the primary electron beam. The electron beam is scanned across the surface of the sample in a raster pattern, with detectors building up an image by mapping the detected signals with beam position.

Electron microscopes are very expensive to buy and maintain. They require extremely stable high voltage supplies and stable currents to each electromagnetic lens. Continuously-pumped high vacuum systems are needed to visualize the samples, as the

molecules that make up air would scatter the electrons. Also, to avoid the scatter of the electrons by the water present on the samples, it is necessary to remove a great quantity from of their water solvent. As fibrin samples contain 70% of solvent, electron microscopy imaging is disadvantageous in terms of quantifying the real size of fibres and the protein concentration.

There are different used methods in electron microscopy, depending on the specimen, the analysis required and the type of microscope. The main techniques used in TEM and SEM microscopy are for instance, *cryo-fixation* (liquid nitrogen freezes the sample and preserves it in a snapshot of its solution state), *chemical fixation* (it preserves the sample and prevents deterioration, although it is now dead), *dehydration* (the removal of water from the samples and replacement with organic solvents like ethanol or acetone) or *staining* (the use of heavy metals to scatter imaging electrons and thus give contrast between different structures, since many biological materials are nearly transparent to the electron beam)

4.2.4 Atomic Force Microscopy

Atomic Force Microscopy, also known as AFM, was invented in 1986 by Binning *et al* .[4]. AFM microscopes use a cantilever with a very sharp tip that scans over the sample. As the tip approaches the surface, the attractive force between the surface of the sample and the tip deflects the cantilever towards the surface. A laser beam is used to detect cantilever deflections towards or away from the surface. Then, the topography of the sample is reconstituted with a computer. Figure 23 schematizes the functioning of an AFM microscope.

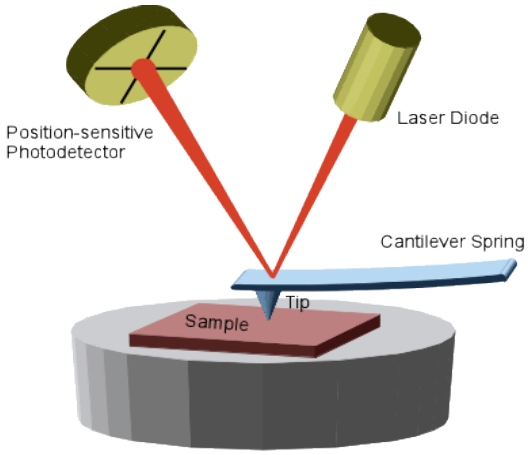

Figure 23. AFM microscopy schema

AFM microscopy can provide three-dimensional surface profiles of the probed specimens. Additionally, samples viewed by AFM do not require any special treatments that irreversibly change or damage the sample. While an electron microscope needs an expensive vacuum environment for proper operation, most atomic force microscopy modes can work in ambient air or even a liquid environment. This makes it possible to study biological macromolecules and even living organisms.

The main disadvantages of AFM microscopy are the single scan size and their very slow scanning speed, which can lead for instance to thermal drift on the samples.

5 Scattering methods

Scattering methods, such as light scattering or small angle x-ray scattering, are powerful tools used to investigate the structure and the dynamics of soft systems, such as fibrin.

Here, we present a short overview of the scattering theory and describe several scattering techniques like dynamic light scattering, small angle x-ray scattering or small angle neutron scattering. Finally, we present the corresponding experimental setups used in this thesis.

5.1 Light scattering

Light scattering methods are used to describe the structure and dynamics of soft condensed matter like suspensions of colloidal particles, solutions of polymers, or biological systems. Space scales from tens of nanometres to tens of microns and time scales from a fraction of microsecond to several hours can be probed. Light scattering allows obtaining information from a significant number of scattering objects (contrary to microscopy techniques) and perform statistical studies of the systems.

Scattering methods can be divided in two groups: static and dynamic light scattering. In static light scattering (SLS), the structure of a sample is probed by measuring the time-averaged scattered intensity as a function of the scattering angle. Dynamic light scattering (DLS) gives information of the sample dynamics which is extracted from the temporal fluctuations of the scattered intensity.

5.1.1 Light scattering theory

Scattering is a physical process where radiation, like visible light, is deviated in multiple directions due to interactions between non-uniformities in the medium. The scattered radiation is collected by a detector and analysed to get information on the sample structure or dynamics.

We consider an incident beam consisting of a plane, monochromatic and linearly polarized electromagnetic wave. The electric part of the electromagnetic wave (the magnetic part can generally be neglected) is described as it follows:

$$E_I(\boldsymbol{r}, t) = E_0^{\,i(\boldsymbol{k_I}\cdot\boldsymbol{r}-\omega t)} \quad (1)$$

where E_0 is the electric field amplitude, $\boldsymbol{k_I}$ is the wave propagation vector (that has a modulus $k_I = \frac{2\pi}{\lambda}$, where λ is the wavelength in the medium through which the wave is propagating), ω is the wave angular frequency, $\boldsymbol{r}$ is the position vector relative to an arbitrary origin O and t is the time at which the wave is evaluated.

Here we assume several facts for the case where the incident wave is scattered by a disordered system of N particles. First, the intensity of the light scattered by the solvent is negligible compared to the scattered by particles. Second, the Born approximation (or Rayleight-Gans-Debye approximation) is valid. This means that the particles are small compared to the wavelength of the incident radiation and their refractive index is close to that of the solvent. Also, the diffusion process is "quasi-elastic", which means that the energy transfer from the photons to the sample is negligible and the amplitude k_S of the propagation vector of the scattered light is equal to k_I ($k_I = k_S = 2\pi/\lambda$).

As it is illustrated in Figure 24, the difference between the propagation vectors of the scattered light and the incident beam gives as result the scattering vector $\boldsymbol{q = k_S - k_I}$. For "quasi-elastic" processes, the scattering vector amplitude is written as:

$$q = \frac{4\pi}{\lambda}\sin\theta$$

where 2θ is the scattering angle.

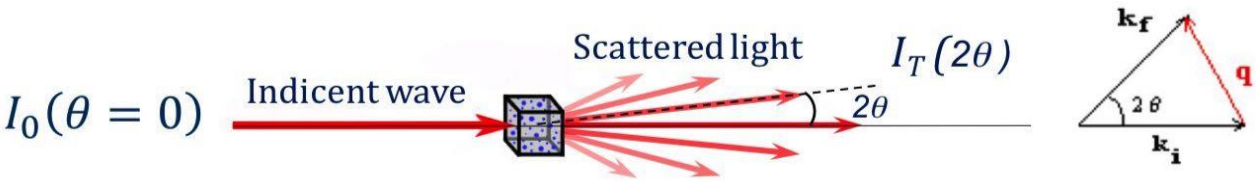

Figure 24. Scattering experiment schema

The modulus of the scattering vector has dimension of the inverse of length. It is represented by q^{-1}, which physically corresponds to the length-scale observed on the system. For large scattering angles 2θ, q^{-1} will be smaller than the particles correlation length (e.g. the particle size in non-interacting colloids) resulting in substantial interference, on the contrary at small angles the opposite situation will occur and the scattering intensity will reach a plateau.

The total electric field obtained in a scattering experiment on a detector positioned at a distance $R \to \infty$ is the sum of the electrical fields scattered by each particle. The quantity that is measured in a light scattering experiment is the average intensity of the scattered light that is proportional to the square of the scattered electric field. This is expressed as:

$$\langle I(\boldsymbol{q},t)\rangle = \langle |E_S(\boldsymbol{q},t)|^2\rangle \propto \sum_{i=1}^{N}\sum_{j=1}^{N}\langle b_i(\boldsymbol{q})b_j^*(q)exp\left[-i\boldsymbol{q}\cdot\left(r_i - r_j\right)\right]\rangle \qquad (2)$$

where $\langle \dots \rangle$ is the average on all the configurations, r_j denotes the position of the j-th particle with respect to O, $b_j(\boldsymbol{q})$ is the scattering amplitude for the particle j and $b_j^*(q)$ is its complex conjugate.

This results in an interference pattern, which on a screen located in the far field, shows bright and dark spots randomly distributed. The bright spots are named "coherence areas" or "speckles".

This theoretical development is inspired from Elise Tamborini thesis work [5].

5.2 Static light scattering

Static Light Scattering (SLS) measures the radiation scattered by the sample as a function of the direction of propagation $\boldsymbol{q}$. In the case of monodisperse particles, where all the terms $b_i(\boldsymbol{q})$ are equal and we can define $b_i(\boldsymbol{q}) = b(\boldsymbol{q})$**,** the intensity equation can be written as:

$$\langle I(\boldsymbol{q},t)\rangle = Nb(0)^2 P(\boldsymbol{q})S(\boldsymbol{q}) \tag{3}$$

where $P(\boldsymbol{q})$ is the form factor and is related to the shape and size of an individual particle and it is defined by:

$$P(\boldsymbol{q}) = \left[\frac{|b(\boldsymbol{q})|}{b(0)}\right]^2 \tag{4}$$

The quantity $S(\boldsymbol{q})$ defines the static structure factor and is given by:

$$S(\boldsymbol{q}) = \frac{1}{N}\sum_{i=1}^{N}\sum_{j=1}^{N}\langle exp\left[-i\boldsymbol{q}\cdot\left(r_i - r_j\right)\right]\rangle \tag{5}$$

$$= 1 + \frac{1}{N}\sum_{i\neq j}^{N}\sum_{j=1}^{N}\langle exp\left[-i\boldsymbol{q}\cdot\left(r_i - r_j\right)\right]\rangle \tag{6}$$

The static structure factor describes the system structure providing information on the relative positions of the scatterers, and hence on their interactions.

In experiments, a measure of the structure factor can be obtained from the ratio between the intensity distribution measured for a concentrated suspension ($\langle I(\boldsymbol{q},t)\rangle = Nb(0)^2 P(\boldsymbol{q})$), and the form factor measured on a diluted suspension of the same particles.

5.3 Dynamic light scattering

5.3.1 Method

Dynamic Light Scattering (DLS) experiments measure the intensity scattered by a sample at a given angle 2θ using as a sensor a photodiode or photo multiplier tube with

a size comparable to the coherence area. The obtained signal is then transmitted to a photocorrelator that computes the normalized time-correlation function at a fixed q defined as:

$$g_2(\tau) = \frac{\langle I(t)I(t+\tau)\rangle}{\langle I(t)\rangle^2} \tag{7}$$

where $\langle \dots \rangle$ indicates an average on time, $I(t)$ is the intensity scattered at a time t and $I(t+\tau)$ is the intensity scattered at time $t+\tau$.

The intensity correlation function is the quantity that is measured in a DLS experiment. From the point of view of theory is preferable to define $g_1(\tau)$ as the normalized time-correlation function of the scattered electric field.

$$g_1(\tau) = \frac{\langle E_s(t)E_S^*(t+\tau)\rangle}{\langle I(t)\rangle} \tag{8}$$

For randomly distributed particles, the scattered electric field is the sum of a very large number of unitary random vectors, and is a Gaussian variable. Under these conditions, $g_2$and $g_1$are linked by the Siegert relation [6]

$$g_2(\tau) = 1 + \beta^2|g_1(t+\tau)|^2 \tag{9}$$

where β^2 is a constant depending on the ratio between the detector size and the speckle size ($\beta^2 = 1$ if the detector area is very small with respect to the speckle size).

The random movement of nanometric solid particles (< 1μm) in a fluid, also referred to as Brownian movement, is caused by thermal agitation. It is the collision between the molecules in the fluid and the particles in the suspension. The energy of each particle is defined as $\frac{3k_bT}{2}$, where $k_b$is the Boltzmann constant and T is the temperature of the fluid.

This random motion is modelled by the Stokes-Einstein equation that connects the diffusion coefficient D measured by dynamic light scattering to particle size. D is written as follows:

$$D = \frac{k_b T}{6\pi\eta R} \tag{10}$$

where $k_b$is the Boltzmann constant, T is the temperature of the fluid, η its viscosity and R defines the hydrodynamic radius of the particles.

The correlation function of the electric field decreases exponentially as:

$$g_1(\tau) = \exp\left(-\frac{\tau}{\tau_c}\right) \tag{11}$$

where $\tau_c = \frac{1}{2Dq^2}$, so $g_2(\tau)$ can be written as:

$$g_2(\tau) = 1 + \beta\exp(-2Dq^2\tau) \tag{12}$$

Figure 25 shows a schematic representation of the decay of the function $g_2(\tau)$.

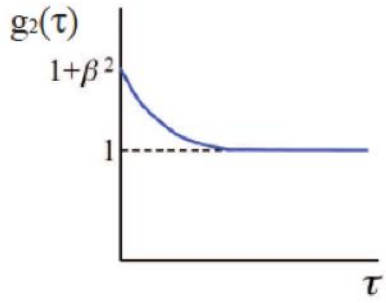

Figure 25. Schematic representation of the decay function g2(t)

5.3.2 Experimental setup

DLS measurements were performed at the Cermav laboratory (Grenoble, France) using a CGS-8FS/N069 apparatus from ALV technology (Manila, Philippines) with a 35 mW 632.8 nm laser from JDSU (Milpitas, CA, USA).

The three fibrinogens were loaded in 10 mm diameter cylindrical cells, immerged in a toluene bath and thermostated at a temperature of 25.0 ± 0.1°C. Data were collected at 90° for 120 s. Hydrodynamic radius distributions and their polydispersity index were obtained using Contin analysis.

5.4 Turbidimetry

5.4.1 Method

Turbidimetry is a technique that quantifies the attenuation of light transmitted through a sample. Light is transmitted to a spectrophotometer through an optic fibre where it is collimated, diffracted and focalized to a CCD barrier where the spectre is formed. The CCD barrier sends then an electric signal that reproduces the intensity captured by the different pixels. Turbidimetry techniques, as it is illustrated on Figure 26, obtain information from the wavelength spectre, from 500nm to 800nm in our case of study.

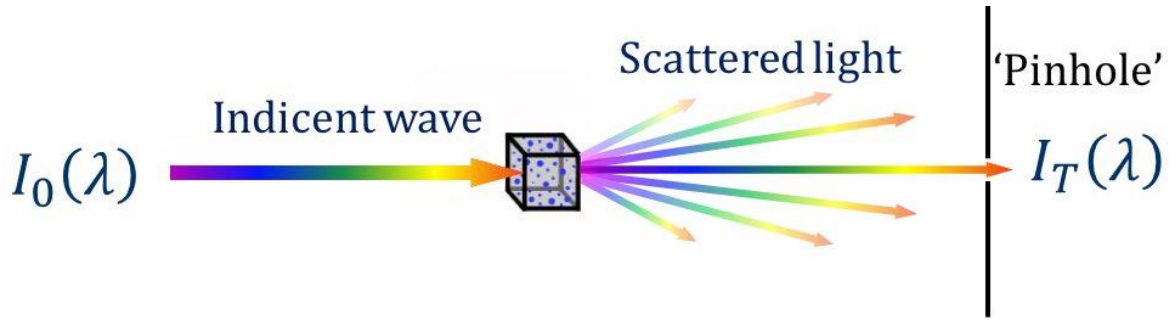

Figure 26. Scattering principle

The turbidity is the natural logarithm of the intensity transmission T, while the optical density D is its decimal logarithm:

$$T = \frac{I_T}{I_0} = \exp(\tau A) = 10^{-DA} \tag{13}$$

so that

$$\tau = D \ln(10) \tag{14}$$

where I_0 is the incident intensity, I_T is the transmitted intensity and A is the depth of the medium.

As long as multiple light scattering and the dependent scattering effects are negligible, the turbidity is related to the scattering cross section C_{scat} and number density of particles N_p by:

$$\tau = N_p C_{scat} \tag{15}$$

where

$$C_{scat} = \int_0^{2\pi} \int_0^{\pi} \frac{I_\theta(\lambda)}{I_0} r^2 \sin(\theta) d\theta d\phi \tag{16}$$

For the particular case of the turbidity of randomly oriented thin fibres Yeromonahos *et al.* [7] obtained a formula that allows the calculation of the radii of the fibres and their protein density from the turbidity of a fibrin gel. This relation can be written as:

$$\tau\lambda^5 = 2\pi^3 C n_s \frac{\mu}{N}\left(\frac{dn}{dc}\right)^2 \frac{44}{15}(\lambda^2 - \frac{92}{77}\pi^2 a^2 n_s^2) \tag{17}$$

where τ [cm^{-1}] is the turbidity of the suspension, λ [cm] is the wavelength, μ [Da/cm] is the mass-length ratio, a [cm] is the radius of the fibres, n_s is the refraction index of the solvent, n is the refraction index of the fibres and C [mg/ml] is the concentration of fibrinogen. Here, it is assumed that the fibres are cylinders of length L where $L >> \lambda$, $\lambda >>$ R_g and the *distance of observation* >> L.

The exposed relation implies that $\tau\lambda^5$ varies linearly as a function of λ^2. By plotting this relation we can obtain the average mass-to-length ratio (μ), the average number of protofibrils per fibre cross section ($Np=\mu/\mu_0$, where μ_0 = 1,44x10^{11} Da/cm represents the mass-to-length ratio of a single protofibril [8,9]) and the and the average radius (a) of fibrin fibres. The average protein mass concentration (δ) is determined from the mass-to-length ratio and the radius of the fibres as ([7]):

$$\delta = \frac{\mu}{\pi a^2} \tag{18}$$

5.4.2 Experimental setup

The experimental device used to perform turbidimetry measurements was conceived by Yeromonahos *et al.* and the creation process is described on her PhD [10]. It consists on a thermostatic structure constituted by six commercial spectrophotometers (USB650, Ocean Optics, USA) remotely controlled by a computer. The experimental setup is schematized on Figure 27.

Fibrin gels were formed in 10mm optical path length polystyrene cuvettes (Brand, Wertheim, Germany) by mixing 2/3 of the fibrinogen solution and 1/3 of the thrombin solution. The cuvettes were covered with Parafilm to prevent evaporation. The optical density spectra, going from 500nm to 800nm, was measured each 3 seconds and the temperature was set at the physiological condition of 37°C.

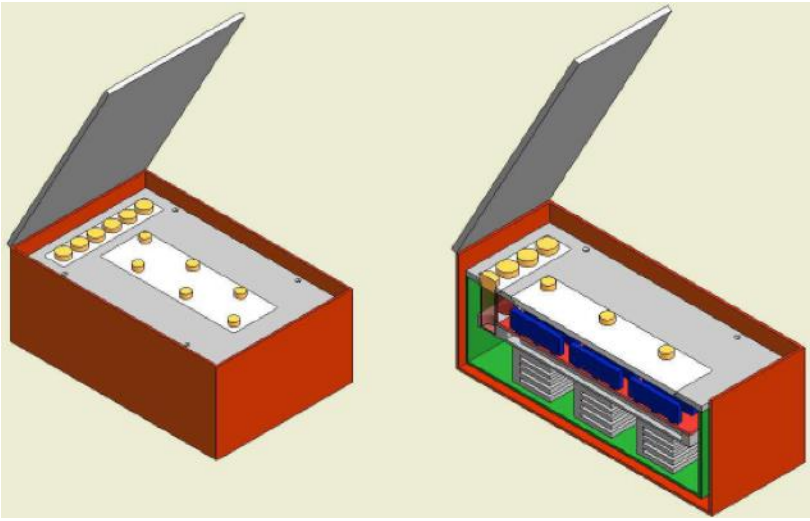

Figure 27. Different views of the spectrophotometry prototype developed by Yeromonahos et al [7]

5.5 Small angle x-ray scattering

5.5.1 Synchrotron functioning

Electrons emitted by an electron gun are first accelerated in a linear accelerator (Linac) and then transmitted to a circular accelerator (booster synchrotron) where they are accelerated to reach an energy level of 6 billion electron volts (6 GeV).

These high-energy electrons are then injected into a large storage ring (a tube of ~850m in circumference) where they circulate in a vacuum environment, for many hours, close to the speed of light. The storage ring has alternate straight and curved sections. Each curved section is formed by two large bending magnets. Those magnets force the electron beam to follow an orbit very close to a circumference. In each straight section, focusing magnets ensure that electrons remain close to their ideal orbital path. Also, each straight section hosts an undulator, a device consisting of series of alternating magnets. This forces the electron to follow an undulating, wavy, trajectory.

As electrons are deflected from their straight path when passing through the bending magnets, they emit a spray of X-rays tangentially to the plane of the electron beam. The synchrotron light produced from a bending magnet covers a wide and continuous spectrum, from microwaves to hard X-rays.

The beam provided by the accelerator is then modified on the beamline. Specialised mirrors and crystal optics are used to focus the beam and select the wavelength desired for each kind of experiment. Finally, the beamline provides a way to put a sample of material in the X-ray beam trajectory, control its position, adjust the beam and capture data.

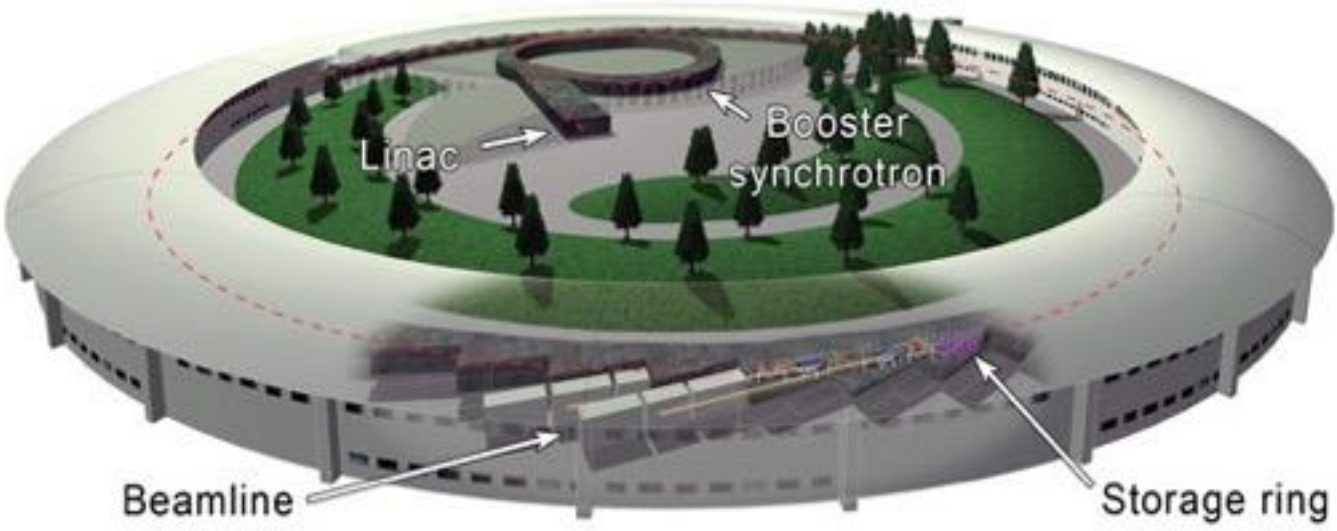

Figure 28. Synchrotron schema from ESRF

5.5.2 Method

Small Angle X-ray Scattering (SAXS) is a physical method identical, except for the used wavelength, to the previously described light scattering method (cf. section 5.1) SAXS can be applied to study the overall shape and structural transitions of biological structures since it can be used to measure the form and structure factors of the sample. Here we review some of the technical aspects of how does SAXS work.

Typical SAXS experiments profiles represent the intensity as a function of q in the range q_{min} - q_{max}, defined by the experimental setup. A measurement made at a given wavevector q_0 allows to investigate the density fluctuations in the sample for a length scale $d_0 = \frac{2\pi}{q_0}$. This is equivalent to observe the system through a $\frac{2\pi}{q_0}$ diameter "window" in real space. To study objects much smaller or larger than d_0 , another window has to be selected. The smallest or largest observations windows are given by $d_{min} = \frac{2\pi}{q_{max}}$ and $d_{max} = \frac{2\pi}{q_{min}}$ respectively. This determines the size of the smallest (and respectively

biggest) particles than can be observed with the instrument (in the particular case of the line ID02, *q*-range can go from 0.001 nm^{-1} to 50 nm^{-1}).

The *q*-range of SAXS experiments is usually divided in three domains, here explained and illustrated on Figure 29

- *High q domain:* The window is very small: there is a contrast only at the interface between the two media. This domain, named *Porod's region*, gives information about the interfaces present in the sample.
- *Intermediary zone:* The window in this domain is of the order of the "elementary bricks" in the systems. The form factor *P(q)* can be measured (size, shape and internal structure of one particle).
- *Low q domain:* The window here is very large so the structural order can be obtained. The structure factor *S(q)* can be obtained in order to calculate the interactions in the system.

To access the three different regions of *q* vectors here described, several detection distances from the sample must be combined. The further the detector is placed from the sample, the smaller the studied angles and the *q* vectors are. A detector placed at a distance of 2m can access to a region going from 0.07 to 3nm^{-1} while a distance of 30m distances from 0.15 to 1.4nm^{-1}.

The development of x-ray scattering principles is inspired on the CEA published version by the *Institut Rayonnement-Matière* of Saclay (France) [11].

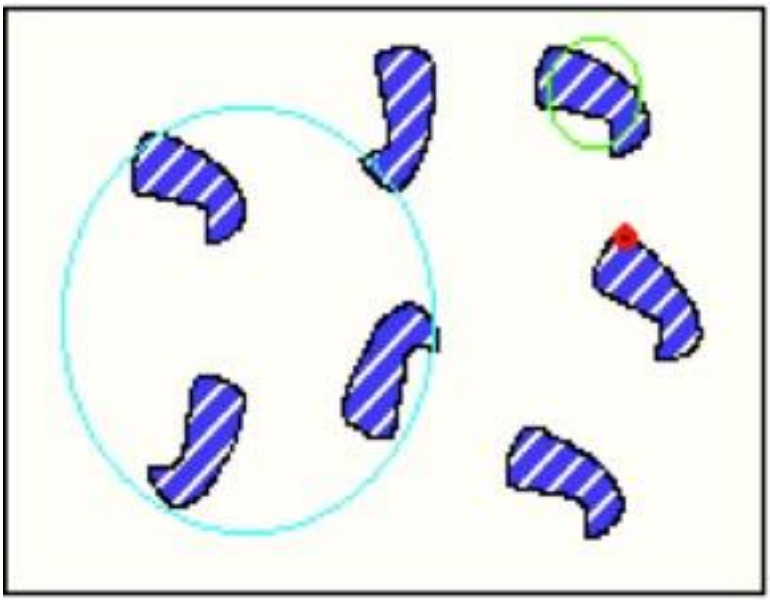

Figure 29: q-range domains of SAXS experiments. High q domain is represented in red colour, intermediary zone in green and low q domain in blue.

5.5.3 Experimental setup

We performed measurements at the ID02 line of the European Synchrotron Radiation Facility (ESRF, Grenoble, France). In order to carry out these experiments, we used the system previously developed by Yeromonahos *et al.* [10], which is a self-made thermostatic and electro-mechanic stopped flow device (Figure 30). This device meets the requirements of SAXS experiments here itemized:

- Due to the low diffusion of the protein solutions of our samples, quartz or polycarbonate cells were used.
- Previous tests have demonstrated that the mix fibrinogen-thrombin and the formation of a fibrin clot on a capillary system is not possible. The use 200µL, rectangular cells, was then prioritized.
- In order to optimize the measurements and avoid cleaning, the system requires several *semi-disposable* cells. For each measurement, single-use quartz layers (20µm thickness) were glued to the two faces of a brass structure.

- To favour the repeatability of the experiments, an automatized stopped flow system was established. This system consists of an electromagnet which activates the piston of a pipette, which in turn injects the thrombin solution that activates polymerization.

First, 180μL of buffer were injected into the cell structure described above. Then, a first X-ray scattering measurement was performed to measure the quartz layer impurities and subsequently subtract them during the analysis. Second, 20 μl of a fibrinogen solution of 1 mg/ml final concentration was injected into the cell structure. Finally, the stopped flow system was set in the experimental cabin to inject a 20μL thrombin solution ([IIa] = 0.1 IU/ml final concentration) and trigger the polymerization.

The scattering measurement was initiated from the command cabin exactly at the same time as the polymerization was activated. In order to avoid the damage of the sample caused by the electron beam a snake-like pattern (48 measuring points in an acquisition time of 0.1s/point) was programed to scan the whole surface of each sample. The sample-detector distance was set at 7m.

5.6 Small angle neutron scattering

Small Angle Neutron Scattering, also referred to as SANS, is a technique used to characterize shapes and structural transitions at a scale that goes from 1nm to 1000nm. SANS is based on the same scattering principle as SAXS method. The main difference between SAXS and SANS experiments is that samples are here illuminated with a neutron beam instead of electrons. Neutrons are elastically scattered by nuclear interaction with the nuclei or interaction with magnetic momentum of unpaired electrons.

The use of SANS techniques is commonly used on the case of biological systems due to the behaviour of hydrogen. In the case of biological samples for SANS and USANS experiments, *heavy water* solvents (D_2O) are used to obtain good and variable contrast and minimize the incoherent scattering background.

The advantage of SANS over other small angle scattering methods (such as small-angle x-ray or light scattering) is the deuteration method. This method consists in using

deuterium labelled components in the sample in order to control their contrast. which is impossible in SAXS at it measures only density fluctuations.

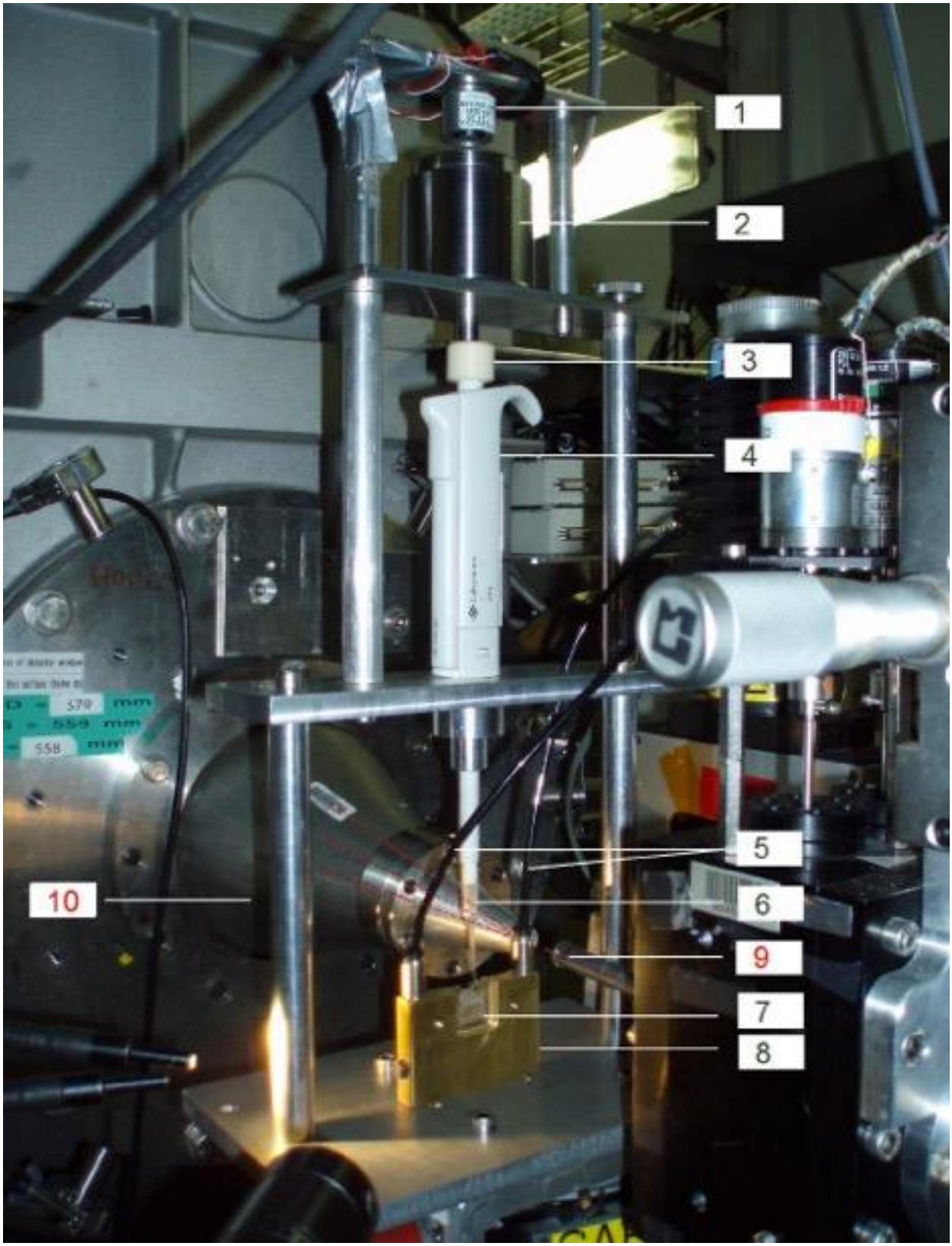

Figure 30. Stopped flow system (not in use, i.e. away from the beam path): 1- Electro-magnet; 2- Weight; 3- Pipette's push button, 4- Pipette, 5- Thermostatic circuit; 6- Thrombin's solution prior to the experiment; 7- Homemade cell, 8- Cell's holding structure, 9- X-ray beam, 10- Detector

6 Mechanical properties. Rheology

6.1 Introduction

In the beginning of the XXth century the existing theories used to describe either liquids or solids were insufficient to describe a new class of materials which properties were between these two states. A set of new theories and experimental techniques were developed in order to characterize and understand the deformation and flow properties of such materials which are now referred to as non Newtonian or complex fluids. This field of science is now known as *rheology*. In the following chapter we present the basic notions of rheology and a description of the different configurations and methods used in this study [12].

6.2 Basic notions in Rheology

The main purpose of rheology is to characterize the relation between *strain*, *strain rate* and *stress* within materials. One usually distinguishes purely non-Newtonian viscous fluids, purely elastic materials as hookean solid and viscoelastic materials which properties lay between those of purely elastic and purely viscous materials. Prior to any presentation of specific experimental setups normally used to characterize the flow properties of a complex fluid, the next section will explain the notions of velocity gradient and stress tensor, which are useful mathematical expressions to describe the deformation of materials under applied forces.

6.3 Velocity Gradient Tensor and Stress Tensor

6.3.1 Velocity Gradient, Rate of Deformation and Vorticity Tensors

Here we consider a point in a three dimensional space defined by it's Cartesian coordinates $\vec{x} \equiv (x_1, x_2, x_3)$. The velocity vector at point $\vec{x}$ is also defined here as $\vec{v}(\vec{x}) \equiv \big(v_1(x), v_2(x), v_3(x)\big)$ where v_1, v_2 and v_3 are the components of the velocity in directions parallel to the directions '1', '2' and '3' respectively. The *i, j* components of the *Velocity Gradient Tensor* $\nabla\mathbf{v}$ are given by the expression:

$$\nabla\mathbf{v}_{i,j} = \left(\frac{\partial v_j}{\partial x_i}\right)_{i,j=1,2,3} \tag{19}$$

Considering v_0 as the velocity of any given point in the flow with the origin x_0 being chosen arbitrarily, the velocity of a nearby point *x* is then given as a function of the velocity gradient by the relation:

$$\vec{v}(\vec{x}) = \vec{v}_0 + (\vec{x} - \vec{x}_0)\,\nabla\mathbf{v} \tag{20}$$

Equation (20) represents the physical significance of the velocity gradient tensor which represents the steepness of the velocity variations from point to point in any direction of a flow.

We consider a fluid element in such a flow. It is always possible to consider its deformation as a combination of a stretch and a rotation. These two components of any flow deformation correspond to the definition of the 'rate-of-deformation' tensor **D** and the vorticity tensor $\boldsymbol{\omega}$ which are respectively the symmetric and antisymmetric part of the gradient tensor given by equations (21) and (22) respectively

$$\mathbf{D} = \frac{1}{2}(\nabla\mathbf{v} + \nabla\mathbf{v}') \tag{21}$$

$$\boldsymbol{\omega} = \frac{1}{2}(\nabla\mathbf{v} - \nabla\mathbf{v}^T) \tag{22}$$

6.3.2 Stress Tensor

We define here an infinitesimal cube of material within a flow (see Figure 31). $\left(d\vec{F}_j\right)_{j=1,2,3}$ are the forces exerted by the material exterior to the cube on its face perpendicular to the j direction and $\left(d\vec{F}_{ij}\right)_{i,j=1,2,3}$ their components on the *i* direction. The stress vector $\vec{T}(M,\vec{n})$ at the center *M* of a surface *ds* oriented by the normal vector $\vec{n}$ is defined by:

$$\overrightarrow{dF} = \vec{T}(M,\vec{n})ds \tag{23}$$

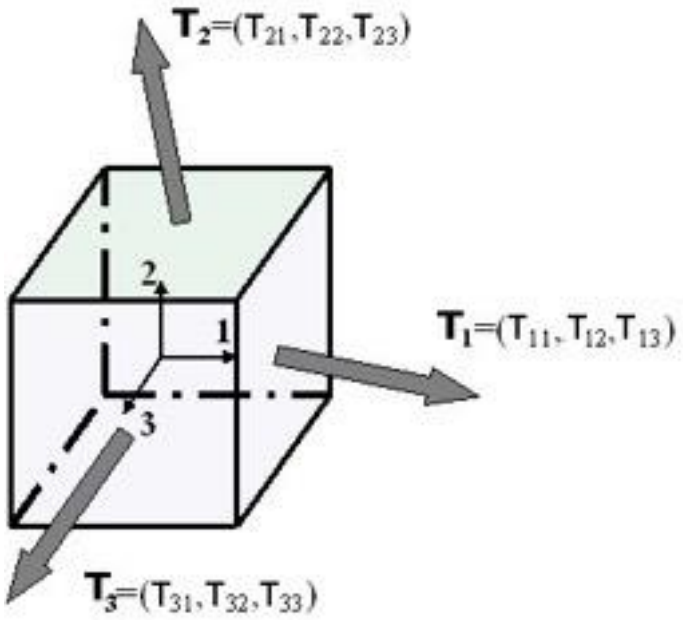

Figure 31. Definition of the state of stress in terms of forces acting on the faces of a unit cube

The state of stress tensor $\mathbf{T}(M)$ is defined then by:

$$\vec{T}(M,\vec{n}) = \mathbf{T}(M) \cdot \vec{n} \tag{24}$$

The *ij* components $T_{ij}$of the state-of-stress tensor $\mathbf{T}(M)$ are given by the expression:

$$T_{ij} = \left(\frac{d\vec{F}_{ij}}{ds}\right)_{i,j=1,2,3} \tag{25}$$

In a fluid "at rest" (under hydrostatic pressures) the state-of-stress tensor simplifies in an isotropic tensor given by the equation (26) where ***I*** stands for the unit tensor for which all diagonal points are unity while all non-diagonal components are null.

$$\mathbf{T} = -p\boldsymbol{I} \tag{26}$$

As only pressure gradients affect the flow motion of an incompressible fluid, the state of stress tensor can be decomposed as:

$$\mathbf{T} = \boldsymbol{\sigma} - p\boldsymbol{I} \tag{27}$$

Here, $\boldsymbol{\sigma}$ is the *extra* or viscous stress tensor. It accounts for the forces that affect the motion of the fluid. Often, **T** is referred to as the total stress tensor and $\boldsymbol{\sigma}$ as just the stress tensor.

The relation between **D** and $\boldsymbol{\sigma}$ constitutes what is usually referred as the *constitutive equation of a fluid*. Depending on its properties, especially degree of anisotropy, history dependence and elasticity, this constitutive equation of a given fluid can present various forms whit different degree of complexity. For Newtonian fluids, this equation (equation (28)) is linear and implies only one parameter, the shear viscosity η.

$$\boldsymbol{\sigma} = 2\eta\mathbf{D} \tag{28}$$

For some particularly complex fluids, their constitutive equation still remains to be formulated.

6.4 Shearing Flows

Shearing flows are the simplest configurations used in rheometry to characterize the flow properties of a material. Indeed, in such flows, several components of the *stress tensor* and the *rate-of-deformation tensor* become null. Different flow geometries can be used with different levels of approximation to produce a homogeneous shear state of stress and strain within a fluid. As is presented on Figure 32, to illustrate shearing flow we consider a fluid confined between two parallel plates, one fixed and the another one moving at a constant velocity, V_0.

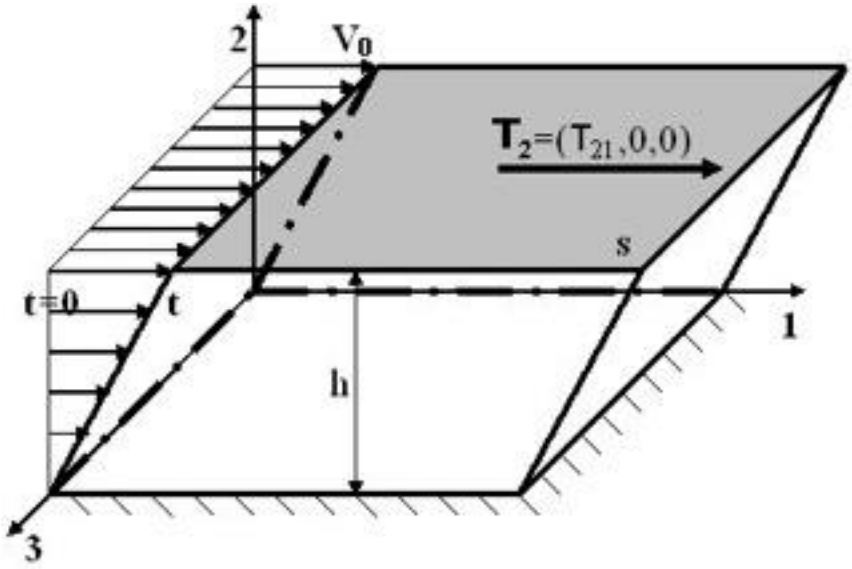

Figure 32. Deformation induced by a shearing flow

We assume that the described flow is laminar; that is, the convective terms due to inertial effects in the *Navier-Stokes equations* can be neglected. We consider as well a no-slip boundary condition at the interface plates-fluid that verifies equations (29) and (30). Here the deformation of the bulk can be considered as the sliding of thin fluid layers one over the others

$$v_1(x_2 = 0) = 0 \tag{29}$$

$$v_1(x_2 = h) = V_0 \tag{30}$$

If a two dimensional flow is considered, the only non null component of the velocity at a distance $x_2$from the fixed plate is given by the relation:

$$v_1(x_2) = \frac{V_0}{h} \cdot x_2 \tag{31}$$

Then, the *rate-of-deformation* tensor is represented by:

$$D_{12} = D_{21} = \frac{V_0}{2h} = \frac{\dot{\gamma}}{2} \tag{32}$$

From equation (32) we introduce the term $\dot{\gamma}$, also referred as the *shear rate*. The presented flow conditions give rise to a simple expression of the *stress tensor* $\boldsymbol{\sigma}$. The relative movement of each layer induces friction forces corresponding to necessary force to move the upper plate F_2. Being s the surface of the plates, the component σ_{12} of the stress tensor usually referred to as the *shear stress* is given by the following expression:

$$\sigma_{12} = \sigma_{21} = \frac{F_{21}}{\mathrm{s}} \tag{33}$$

The *shear viscosity* of a material (equation (34)) is defined as the ratio between the shear stress σ_{12} and the shear rate $\dot{\gamma}$. Considering the simplest case of Newtonian fluids, the shear viscosity is constant so that the shear stress (σ_{12}) is directly proportional to the shear rate ($\dot{\gamma}$). Moreover, the shear stress is the only non null component of the stress tensor, so that the knowledge of the shear viscosity is sufficient for a complete characterization of the shear flow behaviour of Newtonian fluids.

$$\eta = \frac{\sigma_{12}}{\dot{\gamma}} \tag{34}$$

In complex fluids the relation between the shear stress and the shear rate is more complicated. Indeed, the shear stress experienced by the sample can be dependent of the applied stress, the shearing time, the thermo-mechanical history, etc. In some cases, the shearing process can induce normal forces so that the diagonal components of the stress tensor are no more null. As a consequence, knowing the shear viscosity ay a given shear rate is not enough to characterize the material flow properties. Therefore, the shear stress to shear rate ratio presented on equation (35) is usually referred to as the *apparent shear viscosity*.

$$\eta(\dot{\gamma}, t) = \frac{\sigma_{12}(\dot{\gamma}, t)}{\dot{\gamma}} \tag{35}$$

6.5 Non-Newtonian Behaviours

As mentioned before, knowing the shear viscosity of a Newtonian fluid is sufficient to predict its behaviour in other flow configurations. In the case of the complex materials, the internal structure depends on the flow conditions and conversely.

When the ratio between the shear stress and the shear rate is not constant the fluid is referred to as *non-Newtonian*. These fluids can then have both a viscous and an elastic part, for which they are as well referred to as *viscoelastic fluids.*

These *flow-structures* interactions ultimately result in the emergence of non-linear and time-dependent terms in the constitutive equations controlling their flow properties. A range of test has been developed through the years in order to characterize this kind of materials. [12–15].

6.5.1 Normal stress in shearing flow

Some macromolecules like polymers present the properties of being able to stretch and orient themselves according to the flow field when sheared [16][17]. This usually results in the apparition of diagonal terms in the *stress tensor.* The microscopic reorganization of of the structures in a shear flow, as the one represented in Figure 32, generates macroscopic effects consisting in the emergence of a normal force, along direction 2, that tends to either push the two parallel plates apart or pull them closer depending on its sign. The stress tensor $\boldsymbol{\sigma}$ is determined to within an additive isotropic tensor so that only the first and second normal stress differences defined in equations (36) and (37) can be measured. In practice only N_1 is conveniently measured with usual apparatus [18].

$$N_1 = \sigma_{11} - \sigma_{22} \tag{36}$$

$$N_2 = \sigma_{22} - \sigma_{33} \tag{37}$$

The emergence of normal forces with a steadily sheared material is usually a good indicator of its elastic properties. Materials presenting both viscous and elastic properties are referred to as *viscoelastic fluids*. The characterization of their viscoelastic

properties usually requires the use of a dynamic approach as described in the following section.

6.5.2 Linear viscoelasticity

As mentioned above, viscoelastic fluids present intermediate properties to those of a purely viscous fluid and those of a purely elastic solid. Because of that, viscoelastic materials are characterized by two moduli: the *storage modulus* $G'(\omega)$ and the *loss modulus* $G''(\omega)$. They correspond to the ability of viscoelastic fluids either to store energy in the form of elastic energy or to dissipate it in viscous friction. These properties are controlled by the rate of reversible spontaneous rearrangement or relaxation of the microstructures within the fluid which depends on the frequency ω at which is the material is solicited. $G'(\omega)$ and $G''(\omega)$ are only defined for deformations of the sample small enough to ensure that the microscopic structures formed within the fluids are not irreversibly affected by the flow. Such deformation conditions correspond to what is defined as the *linear viscoelastic regime*. The characterization of the linear viscoelastic properties of a material can be achieved by imposing small-amplitude oscillating shear strains in the form $\gamma(t) = \gamma_0 \sin(\omega t)$ in which γ_0 is the strain amplitude of the oscillation and ω their angular frequency.

In the linear viscoelastic regime, the *shear stress* response $\sigma(t)$ to small amplitude sinusoidal strain is also sinusoidal with the same frequency and its amplitude is proportional to the amplitude of the strains γ_0 . The elastic component of the shear stress response is in phase with the strain γ while its viscous component is in phase with the rate of strain $\dot{\gamma}$. Therefore, in the viscoelastic regime σ is related to the imposed strain by equation (38)

$$\sigma(t) = \gamma_0(G'(\omega)\sin(\omega t) + G''(\omega)\cos(\omega t)) \tag{38}$$

The relaxation process of the structures within the fluid can be complex and can involve several characteristic times [17][19].

6.5.3 Nonlinear viscoelasticity

All non Newtonian materials present a nonlinear stress response to an applied shear strain. The linear response is characterized by a linear increase in shear stress with respect to the applied strain. Upon reaching some critical strain the material may weaken or harden with additional deformation. This is termed the linear viscoelastic limit.

Above the linear viscoelastic limit, the material can begin to weaken as a function of increasing strain, (strain-soften). Strain hardening, another form of nonlinear viscoelasticity, is the opposite property and is relatively common in biopolymer gels [20,21]. Gels formed from various proteins including fibrin, actin or collagen strain harden at deformations beyond their linear viscoelastic limit.

The nonlinear behaviour of materials is not fully understood yet and is an active field of research, especially for fibrin. Here we resume several methods that have been designed in order to probe the nonlinear response of soft materials to an applied shear.

In the case of *Large Amplitude Oscillatory Shear (LAOS)* procedures, a sinusoidal strain is applied and the stress response is measured. Nonlinearities in the stress can be *measured* by Fourier transforming, decomposition or Lissajous plots [22] In LAOS strain controlled experiments, a sinusoidal strain $\gamma(t)$ is applied and the oscillatory response $\sigma(t)$ is measured.

$$\begin{aligned} \gamma(t) &= \gamma_0 \sin(t) \\ \sigma(t) &= \sigma_0 \sin(\omega t + \delta) \end{aligned} \tag{39}$$

Here, γ_0 is the strain amplitude and $\delta = \frac{G'}{G''}$. G' and G'' are, respectively, the elastic and viscous components of the complex shear modulus ($G^*(\omega) = G'(\omega) + iG''(\omega)$)

It is difficult to interpret the modulus at strains above the critical strain, because the stress response is highly non-sinusoidal once the nonlinear regime is reached. G^* is obtained in LAOS experiments from the first harmonic in the response and does not consider higher order terms, which do store energy. Therefore, for strain stiffening materials such as fibrin gels, G^* underestimates the modulus in the nonlinear regime, since it corresponds to the ratio of stress over strain σ/γ, which is smaller than the local derivative, or slope, $d\sigma/d\gamma$.

Differential measurements are more accurate and can be used to probe the differential modulus $K^* = d\sigma/d\gamma$:

- *Prestress or differential technique*: A small amplitude oscillatory stress is superposed on a large steady stress. This method works mainly on materials that are predominantly elastic (already applied to fibrin gels [23]). This method presents a very poor signal to noise ratio, and biases due to inertio-elastic effects.
- *Strain ramp protocol*: The sample is subjected to a steady shear with a low strain rate $\dot{\gamma}$ [23]. This method obtains a rate-independent elastic modulus. In the case of fibrin gels, the differential moduli obtained from the strain ramp and prestress methods agree rather well, since the gels are nearly perfect elastic solids.

Nonlinear strain stiffening of materials, concretely for the case of fibrin clots, is followed by clot rupture or failure, at a critical strain. The partial or complete failure of the fibrin sample has as a consequence a decrease of the measured instantaneous and the normal force moduli.

6.6 Rheometry

Now, we review the different experimental devices used to determine the macroscopic rheological properties of materials. First, we discuss the functioning of stress and strain controlled rheometers and the relation between the technologically controlled parameters. The rheological parameters, *i.e.* the shear stress and the shear rate, are defined for the different shear cell geometries considered in our study. Finally, we describe the experimental procedures that allowed obtaining valid data.

6.6.1 Shear Rheometry

Strain and Stress Controlled Shear Rheometers

Unlike stated in their names, the physical parameters controlled or measured either by a strain or stress controlled rheometer are not the strain and the stress. Indeed, these later quantities are mesoscopic ones and therefore are not directly measurable mechanically. Strain and stress controlled rheometers are designed with a

moving shaft dragged respectively by a motor of which either the *angular velocity* or the *torque* are precisely controlled.

The angular velocity and the torque are applied to the studied sample through the use of a shear cell in which the sample is loaded. The torque (*resp*. angular displacement) induced by this mechanical solicitation is then monitored by mean of a transducer (*resp.* an angular displacement sensor) attached to the fixed part (*resp.* moving part) of the rheometer. The relations between the torque and the angular velocity and shear stress and rate, can then be determined as a function of the chosen shear cell geometry as it will be discussed.

Strain-controlled rheometers are designed with powerful motor so that they can supply the energy necessary to deform the sample in a controlled manner. On the other hand, stress-controlled rheometers are designed with motors of which the torque is precisely controlled. Here the torque-related stress applied to the tested sample and corresponding to the energy density experienced by the sample is precisely controlled.

Shear Cell Geometries: Macroscopic to Mesoscopic Relations

We have used three standard shear cell geometries in our rheological measurements. These are the *cup and bob* or *Couette* geometry, the *cone and plate* geometry and the *parallel plates* geometry. In the following paragraphs, the relations between the torque and the angular velocity and the shear stress and the shear rate are introduced. To preserve the clarity of the writing, we assume the shear flow to be Newtonian, laminar, isothermal and steady.

Cup and bob shear cells

As shown in Figure 33, in a cup and bob geometries the sample is loaded between two concentric cylinders of respective radius R_1 and R_2, one being fix and the other moving. Either if the angular velocity Ω or the torque Γ is the controlled parameter does not change the relations between these macroscopic and measurable quantities and their mesoscopic counterparts within the sample, the shear rate $\dot{\gamma}$ and the shear stress σ_{12}.

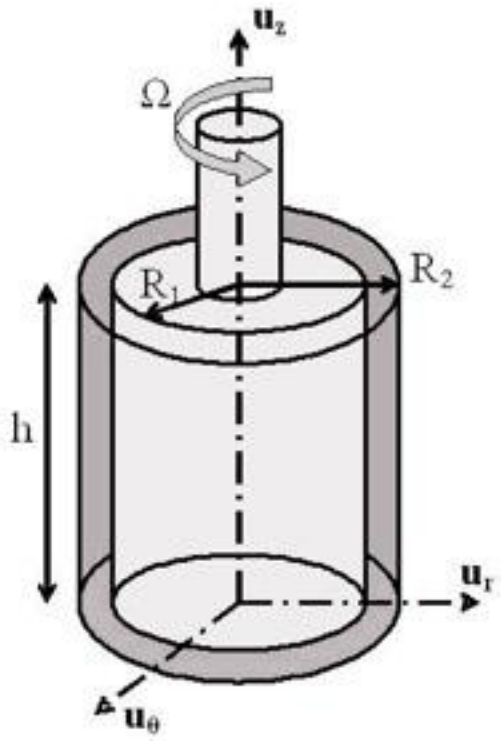

Figure 33: Cup and bob geometry

Considering that the gap separating both cylinders is small when compared to their radius of curvature ($R_2 - R_1 \ll R_1$), the values of stress and shear rate in the following are expressed as:

$$\sigma \approx \frac{\Gamma}{2\pi h R_1^2} \tag{40}$$

$$\dot{\gamma} \approx \frac{\Omega R_1}{R_2 - R_1} \tag{41}$$

Cone and plate shear cells

The second class of shear cells here described are the cone and plate geometries. As can be seen in Figure 34, the sample is now loaded between two coaxial fixtures: a truncated cone and a plate. The truncated cone is positioned so that its virtual vertex coincides with the centre of the fixed plate.

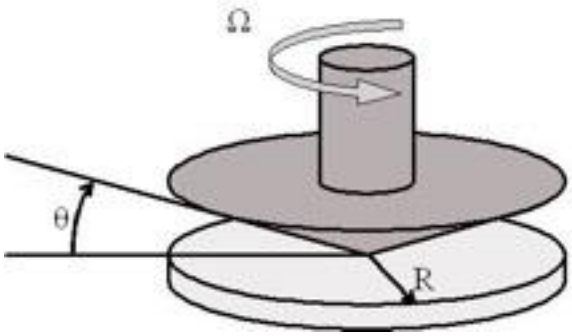

Figure 34: Cone and plate cell

For small enough values of the cone angle ($\theta \leq 4°$), the velocity profile between the cone and the plate at a given radius r can be considered as linear. Therefore, both the shear rate and the shear stress are uniform in the whole sample volume. These are simply given in equations (42) and (43) as a function of the plate radius R, the torque applied to the moving part of the rheometer Γ and the cone angle θ.

$$\dot{\gamma} = \frac{v_\theta(r)}{h(r)} = \frac{r\Omega}{r\tan\theta} = \frac{\Omega}{\tan\theta} \tag{42}$$

$$\sigma = \frac{3\Gamma}{2\pi R^3} \tag{43}$$

The cone and plate geometry ensures uniform shear stress and rate within the tested sample and also allows to measure the first normal stress difference N_1 by measuring the vertical force F_z applied on the cone by the sheared sample.

$$N_1 = \sigma_{11} - \sigma_{22} = \frac{2F_z}{2\pi R^2} \tag{44}$$

Cone and plate geometries have undeniable asset to generate uniform shear rates and shear stresses but they are not suitable to characterize the rheological properties of complex fluids with internal structures larger than the cone truncation. In that case the basic postulates on which the continuum mechanic has been developed becomes invalidated.

Parallel plates shear cells

Finally, we considered this type of shear cells in our rheological study. As is shown in Figure 35, the sample is loaded between two coaxial parallel plates which distance is constant along a radius so that neither the shear stress or the shear rate are uniform within the investigated sample. Indeed, equation (45) shows that the local shear stress increases linearly along the radius.

$$\dot{\gamma}(r) = \frac{v_\theta(r)}{h} = \frac{r\Omega}{h} \tag{45}$$

As in the case of cup and bob geometries and as is given in equation (46), only the mean value of the shear stress can be deduced from the torque Γ applied to the geometry.

$$\langle\sigma\rangle = \frac{3\Gamma}{2\pi R^3} \tag{46}$$

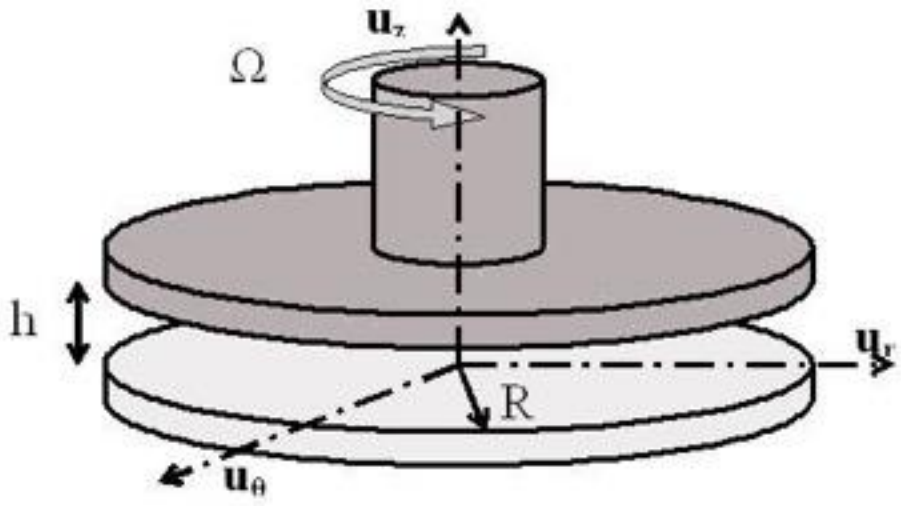

Figure 35: Parallel plates geometry

Since the contribution of the sheared sample to the torque applied to the plate is maximum at the rim of the geometry, the apparent shear viscosity measured with these shear cells is defined by:

$$\eta_{app} = \frac{\langle \sigma \rangle}{\dot{\gamma}_{r=R}} \quad (47)$$

6.7 Experimental setup

We performed rheological experiments on a stress-controlled MCR 501 rheometer (Anton Paar, Graz, Austria). The geometry chosen to perform measurements on fibrin clots was a 25mm steel plate-plate geometry. To avoid the evaporation of the fibrin gels during measurements, the edge of the samples was coated with a low viscosity mineral oil.

A mixture of 2V of the fibrinogen solution and 1V of the thrombin solution of a final volume of 500µm was directly realized on the peltier plate of the rheometer. Fibrin clots were polymerized at 37°C during 4h.

First, polymerization of fibrin gels was monitored by recording the evolution of the elastic and viscous moduli (*G', G''*) by applying low strain oscillations (γ=0.5% at f=0.5 Hz), well below the onset of strain influence on the formation of fibrin [24].After 4h, the linear viscoelasticity of the mature samples was determined in the 0.1-20Hz range.

Finally, the nonlinear rheology of the fibrin samples was probed by applying the *shear strain ramp protocol* previously introduced (section 6.5.3 of this chapter). The protocol for each cycle of either single or successive time-linear strain ramps consisted the following steps: (a) the initial deformation was set to σ = 0 Pa for 20s, (b) a constant linear shear rate of $\dot{\gamma}$= 0.005 s^{-1} was applied until reaching the required maximal shear strain, (c) the maximal shear strain was then imposed during 5 seconds (d) a constant linear shear rate of $\dot{\gamma}$= -0.005 s^{-1} was applied until reaching the relaxation of the sample (e) the deformation was set again to σ = 0 Pa during 20s before initiating the next ramp if required. This protocol is schematized in Figure 36.

For the case of successive ramps, the maximal strain was set at 12.5% for the first ramp, 25% for the second ramp and then increments of 25% were applied for each cycle until 250%. The instantaneous modulus G_{inst} (also called differential [24], tangent [25,26] or nonlinear [27,28] modulus) was calculated as $G_{inst}=d\sigma/d\gamma$.

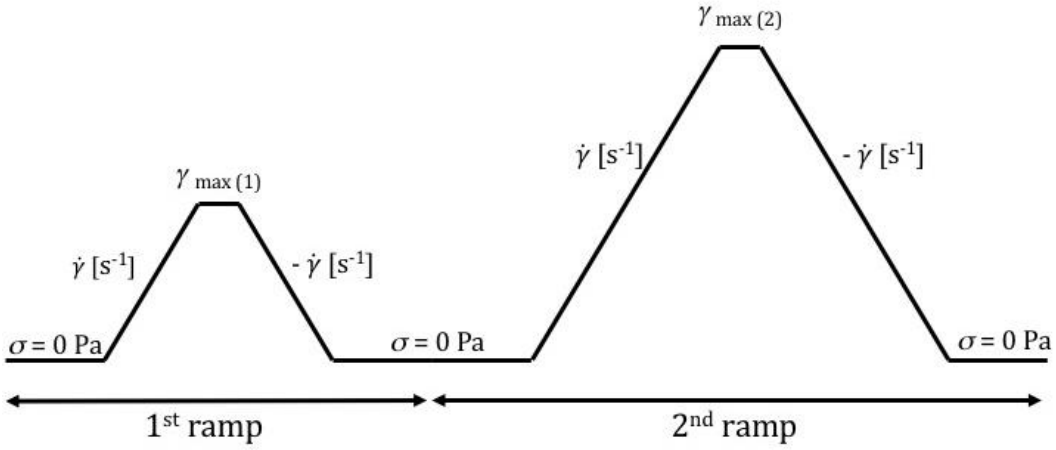

Figure 36. Protocol of time-linear shear strain ramps

References

1 Clauss A. Gerinnungsphysiologische Schnellmethode zur Bestimmung des Fibrinogens. *Acta Haematol* Karger Publishers; 1957; **17**: 237–46.

2 Hagel L. Gel-Filtration Chromatography. *Current Protocols in Molecular Biology*. Hoboken, NJ, USA: John Wiley & Sons, Inc.; 2001. p. 10.9.1-10.9.2.

3 Lang NR, Münster S, Metzner C, Krauss P, Schürmann S, Lange J, Aifantis KE, Friedrich O, Fabry B. Estimating the 3D Pore Size Distribution of Biopolymer Networks from Directionally Biased Data. *Biophys J* 2013; **105**: 1967–75.

4 Binnig G, Quate C, Gerber C. Atomic Force Microscope. *Physical Review Letters*. 1986. p. 930–3.

5 Tamborini E. Métallurgie colloïdale: structure et propriétés mécaniques d'un système colloïdal modèle comme un analogue des polycristaux atomiques. University of Montpellier II; 2012.

6 B. J. Berne and R. Pecora. Dynamic Light Scattering. ohn Wiley and Sons Ltd., Baffins Lane , 376 Seiten,; 1976.

7 Yeromonahos C, Polack B, Caton F. Nanostructure of the fibrin clot. *Biophys J* Biophysical Society; 2010; **99**: 2018–27.

8 Carr ME, Hermans J. Size and Density of Fibrin Fibers from Turbidity. *Macromolecules* 1978; **11**: 46–50.

9 Spirito M De, Arc G, Papi M, Rocco M, Ferri F, Spirito M De, Arcòvito G, Papi M, Rocco M. Small- and wide-angle elastic light scattering study of fibrin structure Small- and wide-angle elastic light scattering. 2003; : 636–41.

10 Yeromonahos C. Nanostructure des fibres de fibrine. University Joseph Fourier; 2011.

11 S. Lyonnard, O. Spalla, F. Testard, F. Né, O. Taché. Small Angle X-Rays Scattering.

12 Macosko CW. Rheology Principles, Measurements and Applications. New York Press; 1993.

13 Larson R. The structure and rheology of complex fluids. New York: Oxford University Press; 1999.

14 Ferry JD. Viscoelastic properties of polymers. John Wiley & Sons; 1980.

15 Bird RB, Armstrong RC, Hassager O. Dynamics of polymeric liquids. Volume 1: fluid mechanics. *A Wiley-Interscience Publ John Wiley Sons* 1987; .

16 Moldenaers P, Fuller G, Mewis J. Mechanical and optical rheometry of polymer liquid-crystal domain structure. *Macromolecules* American Chemical Society; 1989; **22**: 960–5.

17 Lee J-Y, Magda JJ, Hu H, Larson RG. Cone angle effects, radial pressure profile, and second normal stress difference for shear-thickening wormlike micelles. *J Rheol (N Y N Y)* The Society of Rheology; 2002; **46**: 195.

18 Auffret Y. Propriétés Macroscopiques et Microscopiques de Phases Lamellaires Lyotropes Cisaillées d'AOT/Eau/Iso-octane. University Joseph Fourier; 2008; .

19 Wunderlich I, Hoffmann H, Rehage H. Flow birefringence and rheological measurements on shear induced micellar structures. *Rheol Acta* Steinkopff-Verlag; 1987; **26**: 532–42.

20 Kang H, Wen Q, Janmey PA, Tang JX, Conti E, MacKintosh FC. Nonlinear Elasticity of Stiff Filament Networks: Strain Stiffening, Negative Normal Stress, and Filament Alignment in Fibrin Gels. *J Phys Chem B* American Chemical Society; 2009; **113**: 3799–805.

21 Storm C, Pastore JJ, MacKintosh FC, Lubensky TC, Janmey PA. Nonlinear elasticity in biological gels. *Nature* Nature Publishing Group; 2005; **435**: 191–4.

22 Piechocka IK. Biopolymers: from Structural Hierarchy to Nonlinear Rheology. University of Amsterdam; 2011.

23 Broedersz CP, Kasza KE, Jawerth LM, Münster S, Weitz D a., MacKintosh FC. Measurement of nonlinear rheology of cross-linked biopolymer gels. *Soft Matter* 2010; **6**: 4120.

24 Münster S, Jawerth LM, Fabry B, Weitz DA. Structure and mechanics of fibrin clots formed under mechanical perturbation. *J Thromb Haemost* 2013; **11**: 557–60.

25 Piechocka IK, Bacabac RG, Potters M, Mackintosh FC, Koenderink GH. Structural hierarchy governs fibrin gel mechanics. *Biophys J* Biophysical Society; 2010; **98**: 2281–9.

26 Piechocka IK, Jansen KA, Broedersz CP, Kurniawan NA, MacKintosh FC, Koenderink GH. Multi-scale strain-stiffening of semiflexible bundle networks. *Soft Matter* Royal Society of Chemistry; 2016; **12**: 2145–56.

27 Weigandt KM, Pozzo DC, Porcar L. Structure of high density fibrin networks probed with neutron scattering and rheology. *Soft Matter* 2009; **5**: 4321.

28 Weigandt KM, Porcar L, Pozzo DC. In situ neutron scattering study of structural transitions in fibrin networks under shear deformation. *Soft Matter* 2011; **7**: 9992.

Chapter 3

Fibrinogen polydispersity controls fibrin multiscale structure

Xabel GARCÍA[1], Landry SEYVE[2], Zéra TELLIER[3], Guillaume CHEVREUX[3], Nicolas BIHOREAU[3], Benoît POLACK[2], and François CATON[1]

[1]Laboratoire Rhéologie et Procédés, CNRS UMR 5520, Université Grenoble Alpes

[2]Laboratoire TIMC-IMAG TheREx, CNRS UMR 5525, University Grenoble Alpes, and Department of Hematology, University Hospital Grenoble Alpes

[3] Laboratoire Français du Fractionnement et des Biotechnologies

This chapter describes the multiscale structures of purified fibrin clots obtained from mono- and polydisperse fibrinogens. First, we present a characterization of the physic chemistry of those fibrinogens. Second, the nano- and microstructures of the fibrins are investigated. Finally, we present the work performed in order to determine the nanostructure of fibrin fibres in plasma, which allows a better understanding of the mechanisms involved on the coagulation process close to in vivo.

1 Introduction

The formation of fibrin clots is an essential process in blood coagulation. Fibrin forms a protein scaffold that enables the organism to close off damaged blood vessels. Fibrin is formed from fibrinogen after activation by thrombin which cleaves fibrinopeptides A and B, thereby exposing the A- and B-knobs and yielding fibrin monomers. Those monomers aggregate first in half-staggered linear protofibrils which subsequently aggregate laterally to form fibrin fibers.

Fibrinogen is a plasma 340-kDa centrosymetric protein. Its structure is constituted by three aligned domains. The central part of the molecule (E-region) is slightly smaller (c.a. 5nm of diameter) while the exterior regions (D-regions) present a 6nm diameter to form a structure about 45nm in length.

Some aspects of fibrin polymerization, in particular lateral aggregation, remain little known. However, it is known that various genetic and environmental factors influence not only the fibrin structure and function but they can also be related with thrombotic disease (1). Many clinical studies have associated the fibrin properties with thrombosis (2, 3).

Among the many factors influencing fibrin structure (ionic strength, pH, concentrations … (4-6)), Huang *et al.* (7) showed that the polydispersity of fibrinogen seems to play a major role. Indeed, fibrinogens purified using standard methods show a high polydispersity. Using gel filtration chromatography, they were able to reduce considerably the polydispersity index of the fibrinogen up to “monodisperse” quality. Strikingly, the monodisperse gel filtrated fibrinogen exhibited turbidity almost twice higher than the one of the original polydisperse fibrinogen. This *a priori* surprizing result was confirmed independently by another group (8). However, this might originate from a different content in γ and γ' content possibly induced by gel filtration. Indeed, the fibrin formed from γ' showed significantly different turbidities (9).

The same comparison was performed on a DLS plate-reader (10) showing differences both in kinetics as well as in the apparent size of the polymerizing objects. Importantly, all those results (7, 10) were obtained at very low fibrinogen concentrations (~0.4 mg/ml).

These results raise three main questions. First, what are the respective multiscale structures of fibrin clots obtained from mono- or poly-disperse preparations? Second, are these differences strictly related to polydispersity or are they more related to differences in fibrinogen species? Finally, are those differences still observed at physiological fibrinogen concentrations?

To answer those questions, we used three commercial fibrinogen preparations, one being size-filtered at 35nm (as described in the Summary of Product Characteristics). We first characterized the physicochemistry of those fibrinogens. The nano- and micro-scale structure of the different fibrins were then investigated in detail.

2 Materials and Methods

2.1 Materials

Human thrombin was purchased from Cryopep (Montpellier, France) as a 12 μL solution containing 298,9 IU. The solution was diluted to 200 IU/ml in a MES buffer (20mM MES, 50mM NaCl, pH 6.5) aliquoted and kept frozen at -80°C.

Three fibrinogens were used. Clottafact (Laboratoire Français du Fractionnement et des Biotechnologies, Les Ulis, France), Fib1 (Enzyme Research Laboratories, Swansea, UK) and Riastap (CSL Behring, Paris, France). Fibrinogens were reconstituted using manufacturers' guidelines and dialyzed twice overnight against HEPES buffer (140 mM NaCl, 20 mM HEPES, 5 mM $CaCl_2$, pH 7.4), aliquoted and kept frozen at -80ºC. The concentrations of fibrinogens were determined on the START'4 coagulometer (Diagnostica Stago, Asnières, France).

Dithiothreitol (DTT), iodoacetamide (IAM), urea, phosphate buffered saline (PBS), ammonium carbonate, and HEPES were purchased from Sigma-Aldrich Chemical (St. Louis, MO, USA). Acetonitrile (MeCN) was HPLC reagent grade and purchased from JT Baker (Philipsburg, NJ, USA). Trifluoroacetic acid (TFA) was from Merck Biosciences (Darmstadt, Germany). All the aqueous solutions were prepared using ultra-pure water (18.2 MΩ-cm resistivity at 25°C, total organic carbon (TOC) < 5 ppb).

2.2 Sample preparation

Fibrinogens were thawed at 37°C for 5 minutes and equilibrated at room temperature for another 5 minutes before use. Thrombin was thawed at 37°C for 1 minute, diluted in HEPES buffer and immediately used.

Fibrin clots were formed by incubating fibrinogen (0.5, 1 and 3 mg/ml) with 0.1 IU/ml thrombin (final concentration).

2.3 Size exclusion chromatography

The molecular distribution of the different fibrinogens was analysed using a Superdex 200 HR 10/30 column on a NGC liquid chromatography system (Bio-Rad, Marnes-la-coquette, France), using 20mM HEPES buffer (pH 7.4) containing 130mM NaCl. One hundred microliters of fibrinogen (10 g/l) were applied. The column was developed at a 0.5 ml/min flow rate. Elution profiles were monitored at λ=280nm.

2.4 Dynamic light scattering

Dynamic light scattering measurements were performed using a CGS-8FS/N069 apparatus from ALV Technology (Manila, Philippines) with a 35 mW, 632.8nm laser from JDSU (Milpitas, CA, USA). Fibrinogens (1mg/ml) were loaded in 10 mm diameter cylindrical cells, immerged in a toluene bath at 25.0 ± 0.1 °C. Data were collected at 90° for 120 s. Hydrodynamic radii distributions were determined using Contin analysis.

2.5 Reverse phase chromatography coupled to mass spectrometry

Fibrinogen (100 µg) was vacuum-dried and dissolved in 35 µL of a 8 M urea and 0.4 mM ammonium carbonate solution pH 8.0. Reduction was done by adding 10 µL of a 40 mM DTT solution in water and incubating the resulting mixture for 20 min at 50°C. After cooling at room temperature, 10 µL of a 80 mM IAM solution in water were added and the solution was incubated at room temperature for 20 min in the dark. RP-HPLC was performed using an ACQUITY UPLC system (Waters, Milford, MA, USA). An amount of 20 µg of sample was injected on a Pursuit 3 diphenyl reverse phase column (150x2.0 mm, 3 µm) equilibrated at 70°C and operated at a flow rate of 200 µL/min (Agilent, Santa Clara, CA, USA). An aqueous solution containing 0.1% TFA and MeCN containing 0.1 % TFA were respectively used as buffer A and buffer B; proteins were eluted by using an increasing gradient of buffer B. After separation, fibrinogen reduced and

alkylated chains were detected by UV at 280 nm and MS analysis was achieved by interfacing the UV detector output to a SYNAPT G2-S HDMS mass spectrometer (Waters, Milford, MA, USA) scanning from *m/z* 500 to 2000.

2.6 Small angle X-ray Scattering

Small Angle X-ray Scattering (SAXS) experiments were performed at the ID02 line at the European Synchrotron Radiation Facility (ESRF, Grenoble, France). The samples were placed in a home-made cell with 20µm mica windows. The sample-to-detector distance was set to 7m and the acquisition time was set to 0.1 s. We verified that no radiation-induced damage occurred.

2.7 Spectrophotometry

Fibrin gels were formed in 10mm optical path length polystyrene cuvettes (Brand, Wertheim, Germany) by mixing 2/3 of the fibrinogen solution and 1/3 of the thrombin solution. The cuvettes were covered with Parafilm to prevent evaporation. Optical density spectra (500nm to 800nm) were measured after 90 minutes at 37 ± 0.3 °C.

Optical density data were analysed using Yeromonahos's (6) model which assumes that fibrin can be modelled as a network of slim and randomly oriented fibers. We determine the mass-to-length ratio and the average diameter of fibers from the optical density *D,* given according to: $D\lambda^5 = A\mu(\lambda^2 - Ba^2)$ where λ is the wavelength, μ is the average mass-to-length ratio, and a is the average radius of fibrin fibers.

The constants A and B are respectively: $A= (44/15)\ C_F\ \pi^3\ n_s\ (dn/dc)^2\ (1/\ (\ln(10)\ N_A)$ and $B= (92/77)\ \pi^2 n_s^2$. The model parameters are C_F the fibrinogen concentration, n_s the refractive index of the solvent, the Avogadro's number N_A and dn/dc = 0.17594 cm^3/g the specific refractive index increment of fibrinogen. By plotting $D\lambda\text{^}5$ against $\lambda\text{^}2$ we obtained the average mass-to-length ratio (μ), the average number of protofibrils per fiber cross section ($Np=\mu/\mu_0$, where μ_0 = 1,44x10^{11} Da/cm represents the mass-to-length ratio of a single protofibril (11, 12)) and the and the average radius (a) of fibrin fibers.

Note that the turbidity definition in Yeromonahos et al. (6) is incorrect, as well as the constants given in Kurniawan *et al.* (13) and Piechocka *et al.* (14) (*Cf.* Yeromonahos PhD dissertation for details (15)).

Each data point represents the mean and standard deviation calculated from three individual experiments.

2.8 Confocal Microscopy

Microscopic images of fibrin networks were obtained using Alexa488 fluorescent fibrinogen (Invitrogen, Breda, Netherland) mixed with the unlabelled fibrinogens at a 1:10 ratio. Samples were polymerized using 0.1 IU/ml of thrombin and varying fibrinogens concentrations (0.5, 1, 3 and 6 mg/ml) during 60 minutes at 37ºC in Secure Seal Hybridization Chambers (Grace Biolabs, Bend, OR, USA). Fibrin networks were visualized using a TCS SP8 confocal microscope (Leica, Wetzlar, Germany) with 40x/1.3 NA and 63x/1,40 NA objectives.

Fibrin clot images contrast and brightness were adjusted using ImageJ (http://rsbweb.nih.gov/ij/).

3 Results and discussion.

3.1 Fibrinogens composition and size distribution.

3.1.1 Dynamic Light Scattering

To characterize the different fibrinogens, DLS was used to obtain their hydrodynamic radii distribution (Figure 37, A). Clottafact shows a narrow peak at 11nm, a size is close to the one of fibrinogen monomers (7, 16). Conversely, Fib1 and Riastap fibrinogens show much broader peaks with maxima at respectively 22 and 23nm.

Therefore, while Clottafact is close to be monodisperse (cumulant polydispersity index=1.1), the other two fibrinogens are clearly mixtures of higher molecular weight species, including probably fibrinogen aggregates (17).

3.1.2 Size exclusion chromatography

Then, we performed a chromatographic analysis of the three fibrinogens (Figure 37.B). All samples show a main peak corresponding to fibrinogen monomers. Riastap and Fib1 present, in addition, a higher molecular weight peak that may correspond either to aggregates or high molecular weight fibrinogens. In addition, Riastap has a distinct low molecular weight peak, corresponding to albumin as stated in the datasheet of the product.

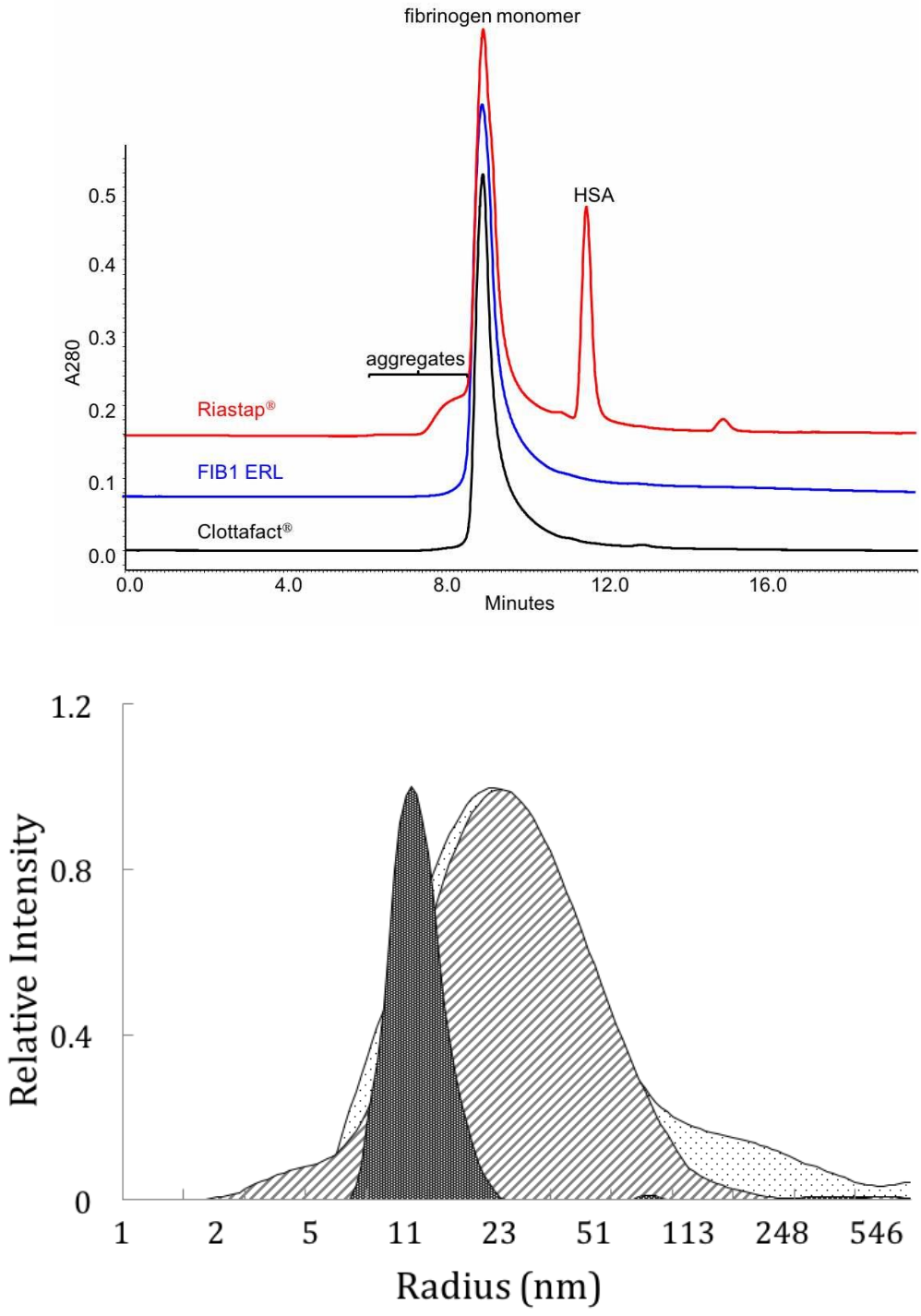

Figure 37. (Up) Size exclusion chromatography (Down) Dynamic Light Scattering results where: Black dots on white background represent Fib1; Striped lines represent Riastap; White dots on black background represent Clottafact

3.1.3 Reverse phase chromatography coupled to mass spectrometry

The three fibrinogens were further analyzed by RPLC after reduction and separation of the α, β, and γ chains. Mass spectrometry was used to determine the chain compositions of each peak (Table 1). As illustrated on Figure 38, the chains content of the different fibrinogens are very similar. The only minor difference was that Clottafact and Fib1 present more intact α–chains than Riastap. In addition, Clottafact and Fib1 have an almost identical composition in co-purified proteins (Figure 39).

The central result of these physic-chemical analyses is the major difference in polydispersity of the different fibrinogens.

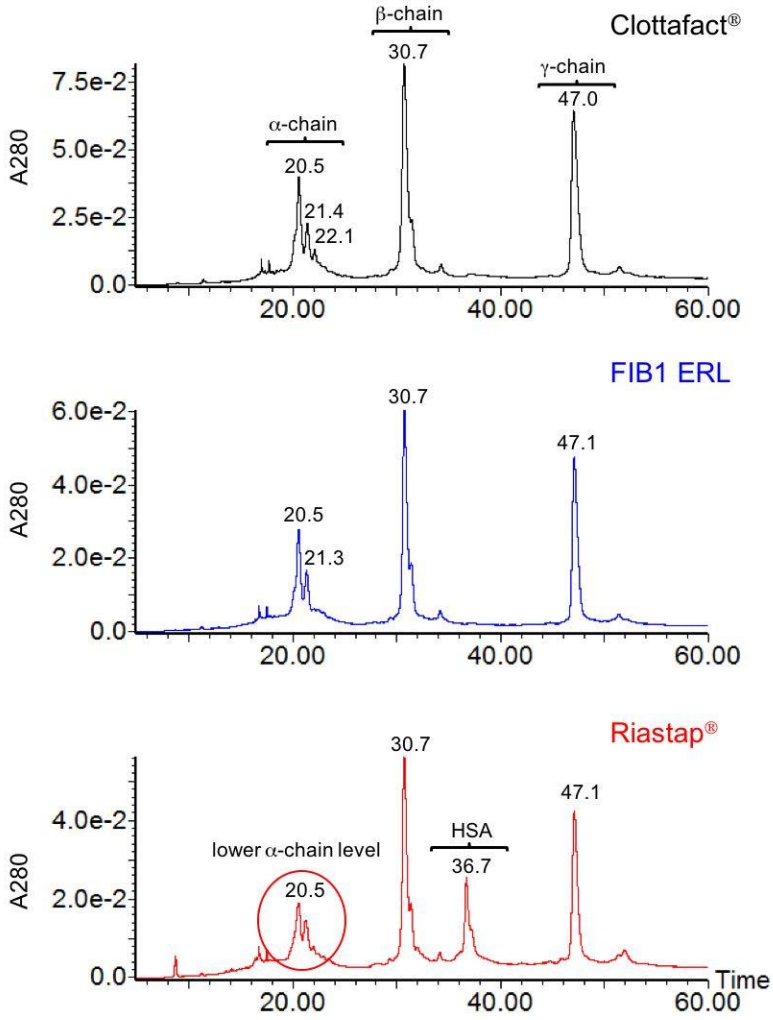

Figure 38. Reverse phase chromatography coupled to mass spectrometry results for Clottafact, Fib1 and Riastap fibrinogens

Time (min.)	Compound	Exp. mass (Da)	Theo. mass (Da)
20.5	α-chain [Ala_1-Val_{610}] left shoulder: oxidized α-chain	66590±2 66605±1	66589 66605
21.4	Cleaved α-chain [Ala_1-Ala_{585}]	63948±2	63947
22,1	Cleaved α-chain [Ala_1-Lys_{556}]	60704±2	60702
30.7	β-chain [Gln_1-Gln_{461}] + pyroGlu (Gln_1) + A_2S_1 (Asn_{364}) right shoulder: loss of Gln_{461}	54841±1 54715±1	54840 54712
47.0	γ-chain [Tyr_1-Val_{411}] + A_2S_1 (Asn_{52})	48954±1	48953

Table 1. Mass spectrometry identification of the different fibrinogen chains peaks.

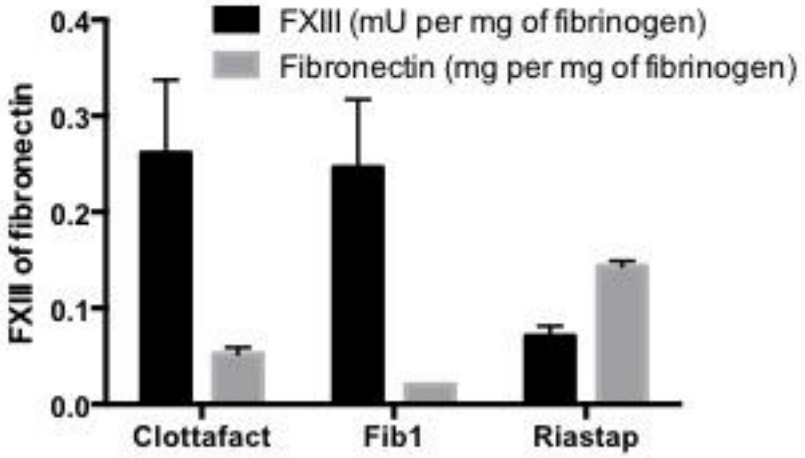

Figure 39. Relative content in fibronectin and blood coagulation factor XIII (FXIII) of the different fibrinogens. The main co-purified proteins of fibrinogen preparations were assayed by an ELISA method. Contents are given in mUnit of FXIII per 1 mg of fibrinogen or in mg of fibronectin per 1 mg of fibrinogen.

3.2 Fibrin's ultrastructure

The question is now whether or not the polydispersity difference has an impact on fibrin multiscale structure. Indeed, it could influence simultaneously the molecular, fiber and network organizations.

3.2.1 Fibrin fibres longitudinal structure.

We used Small Angle X-Ray Scattering to determine the molecular organization inside fibrin fibers. Figure 40 upper panel shows X-ray intensity spectra obtained on mature fibrin clots. The general shape of the scattering curves is similar to those obtained by Yeromonahos et al. (6) and Missori et al. (18). Spectra from each fibrin gel showed a main peak at a *q*-vector ~ 0.3 nm^{-1} corresponding to the usual 22.5nm periodicity of half-staggered fibrin monomers. However, significant differences are observed around this peak, *i.e.* between 0.2 and 0.5 nm^{-1}.

To isolate those differences, we adapted Missori *et al*. (18) method to our data: first the scattering curves were fitted with an order 3 polynomial. This polynomial was then subtracted to the scattering data, yielding the curves shown in the lower panel of figure 4. The data were fitted to two Gaussian distributions (18), one for the main

~22.5nm peak (continuous line) and the other Gaussian for the broad peak (dashed line).

It is obvious in the lower panel of Figure 40 that Clottafact exhibits a much higher amplitude and narrower main peak than the other two fibrinogens. It also shows a well-defined secondary broad peak observed neither for Fib1 nor Riastap. These contributions are modelled as Gaussian distributions.

Clottafact presents a sharp peak at q_1 = 0.284 nm^{-1} with a full-width-at-half-maximum (FWHM) of 0.019 nm^{-1} and a second, broader peak at q_2 = 0.327 nm^{-1} with an FWHM of 0.190 nm^{-1}. The first sharp peak can be assigned to a Bragg diffraction from a repeat distance of $d_1=2\pi/q_1=22.3nm$. Its FWHM gives a persistence length of 2µm of this longitudinal feature indicating that the fibers are straight over this length. The second, broader peak corresponds to a repeat distance of $d_2=2\pi/q_2=19.1nm$ which correspond accurately to the lateral dimension of the unit cell of the fibrinogen crystal described theoretically by Yang et al. (19) and experimentally by Freyssinet et al. (20). Furthermore, the FWHM of this broad peak gives a persistence length of 60nm, *i.e.* close to the diameter of the fibers.

Riastap and Fib1 present a small main peak at 0.285 nm^{-1} *i.e.* a longitudinal repeat of 22.1nm with a FWHM of ~0.01nm^{-1} giving a persistence length of ~0.6µm. This shows that fibers from clots made with Riastap and Fib1 are curvier that Clottafact's. The lateral structure was too weak to be analyzed.

This indicates that the molecular organization of fibrin fibers made from monodisperse Clottafact's is close to crystalline. The fibrin fibers made from the two polydisperse fibrinogens are much less organized longitudinally and laterally.

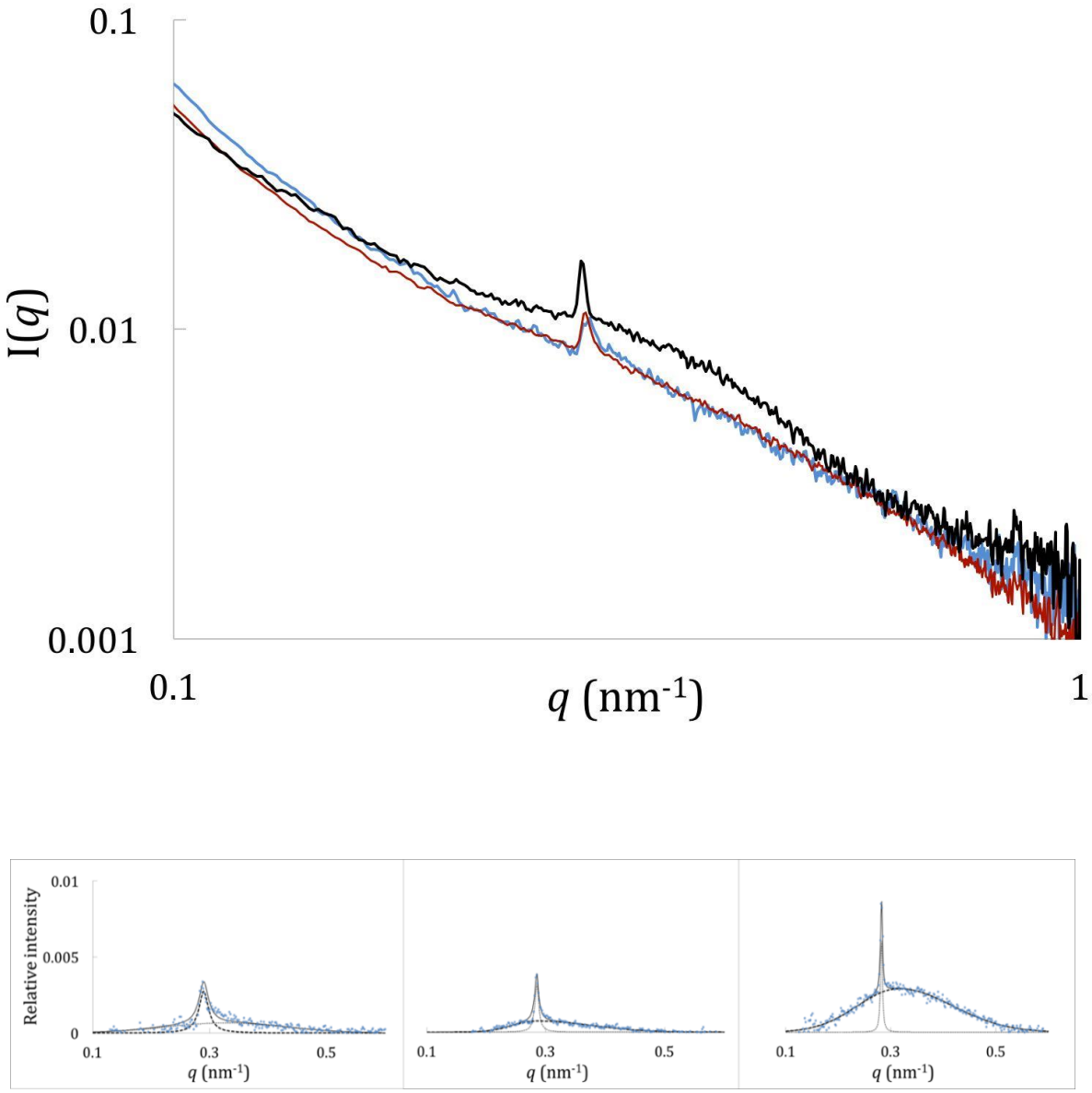

Figure 40. Small angle X-ray scattering curves for fibrin clots. SAXS was performed as described in material and methods. Upper panel: Intensity as a function of q vector. Lower panel: Relative intensity was determined according to the method of Missori et al. (18). Clots were formed using 1 mg/ml of each of the three fibrinogens coagulated using 0.1 IU/ml of thrombin.

3.2.2 Fibres lateral structure.

SAXS experiments were realized for a single experimental condition for each fibrinogen preparation (*i.e.* [Fg]=1 mg/ml; IIa=0.1 IU/ml). Therefore, we performed spectrophotometry measurements to extend the investigation for other experimental conditions as resumed in the materials and methods section.

We used our light scattering method (6) to investigate the packing of protofibrils inside the fibers. Figure 41 upper panel shows that clots from Fib1 and Riastap (polydisperse fibrinogens) have a similar number of protofibrils per fiber (*ca.* 60) while clots from Clottafact show a number of protofibrils which is four times larger (*ca.* 250). Our method also determines the average radius of the fibers (Figure 41, lower panel) that are slightly larger for Clottafact clots and increases slightly with fibrinogens concentration.

From those measurements, the protein density within the fibers can be deduced (6). Figure 5 middle panel shows that the protein density inside Clottafact fibrin fibers is much higher than for the other two fibrins. The protein density of Clottafact fibrin fibers is actually very close to that of the crystalline structure proposed by Yang and Doolittle (19), in perfect agreement with the SAXS measurements presented above.

Therefore, both SAXS and spectrophotometry results indicate that Clottafact fibrin fibers are longitudinally as well as radially close to crystalline, whereas the fibers from Fib1 and Riastap fibrinogens are considerably less organized.

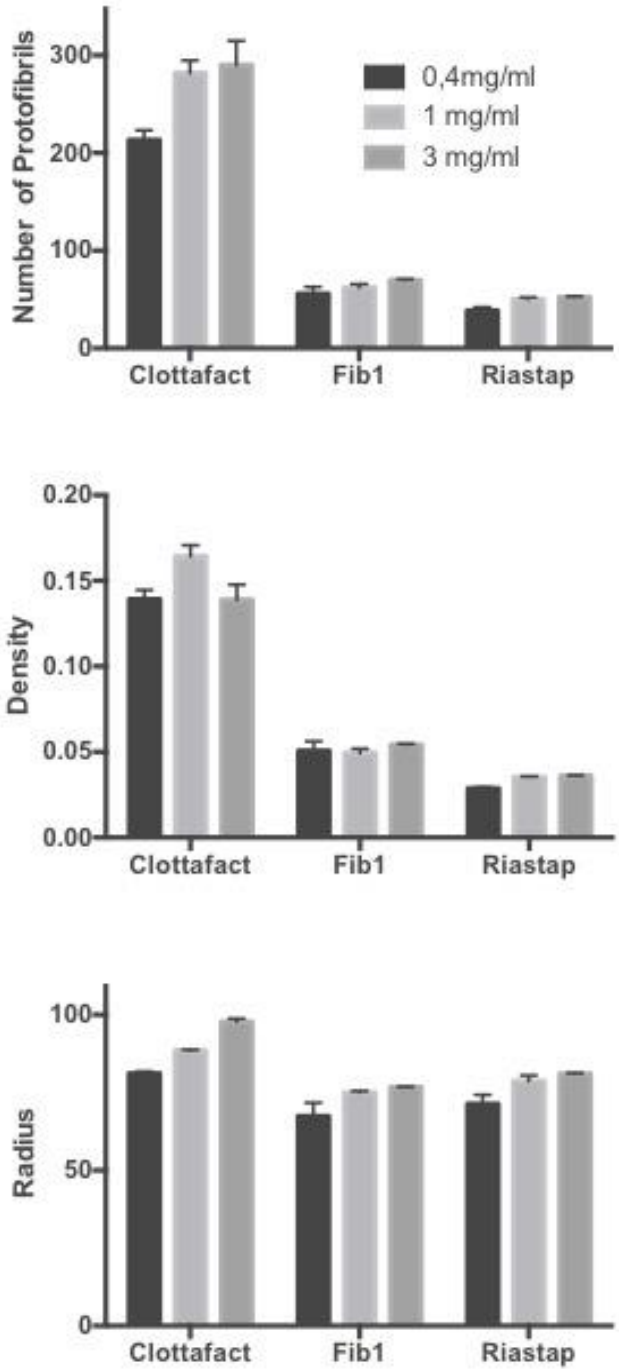

Figure 41. Fibrinography analysis of the three fibrinogens. A. Final number of protofibrils. B. Radius of fibrils. C. Protein density in the fibrils. Fibrinography was performed according to (6). Clots were formed using 0.4, 1, and 3 mg/ml of each of the three fibrinogens coagulated using 0.1 IU/ml of thrombin

3.2.3 Fibrin microstructure: Confocal microscopy

Finally, to check whether the polydispersity differences could also impact the microstructure, we investigated the network organization of fibrin clots at the micron scale. Confocal images presented in Figure 42 show the fibrin final structure obtained from the three different fibrinogens (1 mg/ml). The networks are homogeneous both in the imaging plane and also in depth (data not shown).

Strikingly, major differences in the fibers geometry are found. Indeed, Clottafact fibrin shows highly visible straight fibers, while Fib1 and Riastap produce networks with much less visible, snake-like fibers. The much higher visibility of Clottafact's fibers is probably due to the fact that they move sufficiently slowly with respect to the acquisition time, suggesting a large rigidity. Conversely, the Riastap and Fib1 fibers midpoints are almost invisible, suggesting large movements during the pixel acquisition time and therefore a smaller rigidity. The observed straightness of Clottafact fibers is in agreement with the very large persistence length obtained in the SAXS measurements while Fib1 and Riastap fibers snake-like characteristic is also in agreement with the SAXS much lower persistence length.

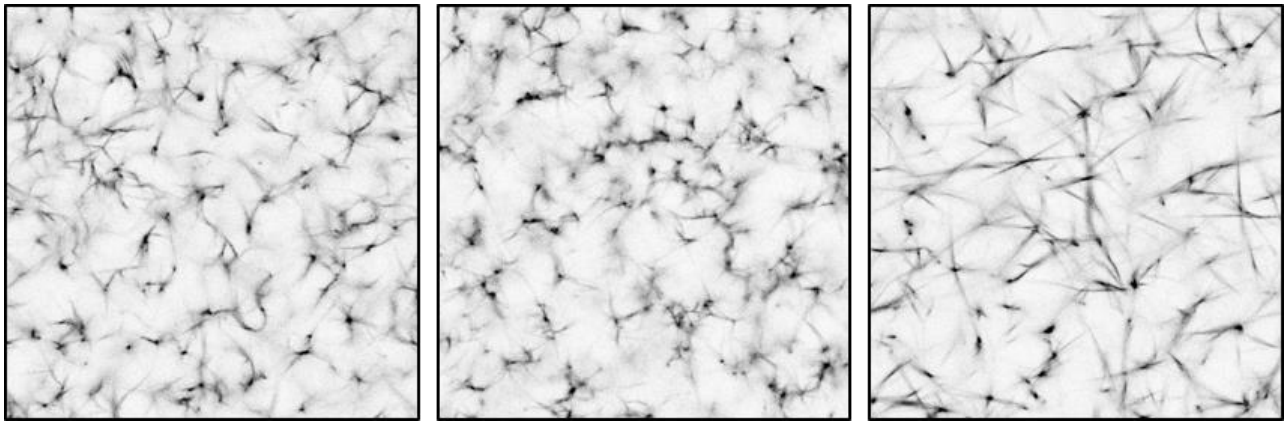

Figure 42: Confocal microscopy analysis of the three fibrinogens. Analysis was performed as described in material and methods. Clots were formed using 1 mg/ml of each of the three fibrinogens coagulated using 0.1 IU/ml of thrombin. Frames are 50 µm wide.

4 Conclusions

We have shown on one hand that Fib1 and Clottafact fibrinogens have a similar composition in co-purified proteins as well as in α-chain profiles, while Riastap showed

a large α-chain degradation pattern. On the other hand, the Clottafact's nano-filtration process conferred a quasi monodisperse profile by removing high molecular weight species. Conversely, it appears that both Fib1 and Riastap possess relatively high molecular weight species.

Both X-ray scattering and spectrophotometry demonstrated that Clottafact's fibres are almost crystalline, while Fib1 and Riastap fibres are much less organized. This structure difference was confirmed at the microscale since Clottafact's fibres exhibited much higher straightness and rigidity.

Therefore, the polydispersity index of fibrinogen controls the fibrin fibre's packing and hence the geometry and rigidity of the fibres.

This opens outstanding questions regarding the influence of polydispersity on the polymerization of fibrin, as well the mechanical properties of fibrin clots formed from monodisperse fibrinogen. It could be of paramount interest for tissue engineering on fibrin scaffolds.

5 Nanostructure of fibrin in plasma systems

5.1 Introduction

Plasma is a component of blood that makes about 55% the total blood volume. It is present in the form of a yellow liquid that holds the blood cells in suspension in what is referred to as "whole blood". Essentially, plasma is the extracellular matrix of blood cells such as red and white cells and contains the coagulation factors, which is in opposition to the serum. In physiological systems, clot formation results from an enzymatic cascade where the coagulation factors activate themselves mutually and simultaneously as introduced on Chapter 1 (*cf.* Fig. 2, Chapter 1). *In vivo,* the exposure of blood to the subendothelial space initiates two processes: activation of platelets and the exposure of tissue factor (TF). The exposure of the TF in presence of platelet phospholipids (PP) and Calcium (Ca^{2+}) is the trigger of coagulation.

The determination of the nanostructure of fibrin fibres in plasma systems allows a better understanding of the mechanisms involved on the coagulation process close to *in vivo.* In this thesis, we used the turbidity method, *i.e.* fibrinography, previously developed by Yeromonahos *et al.* [5, 6] to determinate of the nanostructure of fibrin clots either in purified or in plasma samples.

The results from Chapter 3 provided information about the role of the nature of fibrinogen on the structural properties of fibrin clots in purified systems. However, due to the complexity of the coagulation process that occurs *in vivo,* it is interesting to determine whether or not the influence of the polydispersity profiles of these three different fibrinogens (Fib1, Riastap and Clottafact) on the structure of fibrin is still significant in the quasi-physiological conditions of plasmatic systems.

Here, we have applied our method for the determination of the structure of fibrin to plasmatic systems from a normal pool of Platelet-Poor Plasma (PPP) supplemented with the three investigated fibrinogens.

5.2 Materials and Methods

The three fibrinogens (Fib1, Riastap and Clottafact) were prepared as explained in section 2.2 of this chapter. The normal pool of PPP was thawed for 5 minutes and equilibrated at room temperature for 5 minutes. PPP at an initial fibrinogen

concentration of 3 mg/ml, was supplemented with the fibrinogens by mixing either 2V of PPP with 2V of the fibrinogens or 4V of PPP with 1V of fibrinogen. Control samples were also realized.

Plasmas were mixed with Tissular Factor and phospholipids, to final concentrations of 2pM and 4 μM respectively. Plasmas were incubated at 37°C during 10 minutes. Coagulation was initiated by the addition of $CaCl_2$, to a final concentration of 16.7 mM. Clots were formed at 37°C during 90 minutes and the determination of the structure was realized by turbidity methods, as described previously.

5.3 Results and conclusions

Figure 43 illustrates the results obtained for the PPP supplemented with each tested fibrinogen. For the case of the monodisperse fibrinogen (Clottafact) we observe that, in terms of number of protofibrils, there is no significant difference between the control sample and any of the two supplementations tested (*i.e.* 20% and 50% of Clottafact added to the PPP). Conversely, for the case of polydisperse fibrinogens (Fib1 and Riastap) we observe that the final number of protofibrils is significantly lower than the one obtained for the control sample. Moreover, the increase on the addition of polydisperse fibrinogens results on a lower final number of protofibrils.

We conclude that in plasmatic systems, which imply a more complicated coagulation process than in purified systems, the differences observed between mono- and polydisperse fibrinogens are still present. Moreover, monodisperse fibrinogens do not influence the final structure of plasma clots while polydisperse fibrinogens impact significantly the nanostructure of fibrin clots in plasma.

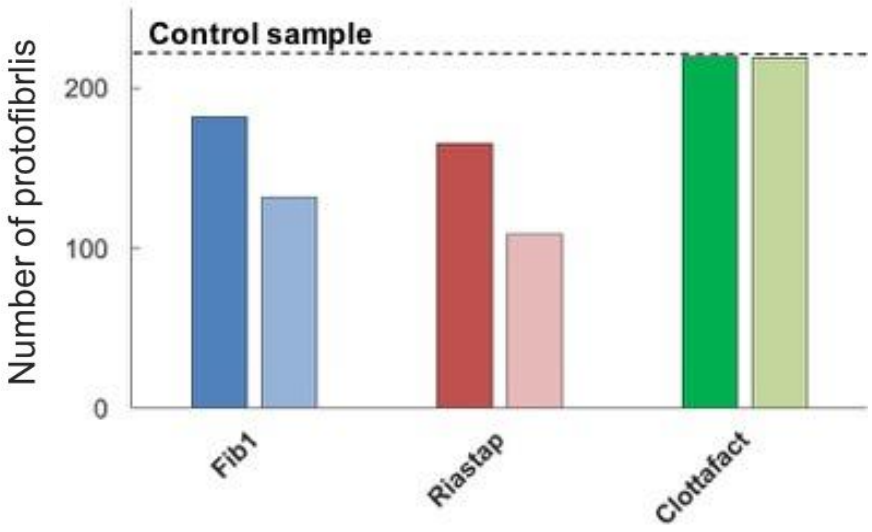

Figure 43. Number of protofibrils for the three fibrinogens in purified system. Dark colours represent the supplementation of 20% and light colours 50%

The dashed line represents the Np obtained for the control sample

References

1. Undas, A., and R. A. Ariens. 2011. Fibrin clot structure and function: a role in the pathophysiology of arterial and venous thromboembolic diseases. Arteriosclerosis, Thrombosis, and Vascular Biology 31:e88-99.

2. Ariens, R. A. 2013. Fibrin(ogen) and thrombotic disease. J Thromb Haemost 11 Suppl 1:294-305.

3. Longstaff, C., and K. Kolev. 2015. Basic mechanisms and regulation of fibrinolysis. J Thromb Haemost 13 Suppl 1:S98-105.

4. Ferry, J. D. 1952. The Mechanism of Polymerization of Fibrinogen. Proc Natl Acad Sci U S A 38:566-569.

5. Yeromonahos, C., R. Marlu, B. Polack, and F. Caton. 2012. Antithrombin-independent effects of heparins on fibrin clot nanostructure. Arterioscler Thromb Vasc Biol 32:1320-1324.

6. Yeromonahos, C., B. Polack, and F. Caton. 2010. Nanostructure of the Fibrin Clot. Biophys J 99:2018-2027.

7. Huang, L., and S. T. Lord. 2013. The isolation of fibrinogen monomer dramatically influences fibrin polymerization. Thromb Res 131:e258-263.

8. Piechocka, I. K., K. A. Jansen, C. P. Broedersz, N. A. Kurniawan, F. C. MacKintosh, and G. H. Koenderink. 2016. Multi-scale strain-stiffening of semiflexible bundle networks. Soft Matter 12:2145-2156.

9. Domingues, M. M., F. L. Macrae, C. Duval, H. R. McPherson, K. I. Bridge, R. A. Ajjan, V. C. Ridger, S. D. Connell, H. Philippou, and R. A. S. Ariëns. 2015. Thrombin and fibrinogen γ′ impact clot structure by marked effects on intrafibrillar structure and protofibril packing. Blood 127:487-495.

10. Huang, L., J. P. Hsiao, C. Powierza, R. M. Taylor, 2nd, and S. T. Lord. 2014. Does topology drive fiber polymerization? Biochemistry 53:7824-7834.

11. Carr, M. E., Jr., and J. Hermans. 1978. Size and density of fibrin fibers from turbidity. Macromolecules 11:46-50.

12. Spirito, M. D., G. Arcòvito, M. Papi, M. Rocco, and F. Ferri. 2003. Small- and wide-angle elastic light scattering study of fibrin structure. J. Appl. Cryst. 36:636-641.

13. Kurniawan, N. A., J. Grimbergen, J. Koopman, and G. H. Koenderink. 2014. Factor XIII stiffens fibrin clots by causing fiber compaction. J Thromb Haemost 12:1687-1696.

14. Piechocka, I. K., R. G. Bacabac, M. Potters, F. C. MacKintosh, and G. H. Koenderink. 2010. Structural Hierarchy Governs Fibrin Gel Mechanics. Biophys J 98:2281-2289.

15. Yeromonahos, C. 2011. Nanostructure des fibres de fibrine. Université Joseph Fourier.

16. Cardinali, B., A. Profumo, A. Aprile, O. Byron, G. Morris, S. E. Harding, W. F. Stafford, and M. Rocco. 2010. Hydrodynamic and mass spectrometry analysis of nearly-intact human fibrinogen, chicken fibrinogen, and of a substantially monodisperse human fibrinogen fragment X. Arch Biochem Biophys 493:157-168.

17. Brookes, E., J. Perez, B. Cardinali, A. Profumo, P. Vachette, and M. Rocco. 2013. Fibrinogen species as resolved by HPLC-SAXS data processing within the () enhanced SAS module. Journal of applied crystallography 46:1823-1833.

18. Missori, M., M. Papi, G. Maulucci, G. Arcovito, G. Boumis, A. Bellelli, G. Amiconi, and M. De Spirito. 2010. Cl− and F− anions regulate the architecture of protofibrils in fibrin gel. European Biophysics Journal 39:1001-1006.

19. Yang, Z., I. Mochalkin, and R. F. Doolittle. 2000. A model of fibrin formation based on crystal structures of fibrinogen and fibrin fragments complexed with synthetic peptides. Proc Natl Acad Sci U S A 97:14156-14161.

20. Freyssinet, J. M., J. Torbet, G. Hudry-Clergeon, and G. Maret. 1983. Fibrinogen and Fibrin Structure and Fibrin Formation Measured by Using Magnetic Orientation. Proc Natl Acad Sci U S A 80:1616-1620.

Chapter 4

Fibrin nanostructure controls the mechanical properties of fibrin clots

Xabel GARCÍA[1], Landry SEYVE[2], Benoît POLACK[2], and François CATON[1]

[1]Laboratoire Rhéologie et Procédés, CNRS UMR 5520, Université Grenoble Alpes

[2]Laboratoire TIMC-IMAG TheREx, CNRS UMR 5525, University Grenoble Alpes, and Department of Hematology, University Hospital Grenoble Alpes

This chapter describes the mechanical properties of different fibrin clots obtained from mono and polydisperse fibrinogens, as in the previous chapter. First we characterize the linear rheological properties of fibrin clots for a wide range of fibrinogen concentrations. Second, we determine the nonlinear rheological and fatigue properties, as well as the rupture scenarios of the fibrin clots.

1 Introduction

The formation of fibrin clots is an essential process in blood coagulation. Fibrin forms a protein scaffold that closes off damaged blood vessels. Fibrin is formed from fibrinogen after activation by thrombin, yielding fibrin monomers. Those monomers aggregate first in half-staggered linear protofibrils which subsequently aggregate laterally to form fibrin fibres.

Several studies have set a relation between cardiovascular pathologies and abnormal structures of fibrin clots [1]. The mechanical properties of such clots should also determine if they could break free and migrate in the circulation, forming an embolus. This embolus may obstruct an artery in the lung (pulmonary embolism), the heart (myocardial infarction), in the brain (stroke) or a peripheral artery in a limb (distal embolism). Therefore, the determination and modelling of the relation between the structure of fibrin clots and their rheological properties is of great importance.

The fibrin clot is a viscoelastic material [2–4] which shows high extensibility, strain stiffening, as well as negative normal stresses [5] depending on fibrinogen concentration [6–9]. Several models have linked the nonlinear mechanical properties to the structure of fibrin, proposing either that the strain stiffening of fibrin clots is caused by the conformational entropy in individual stretched fibres or by non affine network rearrangements [10,11]. Experimental results do not yet discriminate between these models, both aspects could be responsible of the nonlinear behaviour [7,8,12].

To study this structure-mechanics relationship, the structure of the fibrin clot must be modified. Up to date, the only work using this approach modified the ionic strength [9]. Alternatively, it has been shown that, under physiological conditions [13–15], fibrin polymerized from monodisperse fibrinogen results on significantly different structures compared to polydisperse fibrinogen solutions.

In a previous work [15] we have determined that the polydispersity profiles of different commercial fibrinogens control the multiscale structure of fibrin clots. Using SAXS and fibrinography [16,17] techniques, we have determined [15] that monodisperse fibrinogens lead to the formation of close to crystalline, straight, fibrin fibres. On the other hand, polydisperse fibrinogens lead to amorphous, less organized,

fibrin fibres. Therefore, the polydispersity profile of fibrinogen controls fibrin fibres internal packing and hence their geometry. This result opens the question of the influence of the multiscale structure of fibrin on the linear, nonlinear and fatigue mechanical properties, as well as on the rupture scenarios of fibrin clots.

To this aim, we used the same fibrinogen preparations as in our previous work [15], which present either crystalline or porous fibrin fibres. We first characterized the linear rheological properties of the different fibrin clots for a wide range of fibrinogen concentrations. Then, we determined the nonlinear rheological properties, fatigue properties and rupture scenarios of fibrin clots.

2 Materials and Methods

2.1 Sample preparation

The same three commercial fibrinogens, with the same lot numbers, were used as in our previous study [15]: Clottafact fibrinogen (35nm nano-filtered, Laboratoire Français du Fractionnement et des Biotechnologies, Les Ulis, France), Fib1 (Enzyme Research Laboratories, Swansea, UK) and Riastap (CSL Behring, Paris, France). The fibrinogens were reconstituted using the manufacturer's guidelines and then dialyzed twice overnight against HEPES buffer (140 mM NaCl, 20 mM HEPES, 5 mM $CaCl_2$, pH 7.4), aliquoted and kept frozen at -80ºC. The concentrations of fibrinogens were determined on a START'4 coagulometer with STA-LiquidFib (Diagnostica Stago, Asnières, France) and by using Clauss method [18].

Human thrombin was purchased from Cryopep (Montpellier, France) as a 12 μL solution containing 298,9 IU. The solution was diluted to 200 IU/ml in a MES buffer (20mM MES, 50mM NaCl, pH 6.5) aliquoted and kept frozen at -80°C.

Fibrinogens were thawed at 37°C for 5 minutes and equilibrated at room temperature for another 5 minutes before use. Thrombin was thawed at 37°C for 1 minute, diluted in HEPES buffer and immediately used.

Fibrin clots were formed by incubating fibrinogen (0.4, 1, 3 and 6 mg/ml) with 0.1 IU/ml thrombin.

2.2 Fibrinogen composition and size distribution

The initial fibrinogen preparations were characterized by size exclusion chromatography, mass spectrometry analysis and dynamic light scattering as previously described [15].

2.3 Fibrins ultrastructure characterization

The multi-scale structure of the fibrin gels was determined using Small Angle X-ray Scattering, multi wavelength spectrophotometry and confocal microscopy. For details, see [15].

2.4 Rheology

Rheology was performed on a stress-controlled rheometer MCR 501 (Anton Paar, Graz, Austria) with a 25mm steel plate-plate geometry. To prevent evaporation, the edge of the samples was coated with a low viscosity mineral oil. Fibrin clots were polymerized at 37°C during 4h. Polymerization was monitored by recording the evolution of the elastic and viscous moduli (γ=0.5% at f=0.5 Hz), well below the onset of strain influence on the formation of fibrin [19]. The linear viscoelasticity of the mature samples was then determined in the 0.1-20Hz range.

The non-linear rheology was probed to the samples by applying either a single time-linear shear strain ramp up to the apparent rupture of the clot, or successive time-linear shear strain ramps.

The protocol for each cycle of either single or successive time-linear strain ramps consisted the following steps: (a) the initial deformation was set to σ = 0 Pa for 20s, (b) a constant linear shear rate of $\dot{\gamma}$= 0.005 s^{-1} was applied until reaching the required maximal shear strain, (c) the maximal shear strain was then imposed during 5 seconds (d) a constant linear shear rate of $\dot{\gamma}$= -0.005 s^{-1} was applied until reaching the relaxation of the sample (e) the deformation was set again to σ = 0 Pa during 20s before initiating the next ramp if required. This protocol is schematized in Figure 44.

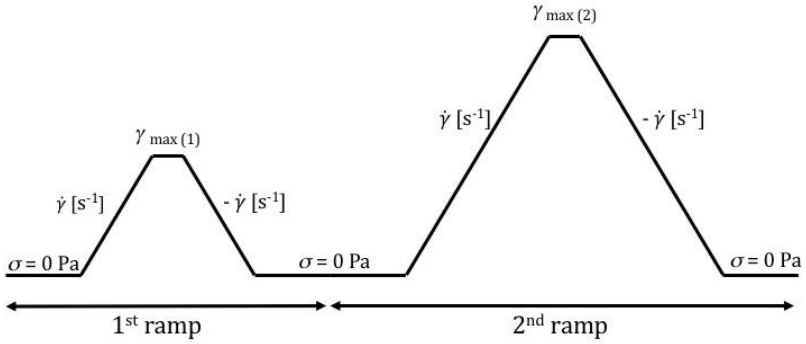

Figure 44. Protocol of time-linear shear strain ramps

For the case of successive ramps, the maximal strain was set at 12.5% for the first ramp, 25% for the second ramp and then increments of 25% were applied for each cycle until 250%. The instantaneous modulus G_{inst} (also called differential [20], tangent [8,9] or nonlinear [6,7] modulus) was calculated as $G_{inst}=d\sigma/d\gamma$.

3 Results and discussion.

3.1 Fibrinogens characterization

Combined mass spectrometry and size exclusion chromatography of fibrinogens showed that Clottafact and Fib1 have almost identical compositions in co-purified proteins as well as less degraded α–chains than Riastap [15]. DLS results showed that the fibrinogen Clottafact, 35nm size-filtered, is close to monodisperse with a hydrodynamic size of 11nm. Conversely, Fib1 and Riastap fibrinogens presented polydisperse broad peaks at ~22nm, indicating mixtures of higher molecular weight species, including probably fibrinogen aggregates.

3.2 Structure of fibrin

As described in detail in our previous work [15], we determined the impact of fibrinogen composition on the multi-scale structure of fibrin. Briefly, it was observed that Clottafact clots were formed with almost crystalline, straight fibres, while both Fib1 and Riastap fibres were considerably more snake-like and internally less organized. Those nano-structural observations were confirmed using confocal microscopy. Results suggested that the fibrinogen molecular weight distribution controls fibres packing and thus the geometry and rigidity of the fibres. A remaining question concerns the influence of those structural differences on the rheology of the clots.

3.3 Rheology

First we determined the influence of the nature of fibrinogen on the structure of fibrin. This article quantifies the influence of fibrinogen on the mechanical properties of fibrin clots and their scenarios of rupture. To do so, we determine the rheological behaviour of fibrin clots from these three different fibrinogens in the linear and nonlinear regimes.

3.3.1 Linear rheology

As can be seen in Figure 46, the linear viscoelastic domain for the different fibrin clots always extends up to about 1% deformation; thus, the linear viscoelasticity is obtained at 0.1% deformation. Figure 45-up shows the viscoelastic spectra obtained at a fibrinogen concentration of 3 mg/ml for each of the three samples. As observed many times [6,8,21], for all clots the elastic moduli are larger than the dissipation moduli and almost constant for the range considered (0.1-10Hz), while the dissipation moduli grow slowly with frequency.

For all fibrinogen concentrations, Fib1 and Riastap clots show similar elastic moduli (G'), while Clottafact's is about 4 times larger. As shown in Figure 45-down, the plateau elastic modulus (measured at 0.6Hz, 0.1%) increases with concentration as $c^{2.2}$, following nicely the $c^{11/5}$ scaling predicted for semi-flexible polymers [8,22].

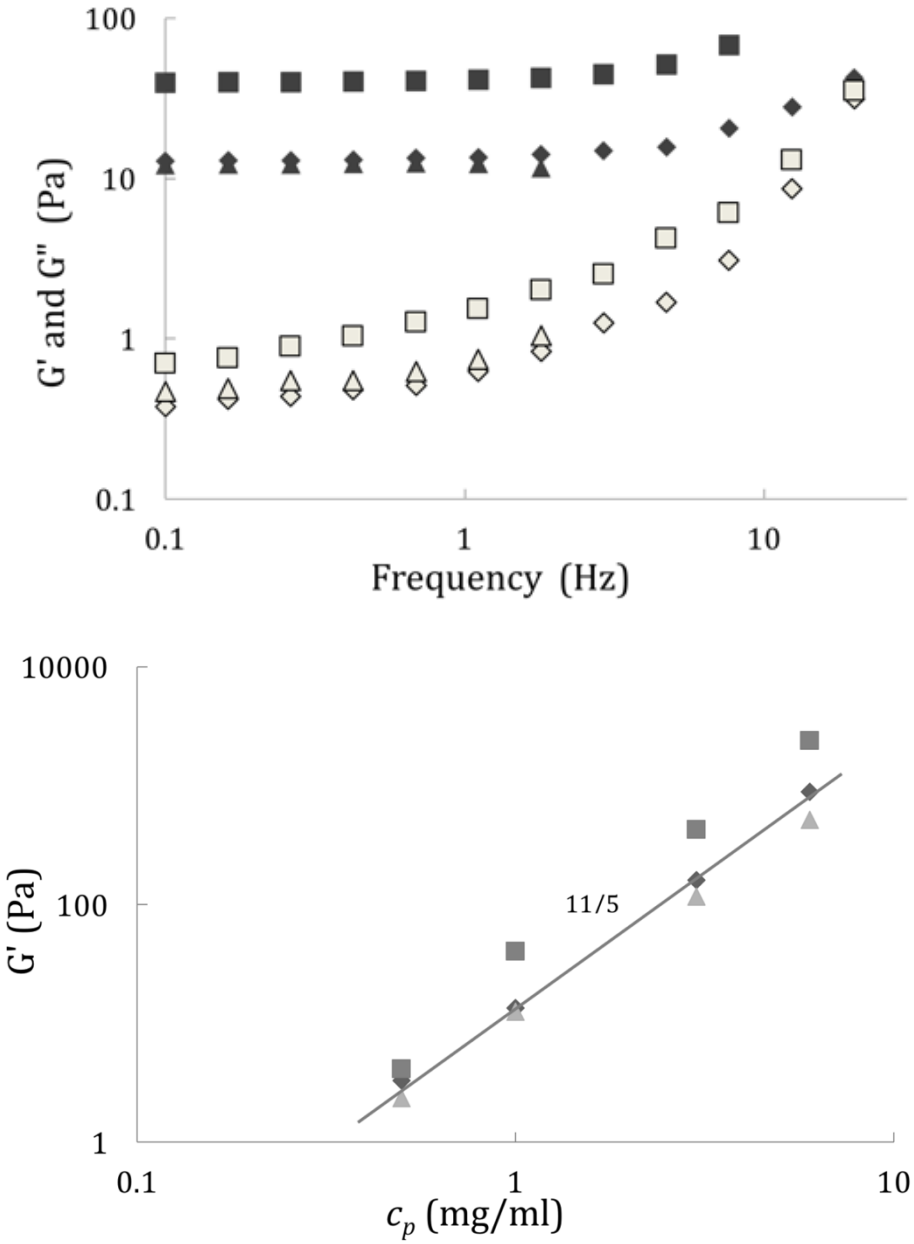

Figure 45. (Up): Elastic and loss moduli of fibrin gels at [Fg]=3mg/ml (the same figures are respected) for a frequency range (0.1 to 10 Hz)

(Down): Viscoelastic regime at 0.6Hz as a function of concentration of fibrinogen. Clots from the fibrinogens: Clottafact (squares), Fib1 (diamonds) and Riastap (triangles).

3.3.2 Nonlinear rheology of fibrin gels

Then, we determined the mechanical properties of fibrin clots at high strains. As explained in the materials and methods section, we applied either a single or successive time-linear shear strain ramps for each fibrin clot and determined the instantaneous elastic moduli.

The nonlinear mechanical responses of Fib1 and Riastap fibrin clots are essentially superimposed (data not shown) while differing strongly from Clottafact gels. From now on, since Fib1 and Riastap rheological measurements are always very close to each other, only Fib1 and Clottafact results will be displayed.

3.3.2.1 Single shear strain ramps

In Figure 46 we represent the shear strain single ramps obtained for both Fib1 and Clottafact fibrin gels at [Fg] = 1, 3 and 6 mg/ml and [IIa]=0.1 IU/ml.

For small strains (γ < 1%), fibrin gels instantaneous moduli show a plateau, corresponding to the expected viscoelastic linear domain. As explained above (*cf.* section 3.3.1), the initial instantaneous modulus (*i.e.* the plateau elastic modulus) from Fib1 fibrin gels are ~4 times lower than Clottafact's for each concentration. At larger strains, the gels show a strain stiffening behaviour, *i.e.* an increase of the instantaneous modulus (G_{inst}) with increasing strain, in agreement with the literature [4,6–10].

All Fib1 clots (Figure 46-left), as well as Clottafact clots below [Fg] = 1mg/ml (Figure 46-right), present similar characteristics. The clots begin to stiffen at about 1% strain and the instantaneous modulus increases monotonously at different rates depending on fibrinogen concentration, as described by Weigandt *et al.* [6]. Finally, at high strain deformation ($\gamma \sim 100\%$) we observe the failure of the clot, which signature is a sudden and large decrease of the measured instantaneous modulus.

The nonlinear behaviour of Clottafact clots above [Fg] = 1 mg/ml also begins by a strain stiffening regime. However, these clots present a secondary plateau (3mg/ml) or a decrease (6mg/ml) between 10% > γ > 20%, followed by a second strain stiffening regime up to the failure of the clot as previously observed by Weigandt *et al* [7]. The second strain stiffening regime evolves monotonously and at $\gamma \approx 100\%$ suddenly increases with a slope $K' \sim \sigma^{3/2}$ (as already observed by Piechocka *et al* [8]), finally

leading to the rupture of the clot. This is illustrated on Figure 47, which represents the instantaneous moduli as a function of stress for Clottafact clots ([Fg] = 3 and 6 mg/ml)

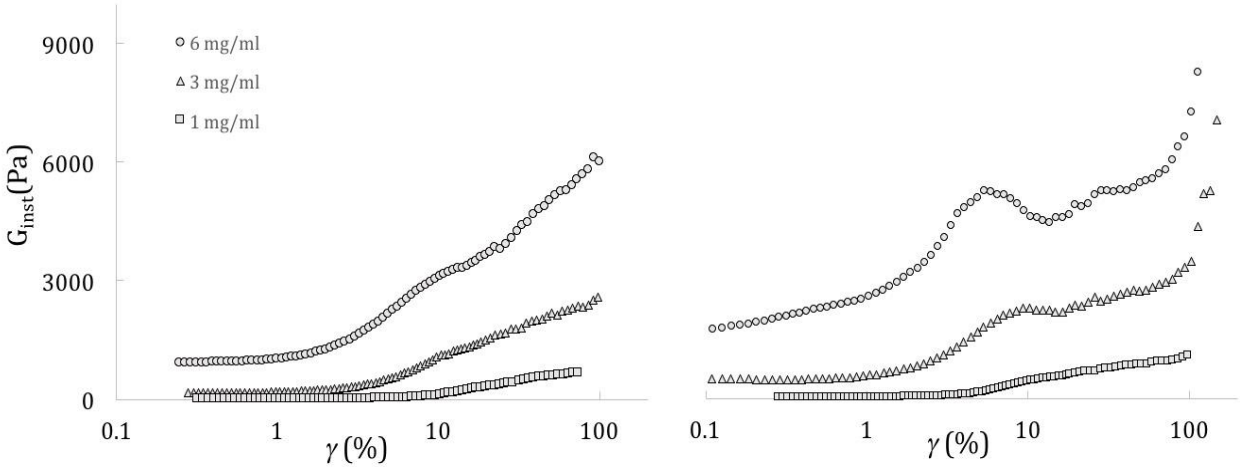

Figure 46. Fibrin clots from Fib1 (left) and Clottafact (right). Single shear strain ramps (until rupture) for [Fg] = 0.4 mg/ml (diamonds), 1 mg/ml (squares), 3 mg/ml (triangles) and 6 mg/ml (circles)

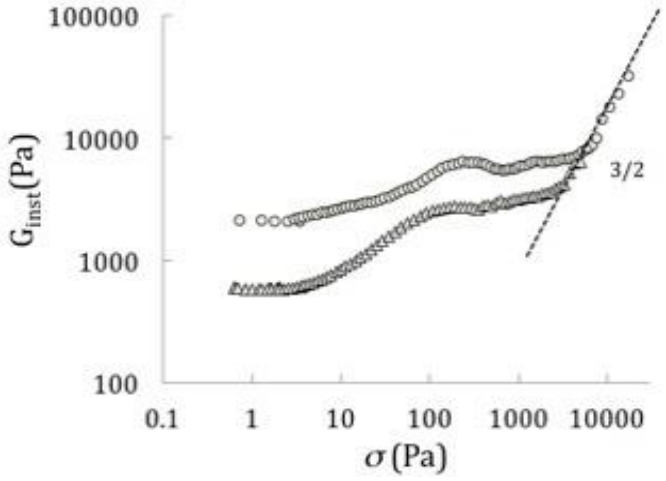

Figure 47. Shear stress ramps until rupture of fibrin clots from Clottafact for [Fg]= 3 and 6 mg/ml (triangles and circles respectively)

3.3.2.2 Successive shear strain ramps

Since blood flow is not oscillatory, but rather the unidirectional superposition of an oscillatory and a steady state flow, we determine the mechanical history dependence of the nonlinear response of fibrin gels using an asymmetric test by performing successive, increasing shear strain ramps. Here, we present and discuss the results corresponding to the instantaneous moduli (G_{inst}) and normal forces of Fib1 and Clottafact fibrin clots at [Fg] = 3 and 6 mg/ml (Figure 48 and Figure 49 respectively).

At [Fg] = 3 mg/ml, Fib 1 clots (Figure 48 up-left) show perfectly superimposed curves of the instantaneous moduli for the first applied ramps. This means that no permanent modifications are inflicted to the gel until the maximum strain of the ramp attains γ = 75%. After this ramp, the effect of repeating the strain ramp while increasing the maximum strain is to significantly increase the linear viscoelasticity of the clot (inset of Figure 48 up-left). This leads to successive higher instantaneous moduli plateaux for low strains (represented by the blue arrow). In other words, work hardening is observed in Fib1 clots. However, this behaviour has no repercussion on the nonlinear regime, where the curves remain superimposed until the rupture of the clot. At higher concentrations (6 mg/ml), the evolution of Fib1 clots (Figure 49 up-left) shows the same behaviour as for lower concentrations, with the only exception of the increase of the strain stiffening slope until the failure of the clot.

The linear viscoelasticity (γ < 1%) of Clottafact clots at 3 mg/ml (Figure 48 up-right) is rather unaffected by the successive ramps. That is not the case for higher strains, where we observe a more intricate behaviour of the instantaneous moduli. Clottafact's curves are superimposed until the ramps reach 75% of deformation. Above this ramp, we observe a progressive disappearance of the "plateau zone" first observed between 10% > γ > 30%. The nonlinear response evolves from the three regimes previously explained (strain hardening – constant plateau – strain hardening) to a monotonous strain hardening regime from $\gamma \approx 1\%$ until the failure of the clot ($\gamma \approx 135\%$). This evolution of the regimes is illustrated with a blue arrow in Figure 48 (frame up-right).

Clottafact clots at 6mg/ml (Figure 49 up-right) behave similarly than at 3 mg/ml. For the first ramps, the clots act as described for the case of single shear strain ramps

(*i.e.* strain stiffening – strain softening – strain stiffening). Then, just after the ramp of γ = 75%, a progressive change of regimes leads to a monotonous strain stiffening curve until the failure of the clot.

Considering now the normal forces, Fib1 clots at 3 mg/ml (Figure 48 down-left) display almost superimposed curves (which reach a maximum value of ~0.4 N) until the failure of the clot. This is in agreement with the behaviour observed for the instantaneous moduli. Moreover, at 6 mg/ml (Figure 49 down-right) normal forces also evolve as just described.

The moduli of the normal forces for Clottafact gels (Figure 48 down-right) show a transition between regimes, which is in agreement with the results of the instantaneous moduli. The normal forces on the first regime (1% > γ > 50%) evolve monotonously and the curves corresponding each successive ramp are superimposed. However, for the ramp of γ = 75%, the measured normal force surprisingly increases 10-fold, establishing a second regime in agreement with the second regime for the instantaneous modulus The same behaviour is observed at 6 mg/ml (Figure 49 down-right), yet the maximal modulus of the measured normal force is almost twice higher with the increase of concentration.

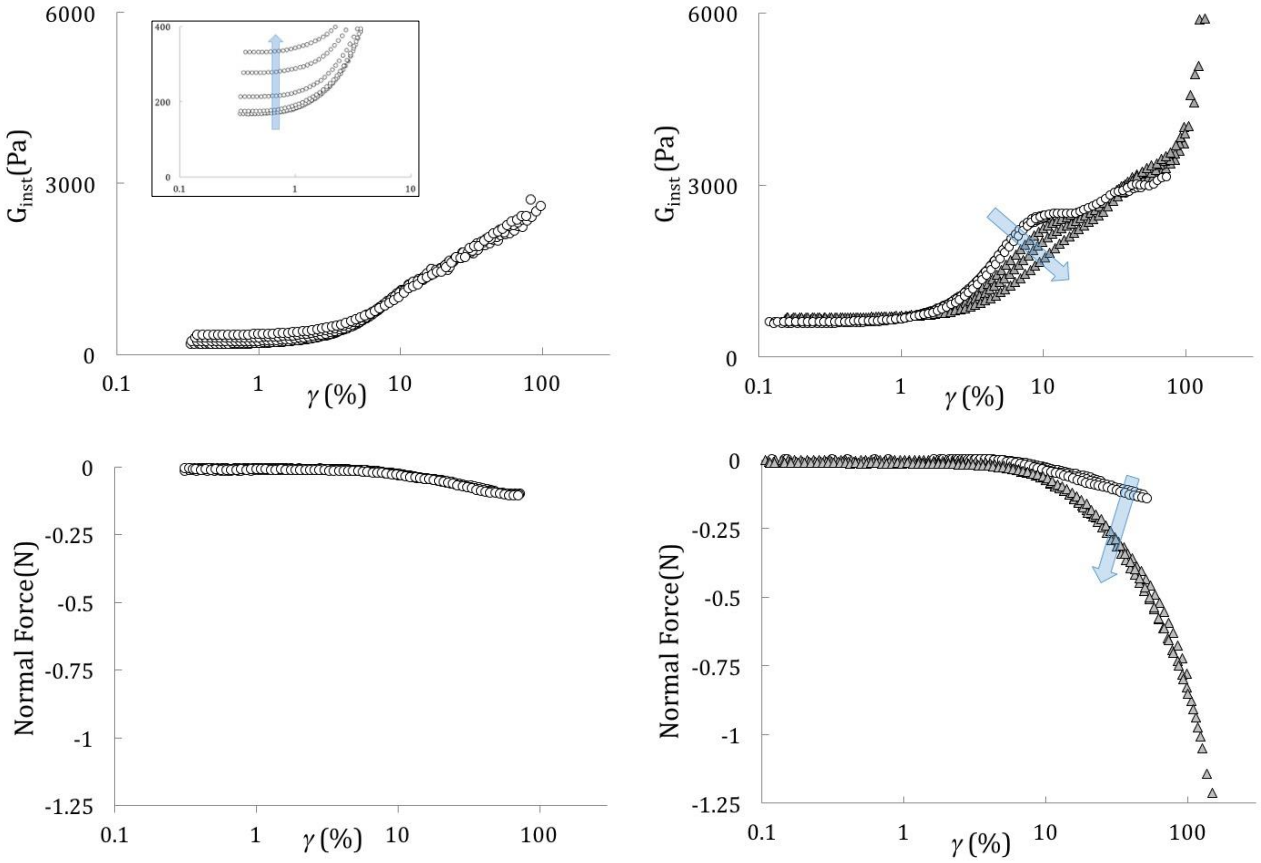

Figure 48. Successive shear strain ramps at [Fg]= 3 mg/m. Left (up and down) frame correspond to Fib1 clots; right frames correspond to Clottafact clots.

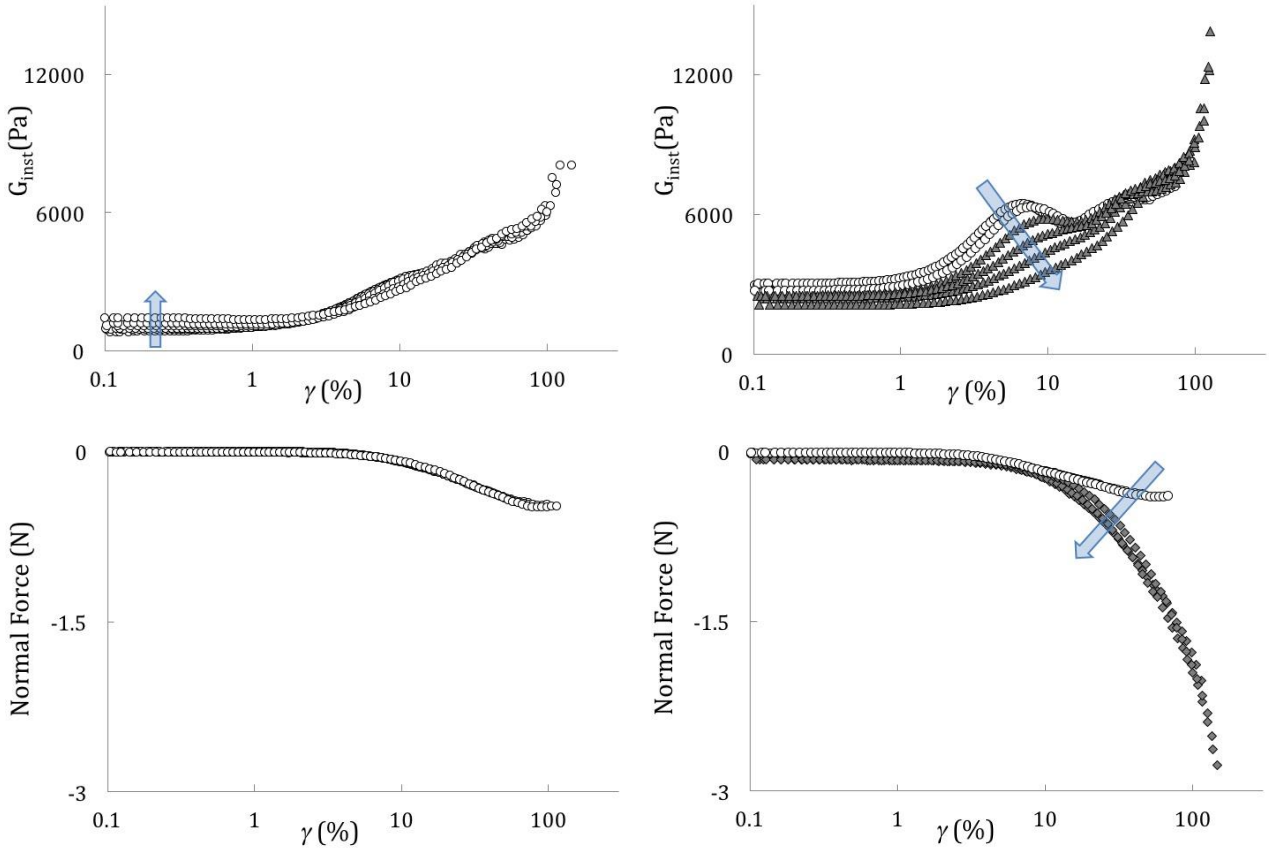

Figure 49. Successive shear strain ramps at [Fg]= 6 mg/ml. Left (up and down) frames correspond to Fib1 clots; right frames (up and down) correspond to Clottafact clots.

3.3.3 Fibrin gels rupture

Now, we concentrate on the different rupture scenarios from each clot. Figure 50 illustrates the evolution of the instantaneous moduli and the normal forces for Fib1 and Clottafact clots after and before the failure. Only the curves at [Fg] = 3 mg/ml are represented because no qualitative differences were observed between the different concentrations in terms of rupture scenarios.

As shown for Fib1 clots (Figure 50 left-up and down), the successive instantaneous moduli, and normal forces are superimposed until failure occurs. Once it happens, the next applied ramp shows a dramatic decrease of the measured instantaneous moduli, and of the normal force modulus. This indicates that the clot has suffered a complete failure, estimated at at γ= 116% (3mg/ml).

The rupture scenario corresponding to Clottafact clots (Figure 50 up and down-right) is different than for Fib1 clots. After the second (fatigue) regime observed for both the instantaneous moduli and the normal forces, a slow decrease of the instantaneous and normal force modulus is observed from γ=150% onwards.

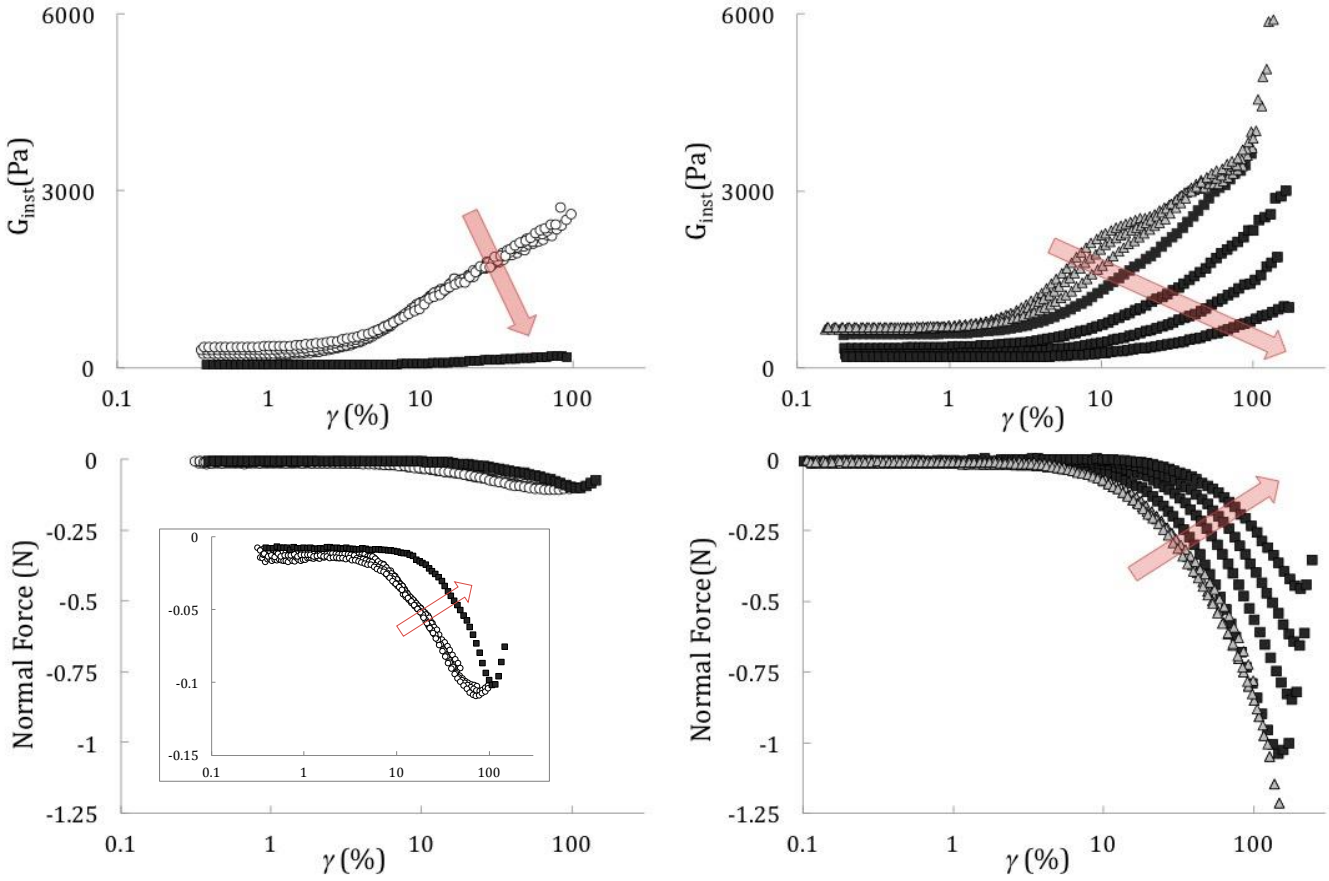

Figure 50. Rupture scenarios of Fib1 (left-up and down) and Clottafact (right-up and down) clots

To quantify the rupture scenarios for all tested concentrations, we represent the linear instantaneous modulus measured for each successive ramp (noted as G_{inst} (0)), *i.e.* the evolution of the linear viscoelasticity before and after the rupture of the clot.

Fib1 clots (Figure 51-left), for all tested concentrations, show the linear viscoelastic plateau followed by work hardening, and then failure. The strain at which failure occurs depends on concentration as seen by Piechocka *et al.* [9].

As observed above, the evolution of G_{inst} (0) for Clottafact clots is different. First, as it is illustrated on Figure 51-right, there is no work hardening except at 1mg/ml. Moreover, once the clot starts to fail, the G_{inst} (0) of each successive ramp decreases smoothly.

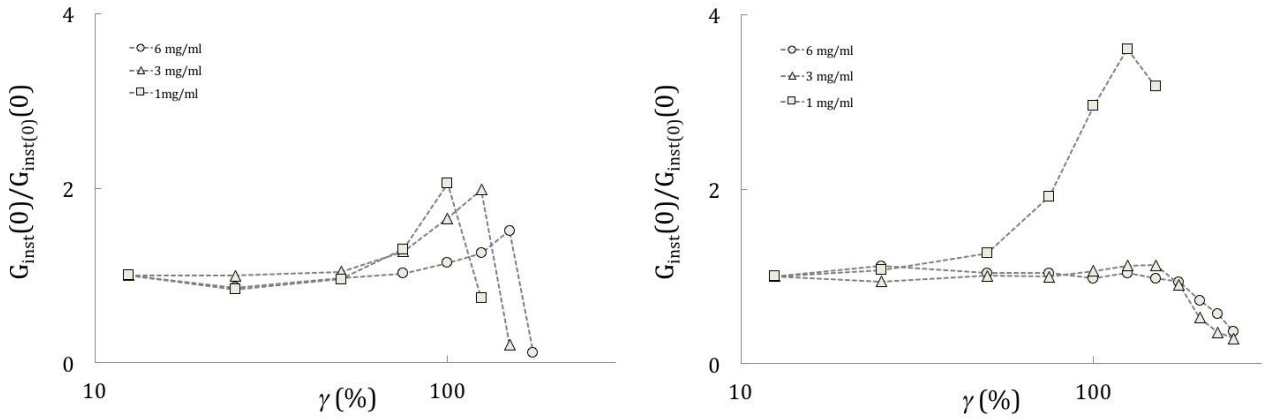

Figure 51. Evolution of the linear viscoelasticity for Fib1 (left) and Clottafact (right) clots

4 Conclusion

We have shown in this work that most of the viscoelastic properties of fibrin are dependent upon the nanostructure of the fibres. First, the elastic moduli of porous fibres (Fib1 and Riastap) are significantly lower than those made of crystalline fibrin fibres (Clottafact). Strikingly, when large strains are applied, porous fibres show monotonous strain stiffening while fibrin clots made of crystalline fibres present a well-defined intermediate regime in the form of either a second linear regime or strain softening.

Under fatigue conditions, porous clots show work hardening which affects the linear viscoelastic regime, while the nonlinear regime is strictly unaffected. Conversely, crystalline clots rheology does not show any work hardening, but is modified in the nonlinear regime, leading to the disappearance of the intermediate regimes described above. Finally, the rupture scenarios of fibrin clots are also related to the structure. While porous clots show a dramatic failure, crystalline clots present a much more progressive failure.

In conclusion, we showed that the structure of fibrin fibres drastically influences the the linear and nonlinear rheological properties, as well as the rupture scenarios of fibrin clots.

References

1 Undas A, Ariëns RAS. Fibrin clot structure and function: A role in the pathophysiology of arterial and venous thromboembolic diseases. *Arterioscler Thromb Vasc Biol* 2011; **31**: e88-99.

2 Nelb GW, Gerth C, Ferry JD, Lorand L. Rheology of fibrin clots: III. Shear creep and creep recovery of fine ligated and coarse unligated clots. *Biophys Chem* Elsevier; 1976; **5**: 377–87.

3 Mockros LF, Roberts WW, Lorand L. Viscoelastic properties of ligation-inhibited fibrin clots. *Biophys Chem* 1974; **2**: 164–9.

4 Janmey P a. Rheology of Fibrin Clots. VI. Stress Relaxation, Creep, and Differential Dynamic Modulus of Fine Clots in Large Shearing Deformations. *J Rheol (N Y N Y)* 1983; **27**: 135.

5 Kang H, Wen Q, Janmey PA, Tang JX, Conti E, MacKintosh FC. Nonlinear Elasticity of Stiff Filament Networks: Strain Stiffening, Negative Normal Stress, and Filament Alignment in Fibrin Gels. *J Phys Chem B* American Chemical Society; 2009; **113**: 3799–805.

6 Weigandt KM, Pozzo DC, Porcar L. Structure of high density fibrin networks probed with neutron scattering and rheology. *Soft Matter* 2009; **5**: 4321.

7 Weigandt KM, Porcar L, Pozzo DC. In situ neutron scattering study of structural transitions in fibrin networks under shear deformation. *Soft Matter* 2011; **7**: 9992.

8 Piechocka IK, Bacabac RG, Potters M, Mackintosh FC, Koenderink GH. Structural hierarchy governs fibrin gel mechanics. *Biophys J* Biophysical Society; 2010; **98**: 2281–9.

9 Piechocka IK, Jansen KA, Broedersz CP, Kurniawan NA, MacKintosh FC, Koenderink GH. Multi-scale strain-stiffening of semiflexible bundle networks. *Soft Matter* Royal Society of Chemistry; 2016; **12**: 2145–56.

10 Storm C, Pastore JJ, MacKintosh FC, Lubensky TC, Janmey PA. Nonlinear elasticity in biological gels. *Nature* Nature Publishing Group; 2005; **435**: 191–4.

11 Onck PR, Koeman T, van Dillen T, van der Giessen E. Alternative Explanation of Stiffening in Cross-Linked Semiflexible Networks. *Phys Rev Lett* American Physical Society; 2005; **95**: 178102.

12 Brown AEX, Litvinov RI, Discher DE, Purohit PK, Weisel JW. Multiscale mechanics of fibrin polymer: gel stretching with protein unfolding and loss of water. *Science* 2009; **325**: 741–4.

13 Huang L, Lord ST. The isolation of fibrinogen monomer dramatically influences fibrin polymerization. *Thromb Res* Elsevier; 2013; **131**: e258-63.

14 Huang L, Hsiao JP-L, Powierza C, Taylor RM, Lord ST. Does topology drive fiber polymerization? *Biochemistry* American Chemical Society; 2014; **53**: 7824–34.

15 Garcia X, Seyve L, Polack B, Caton F. Fibrinogen polydispersity controls fibrin multiscale structure. 2016; .

16 Yeromonahos C, Polack B, Caton F. Nanostructure of the fibrin clot. *Biophys J* Biophysical Society; 2010; **99**: 2018–27.

17 Dassi C. La Fibrinographie : Une méthode multi-longueurs d'ondes pour la détermination

de la structure du caillot en plasma. University Joseph Fourier; 2016.

18 Clauss A. Gerinnungsphysiologische Schnellmethode zur Bestimmung des Fibrinogens. *Acta Haematol* Karger Publishers; 1957; **17**: 237–46.

19 Münster S, Jawerth LM, Leslie BA, Weitz JI, Fabry B, Weitz DA. Strain history dependence of the nonlinear stress response of fibrin and collagen networks. *Proc Natl Acad Sci U S A* National Academy of Sciences; 2013; **110**: 12197–202.

20 Münster S, Jawerth LM, Fabry B, Weitz DA. Structure and mechanics of fibrin clots formed under mechanical perturbation. *J Thromb Haemost* 2013; **11**: 557–60.

21 Roberts WW, Kramer O, Rosser RW, Nestler FHM, Ferry JD. Rheology of fibrin clots I. *Biophys Chem* 1974; **1**: 152–60.

22 MacKintosh FC, Käs J, Janmey PA. Elasticity of Semiflexible Biopolymer Networks. *Phys Rev Lett* American Physical Society; 1995; **75**: 4425–8.

General conclusions

Fibrin clots stop bleeding and serve as a skeleton for wound healing. Moreover, fibrin clots must resist perturbations such as blood flow at the site of vascular injury. In order to perform this function, fibrin fibres present a complex internal structure that is thought to control fibrin clots non-linear mechanics. In order to investigate this relationship, ways to change this nanostructure without changing the reaction conditions had to be found.

In this thesis, we first show that fibrinogen's polydispersity profiles provide a new control parameter for the structure of fibrin. SAXS and spectrophotometry demonstrated that monodisperse fibrinogens build almost crystalline fibres, while polydisperse fibrinogens form much less organized fibres. This has also been confirmed at the micron scale by confocal microscopy, where monodisperse fibrinogens exhibit much higher straightness and rigidity than those exhibited by polydisperse fibrinogens. Therefore, the polydispersity profile of fibrinogen controls the fibrin fibre's packing and hence the geometry and rigidity of the fibres.

Second, we have analysed the structure-mechanics relation of fibrin clots. We show that the mechanical properties of fibrin clots depend strongly on the nanostructure of fibrin. Repetitively strained amorphous fibrins only show modifications of the linear viscoelastic regime (work hardening) up to their failure. In contrast, crystalline fibrin does not present work hardening, but very surprising features at large strains. Indeed, a well-defined second linear viscoelastic regime, or even a strain softening regime is observed before the final inextensible strain hardening regime. These structural and mechanical differences also impact the failure of the clots: less organized clots fail dramatically while crystalline, more organized clots present a progressive failure.

This work opens outstanding questions regarding the influence of polydispersity on the polymerization of fibrin, as well the mechanical properties of fibrin clots formed from mono and polydisperse fibrinogens. This could be of paramount interest for tissue engineering on fibrin scaffolds.

Appendix

Fibrinography: A multiwavelength light-scattering assay of fibrin structure

Carhel DASSI[1], Xabel GARCÍA[1], Landry SEYVE[2], Benoît POLACK[2], and François CATON[1]

[1]Laboratoire Rhéologie et Procédés, CNRS UMR 5520, Université Grenoble Alpes

[2]Laboratoire TIMC-IMAG TheREx, CNRS UMR 5525, University Grenoble Alpes, and Department of Hematology, University Hospital Grenoble Alpes

In addition to the work realized regarding the structural and mechanical properties of fibrin clots. I have participated in the investigation of the pertinence of the previously developed structural assay dedicated to purified fibrinogen-thrombin systems test, called Fibrinography, in plasma. We show that Fibrinography determines quantitatively the nanostructure of fibrin fibers in plasma. We compared this assay with the commonly used single wavelength turbidity method, showing that the latter is not a proper structural assay, but determines essentially the fibrinogen content in plasma. In addition, Fibrinography showed clear discrimination of several hypercoagulant plasmas, as well as an excellent proportionality between anticoagulant concentration, maximum velocity time, and number of protofibrils at this time.

1 Introduction

Thrombosis-related diseases are a major and increasing public health problem, generating very high cumulated costs, both in human and economic terms. For that reason, the timely diagnosis, risk stratification and monitoring of treatment of thrombosis is crucial. However, the clinical assays available today only evaluate fibrin formation time, either using activated partial thromboplastin time (aPTT) or Prothrombin Time (PT). Those tests are mainly sensitive to clotting factors deficiencies and usually measure clotting time increase, while shortening of those times is commonly attributed to pre-analytical errors. While those tests might be pertinent, they are currently of limited use in the diagnosis and follow up of patients with hypercoagulant diseases, highlighting the current need for new haemostatic global assays.

Such an assay of thrombotic conditions and treatment would be easy to perform with excellent sensibility and specificity, while stratifying properly both the thrombotic and bleeding risks.

Such a clinical assay does not yet exists, despite many encouraging attempts. The first test that comes to mind is the one that characterizes the main physiological property of blood clots: its resistance to blood flow. This property is usually measured by thromboelastography (TEG) which is independent of optical phenomena and readily applicable to whole blood. Those elasticity measurements determine clot formation, maturation and lysis in real time. While the main clinical use of TEG concerns the bleeding risk in surgical settings [1-3] there has been a number of clinical evaluations of its ability to predict thromboembolic events. Dai et al. systematic review of the literature on this topic [4] concludes that more clinical studies are necessary since the sensitivity and specificity of the method are currently insufficient (resp. [0% to 100%] and [62% to 92%]). Those insufficiencies are probably related to the discrimination and reproducibility issues highlighted in Lipets et al. and Lancé's reviews [5,6], as well as to the difficulty in the method's standardization.

The mechanical properties of the clot are the result of fibrin formation which itself comes from the cleavage of fibrinopeptides by thrombin. Therefore, another important hemostatic test investigates the temporal evolution of the thrombin concentration in plasma, thanks to a fluorescent technique. The main interest of this

method is that it provides different informations than the aPTT, PT and TEG assays as it does not stop at fibrin formation. Two recent clinical studies confirmed this point both for managing bleeding patients [7] as well as for predicting bleeding for patients undergoing cardiac surgery [8]. Concerning hypercoagulability however, the review by Lipets [5] suggests that once more the reproducibility of the method is insufficient. Indeed, while the difference in the mean parameter values is significant, the standard deviations usually overlap, which makes it complicated to transform such results into a clinical recommendation [5]. Furthermore, although thrombin generation test standardization is presently under development [9] its lack currently restricts the method application.

Finally, the link between thrombin generation and the viscoelastic properties of the clot is through the structure of the fibrin clot. In the more fundamental literature, a rather large number of methods have been used to study the mature structure of the fibrin clot at different scales. Indeed, the fibrin clot structure has been studied by using "direct" methods such as electron and confocal microscopy [10-12] or X-ray or neutron scattering [13-15] or using "indirect methods" (i.e. involving some modeling), such asviscoelastic and spectral analysis [16], clot permeation [17] and light scattering [14,18-21]. However, the use of the direct methods is restricted to very specialized laboratories especially for X-ray and neutron scattering, while microscopy methods are not well adapted to kinetic measurement and not suited to the clinical environment. On the other hand, most indirect methods are little adapted to clinical investigations for practical reasons (blood volume, absence of normalization, test duration…) while turbidimetry, which is a form of light scattering, looks most promising given its apparent simplicity.

Since the seminal work of Casassa (1955) [22], several groups attempted to deduce quantitatively the radius and mass-to-length ratio of fibrin fibres from wavelength-resolved turbidity data [14,15,21,23]. Carr and Hermans (1978) further argued that, for sufficiently thin fibres, their mass-to-length ratio could be directly determined from a single wavelength turbidity measurement of a mature clot. While this result was obtained in a purified system (fibrinogen+thrombin), this simplification has been shown to be invalid for plasma [24]. Despite this unambiguous result, it is still widely believed that the turbidity of a clot is essentially proportional to the thickness of

the fibres [e.g. Undas 2001 and references herein]. Therefore, the main structural assay used today consists simply in following turbidity at a single wavelength during clot formation (and eventually lysis). This method has been used in a large number of studies, in particular in attempts to find biomarkers in cardiovascular diseases [17]. Two kinds of information can be extracted from such measurements: the temporal characteristics (e.g. clotting and lysis times) and the turbidity of the mature clot. Concerning the temporal evolution of the turbidity clinically useful test has been derived: "Waveform Analysis" which is a PT test combined with a light transmission setup [5,25]. In this particular test, the obtained curve is a sensitive predictor of Disseminated Intravascular Coagulation [5,26-28]. Concerning the turbidity of the mature clot on the other hand, while correlations with diseases where obtained (e.g. Undas et al. 2001 and references herein), no sensitivity and specificity study has ever been performed. Furthermore, those turbidity tests are standardized neither in their optical setup (pathlength, chosen wavelength), nor in the reagents. Finally, it is important to notice that this maximum turbidity assay closely resembles that of the PT-derived fibrinogen dosage (e.g. Palareti 1991 and Mackie 2002) [29,30]. To summarize, while turbidimetry is indeed a promising method, it strongly lacks validation as well as normalization. Therefore, there is still a pent-up need for a quantitative, reliable and normalized method measuring the structure of the fibrin clot as it forms in plasma, method usable in clinical laboratories.

To fill that need, we propose a novel fibrin structure assay, Fibrinography, based on the dynamic measurement of the number of protofibrils in fibrin fibres in real-time, as a potential biomarker to discriminate thrombosis and haemostasis risk. This assay is a transposition to plasma of the multiwavelength light scattering assay that we previously developed in purified systems (Yeromonahos 2010 – 2012) [14,15].

2 Materials and methods

Three lyophilized control plasmas (Normal, Protein S depleted, and Heparinized) were obtained from Diagnostica Stago, France, with fibrinogen concentrations of respectively 2.53, 2.44 and 2.78 g/L. The deficient TFPI (Tissue Factor Pathway Inhibitor) plasma was immuno-depleted; its fibrinogen concentration was 2.2 g/L. A frozen normal plasma pool was obtained from normal donors; its final fibrinogen

concentration was 2.5 g/L (Diagnostica Stago). Different fibrinogen concentrations (range 1.23 to 11.23g/L) were added to this plasma (purified fibrinogen from ERL).

Initiation of coagulation activation was realized using a method close to the one of Hemker (1993). Briefly, 100µL of 12pM of Tissue Factor (TF) and 24µM phospholipids (PPL) (Thrombinoscope, Maastricht, the Netherlands) were mixed with 400µL of plasma, and clotting was triggered upon addition of 100µL $CaCl_2$ (16.7mM, final concentration). Light scattered by the forming clot was measured from 500nm to 820nm (2nm resolution), every 3 seconds during 30 minutes at 37°C (±0.5°C) in a prototype multichannel spectrophotometer based on Ocean Optics USB650 spectrophotometers.

2.1 Fibrinography

Fibrinography determines the temporal evolution of the number of protofibrils inside fibrin fibres as well as the radius of those fibres during plasma clot formation. Briefly each wavelength-dependent turbidity spectrum is related to the structure of the fibrin fibres according to equation 1 (Yeromonahos 2010):

$$\tau(t,\lambda)\lambda^5 = A\mu(t)C_F[\lambda^2 + Ba(t)]$$

where τ: turbidity; t: time; λ: wavelength; C_F: fibrinogen concentration; $A = \pi^3 n_S \left(\frac{dn}{dc}\right)^2 \cdot \frac{88}{15}$ and $B = \pi^3 n_S^2 \cdot \frac{92}{77}$, constants; μ: lineic mass; a: radius. Since eq. 1 shows that $\tau(t,\lambda)\ \lambda^5$ is a linear function of λ^2, the lineic mass µ and the radius a of the fibres are determined at each time step by a linear fit. The number of protofibrils is determined at each time step from the lineic mass: Np = μ/μ_0 where $\mu_0 = 144.10^{11}$Da/cm is the lineic mass of a protofibrils [14].

2.2 Thrombin Generation

Thrombin generation was measured using the Calibrated Automated Thrombogram (CAT) initiated by automatically dispensing fluorogenic substrate (Z-Gly-Gly-Arg-AMC) in $CaCl_2$ (416µM and 16,7mM, final, respectively), calibrated against wells containing α_2-macroglobulin/thrombin complex and plasma, and analyzed with Thrombinoscope (Thrombinoscope BV, Maastricht, the Netherlands), according to Hemker's method [31]. Final TF and PL concentrations were 2pM and 4µM, respectively.

2.3 Confocal microscopy

Ten percent fluorescent fibrinogen (Alexa Fluor 488, Molecular Probes, USA) was added to 200µL of plasma. After incubation with 50µL of 2pM TF and 4µM PPL, clotting was triggered by adding 50µL of $CaCl_2$ (16.7mM, final concentration). Confocal stack images were taken after 30 minutes of fibrin network formation. Images at different depth were compared to ensure that the network was homogeneous.

3 Results and discussion

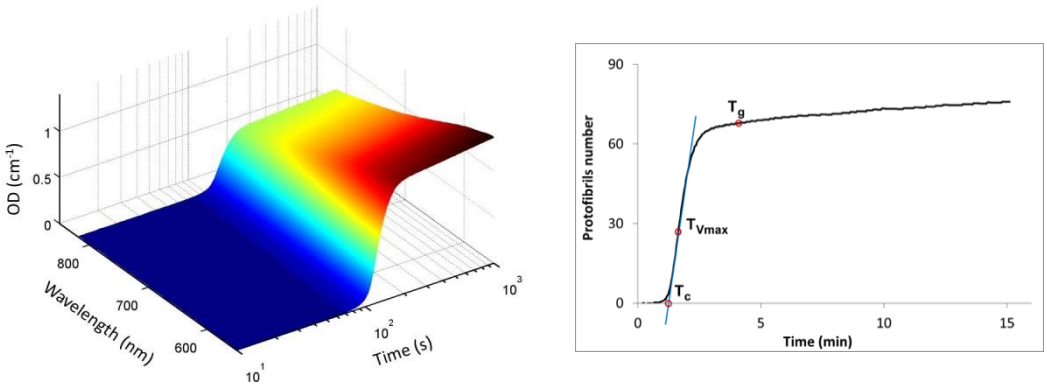

Figure 1. Typical temporal evolution of optical density spectra and of the number of protofibrils in fibrin fibers during a clotting experiment.1a) Optical Density vs time and wavelength for a normal plasma. 1b) Temporal kinetics of the number of protofibrils for the same plasma, data extracted from figure 1a. Coagulation was triggered with 16,7mM CaCl2 in the presence of 2pM TF and 4µM phospholipids.

3.1 Fibrinogram

The typical evolution of optical density spectra during a clotting experiment is shown on figure 1a. From those data, the number of protofibrils inside the fibres and the radius of the fibres are extracted using eq. 1 as described in materials and methods. The temporal evolution of the number of protofibrils plotted in fig. 1.b is called a fibrinogram.

From a fibrinogram, several parameters can be determined such as:

- The time of maximum reaction velocity (inflexion point) T_{Vmax}
- The clotting time T_c: extrapolation on the abscissa of the maximum velocity tangent

- The fibres growth time (reaction velocity down to 3% of max velocity) T_g
- The protofibrils number at T_g

3.2 Reproducibility of the assay.

Fibrinography was replicated 40 times for the three lyophilized control plasmas, on several days. Fig. 2 shows the excellent reproducibility of the assay since coefficients of variation (CV) for the normal and PS depleted plasmas were lower than 5%, while culminating to 8% for the heparinized plasma (Table 1). These CVs can be compared to those > 20% of the CAT assay [32]. In addition, all replicates were within two standard deviations. As expected, the clotting time for the heparinized plasma was longer than for the other two.

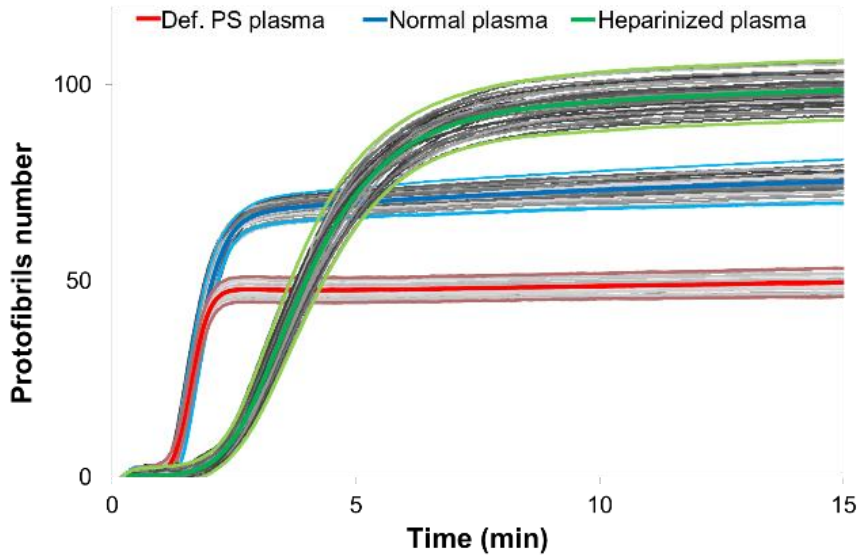

Figure 2. Reproducibility of Fibrinography for the normal ([Fib] = 2.53g/L), heparinized ([Fib] = 2.78g/L), and def. PS ([Fib] = 2.44g/L) plasmas. N=40; for each plasma all replicates are within 2 SD.

	Coagulation Parameters				
Types of control plasmas n=40		**T_c (sec.)**	**T_{Vmax} (sec.)**	**T_g (sec.)**	**N_{pmax}**
Control Normal ([Fib] = 2.53g/L)	**Mean**	78.1	97.7	198.7	75.4
	CV (%)	4.34	4.87	4.54	3.70
Control Heparinized ([Fib] = 2.78g/L)	**Mean**	143.8	209.1	572.8	98.6
	CV (%)	5.08	7.07	6.87	3.86
Control Deficient Protein S ([Fib] = 2.44g/L)	**Mean**	76.0	95.3	148.5	49.7
	CV (%)	2.66	3.02	2.64	3.58

Table 1 : Coagulation kinetics and quantitative parameters Tc: Clotting Time; T_{Vmax}: Time of maximum reaction velocity (inflexion point); Fibres growth time: Tg; N_{pmax}: Maximum number of protofibrils

3.3 Comparison with single wavelength turbidimetry.

We first compare Fibrinography with the widely used turbidity measurement performed at a single-wavelength [*e.g.* Undas, 2011, and references herein]. Albeit this measurement is said to be characteristic of the thickness of fibrin fibres, it actually resembles the PT-derived fibrinogen assay [29,30], and, therefore is expected to correlate with the fibrinogen level in plasma. On the contrary, the structure of fibrin fibres determined in purified conditions has been shown to be essentially independent of fibrinogen concentration [13,33].

Since fibrin clots formed from mixing purified fibrinogen and thrombin are significantly different from plasma clots, and because the normal range of fibrinogen concentrations is rather narrow (2-4g/L), two types of experiments were performed to compare the performance of fibrinography and turbidity measurements as structural assays. First, we performed fibrinography assays on end-tubes from patients obtained at the hematology department. On each sample, the fibrinogen concentration was measured using the Clauss method on a STA-R analyzer (Diagnostica Stago). Coagulation was initiated as described in materials and methods and the OD wavelength spectra were recorded. Then, we converted OD spectra to fibrinograms and determined the maximum number of protofibrils. In parallel, we extracted the maximum turbidity at 540nm (OD_{540}) from the same set of OD spectra.

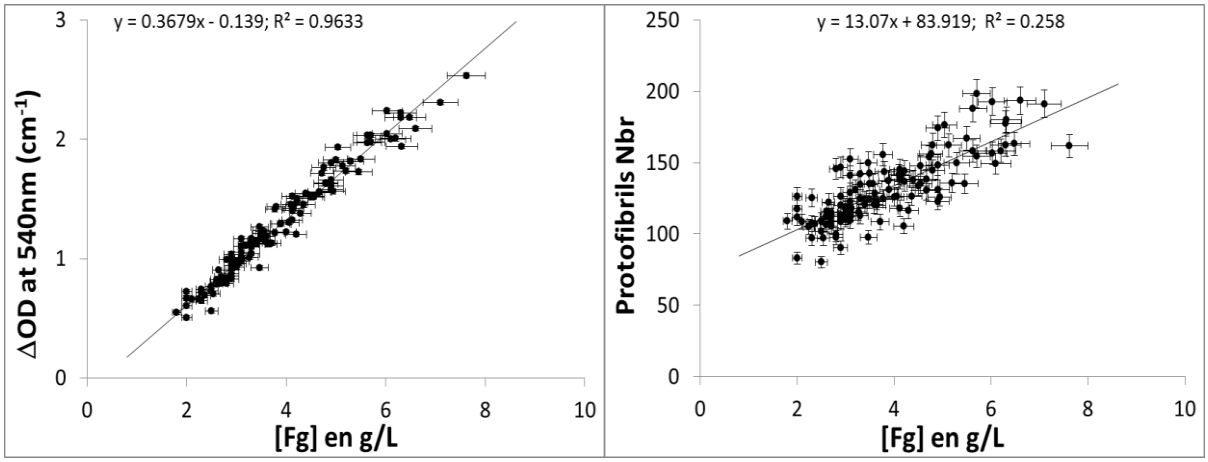

Figure 3 : Evolution of the Optical Density (left) and of the protofibrils number (right) as a function of fibrinogen in patients plasma (N=141).

Figure 3 shows that the behavior of the two measurements differs strongly. The turbidity is proportional to the fibrinogen concentration with an outstanding correlation (R^2=0.96). This result demonstrates that maximum turbidity in plasma clots is not a determinant of fibrin's structure, but measures the fibrinogen concentration with an excellent accuracy as its similarity with the TP-derived fibrinogen assay suggested. In contrast, the number of protofibrils shows a much poorer correlation with fibrinogen concentration (R^2=0.258). Since those experiments are performed on patient's plasma, inflammation or other modifications of the clotting system could be responsible for this weak correlation observed between structure and fibrinogen concentration.

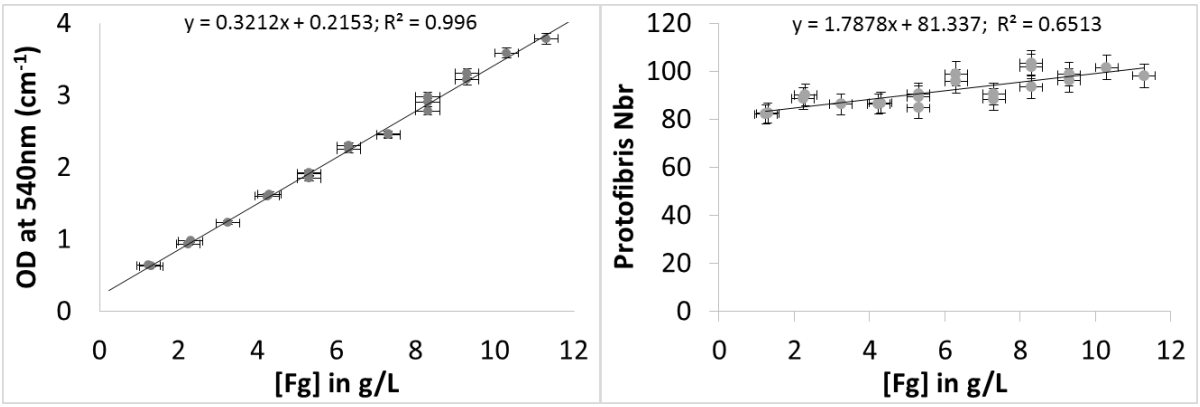

Figure 4 : Comparison of Fibrinography and single-wavelength turbidity for the plasma pool supplemented with different fibrinogen concentrations. Left: optical density vs. fibrinogen concentration. Right: Protofibrils number vs. fibrinogen concentration

To check this possibility, we devised an experiment were the only changing parameter is the fibrinogen concentration. To do that we added varying fibrinogen amounts (Hyphen-biomed, France) to a normal plasma pool, in order to generate a range of plasmas with fibrinogen final concentrations comprised between 1.2 and 11.3g/L. The plasma dilution was held constant at 50% and we checked that thrombin generation was essentially independent of fibrinogen concentration using the CAT assay (supplementary data /data not shown?). Figure 4 shows that the turbidity is proportional to the fibrinogen concentration with a correlation very close to 1. The structure of the fibrin fibres is now almost independent of fibrinogen concentration since the number of protofibrils only increases by 20% when the fibrinogen concentration is increased from 2 to 12g/L, while for patient's plasma it was doubled. This constancy of the structure as a function of fibrinogen concentration is in perfect agreement with the results obtained in purified systems. Indeed, confocal microscopy observations showed that the decrease of pore size with fibrinogen concentration is the consequence of an almost constant number of protofibrils within

fibrin fibres [33]. Similarly, small angle neutron scattering experiments demonstrated directly that the number of protofibrils within the fibres slightly increases with fibrinogen, with exactly the same variation [13].

This proportionality between turbidity and fibrinogen concentration is predicted by the model (eq.1) (see Yeromonahos [14] for details), and taken into account similarly in Carr and Hermans single wavelength method [21] since it is an approximation of our

model. In the experiments with the pooled plasma supplemented with fibrinogen, since the turbidity is proportional to the concentration in fibrinogen, Carr and Herman's method also produce a constant structure as a function of the fibrinogen concentration. To test the relative pertinence of Carr and Herman's assay and Fibrinography, we need a reference structural method and several plasmas with similar fibrinogen levels but different structures. We compare both assays to confocal microscopy in the case of the three control plasmas used above to evaluate the reproducibility of fibrinography.

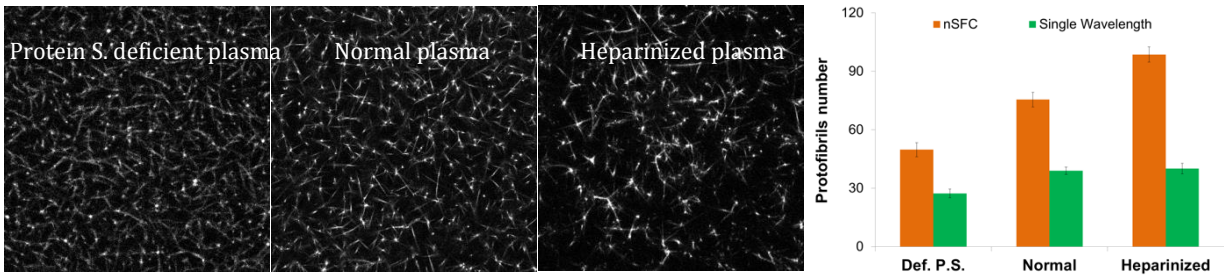

Figure 5 : Comparison of Fibrinography and confocal microscopy for the normal, heparinized and deficient Protein S plasmas. Left: Confocal microscopy images of three plasma. Pore's size increase regularly from right to left. Right: structure determination by photometry. Only our assay gives structural variations compatible with confocal microscopy.

The main observation of Fig. 5 is that the pore size increases fairly regularly from the PS depleted plasma to the normal plasma and to the heparinized one. Since the fibrinogen concentrations are similar in all three plasmas, this pore size increase should translate into an increase in the protofibrils number at the level of fibres to respect the law of mass conservation. Our method shows clearly such a strong increase in protofibrils number (Fig. 3, right panel, orange bars), in good agreement with confocal microscopy. Conversely, Carr's approximation shows no increase in protofibrils number between normal and heparinized plasma, in disagreement with confocal microscopy (Fig. 3, right panel, green bars).

To summarize, we have first demonstrated that single wavelength turbidity measurements determines the fibrinogen content in the tested plasma while Carr' and Herman's single wavelength method [21] is not reliable, as shown previously by Wolberg et al [24]. Indeed, while it takes into account the concentration of fibrinogen, this method uses a thin fibres approximation that is most of the time invalid in plasma. On the contrary, Fibrinography determines structural properties of fibrin fibres that are

in agreement with structural data obtained from several direct methods such as confocal microscopy (present work and Piechoka 2010 [33]), neutron scattering [13], light and X-ray scattering [14,15] and atomic force microscopy [34]. More recently, the validity of fibrinography measurements was confirmed using a direct method (atomic force microscopy) [34].

3.4 Discrimination capacity compared to the CAT assay

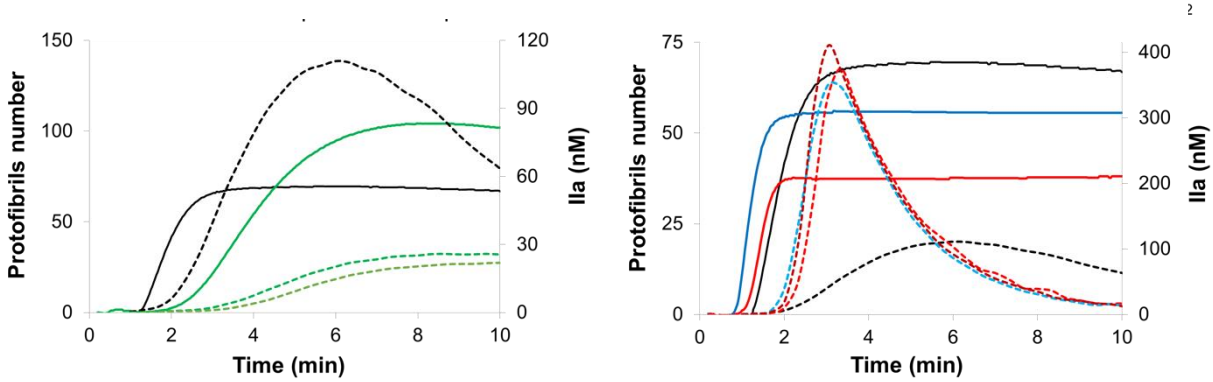

Figure 6 : Left: Comparison of Fibrinography and TG for the normal and hypocoagulant plasma. Continuous line: protofibrils number; dashed line: CAT. Black curves: normal plasma; Green curves: Heparinized plasma.

Right: Comparison of Fibrinography and TG with normal and hypercoagulant plasmas. Continuous line: protofibrils number; dashed line: CAT. Black curves: normal plasma; Blue curves: Def. TFPI plasma; Red curves: Def. PS

To evaluate the discrimination capacity of Fibrinography, we compare Fibrinograms to thrombin generation, both performed in identical conditions for plasmas, tissue factor, phospholipids, and calcium final concentrations.

Figure 6 (left) shows that both assays discriminate clearly normal and hypocoagulant (heparinized) plasmas within 10 minutes. As shown in Table I, the heparinized plasma has 35% more protofibrils per fibre than the normal one. We then compared two hypercoagulant plasmas (deficient in TFPI or in Protein S) to the normal one using Fibrinography and CAT assays. The CAT assay does not discriminate the two hypercoagulant plasmas, while discriminating them from the normal one. Fibrinography clearly discriminates the final structures of all plasmas. Indeed, the final number of protofibrils differs by ~20% between each plasma, well above the CVs of the assay. Moreover, this discrimination was obtained within the first four minutes.

In conclusion, we have shown that Fibrinography determines in plasma the proper nanostructural parameters as demonstrated by comparison with confocal microscopy and as previously shown in purified system [14] by comparison with Small Angle X-ray Scattering. Conversely, we also demonstrated that single wavelength turbidimetry is not a proper structural assay. Actually, the maximum optical density of the clot reflects the fibrinogen concentration together with clot structure.

Last but not least, Fibrinography excellent discrimination of hypercoagulant plasmas together with its excellent reproducibility make it a very promising tool to explore coagulation in clinical or research settings and may become the test that Lipets 2015 and Lancé 2015 [5,6] hoped for.

References

1. NICE diagnostics guidance 13. *Detecting, managing and monitoring haemostasis: viscoelastometric point-of-care testing (ROTEM, TEG and Sonoclot systems).* Issued: August **2014.** www.nice.org.uk/dg13 (as accessed in date 23/11/2015)

2. Whiting P, Al M, Westwood M, Corro Ramos I, Ryder S, Nigel Armstrong N, Kate Misso K, Ross J, Severens J, Kleijnen J. *Viscoelastic point-of-care testing to assist with the diagnosis, management and monitoring of haemostasis: a systematic review and cost-effectiveness analysis.* Health Technology Assesment **2015.** Vol 19 ISSN 1366-5278

3. Kozek-Langenecker SA, Afshari A, Albaladejo P, Alvarez Santullano CA, De Robertis E, Filipescu DC, Fries D, Görlinger K, Haas T, Imberger G, Jacob M, Lancé M, Llau J, Mallett S, Meier J, Rahe-Meyer N, Samama CM, Smith A, Solomon C, Van der Linden P, Wikkelsø AJ, Wouters P, Wyffels P. *Management of severe perioperative bleeding. Guidelines from the European Society of Anaesthesiology.* Eur J Anaesthesiol **2013**; 30:270–382

4. Dai Y, Lee A, Critchley LA, White PF. *Does thromboelastography predict postoperative thromboembolic events? A systematic review of the literature.* Anesth Analg. **2009**;108:734-42.

5. Lipets EN, Ataullakhanov FI. *Global assays of hemostasis in the diagnostics of hypercoagulation and evaluation of thrombosis risk.* Thromb J. **2015**;13(1):4.

6. Lancé MD. *A general review of major global coagulation assays: thrombelastography, thrombin generation test and clot waveform analysis*. Thromb J. **2015**;13:1.

7. Lancé MD, Ninivaggi M, Schols SE, Feijge MA, Oehrl SK, Kuiper GJ, Nikiforou M,Marcus MA, Hamulyak K, van Pampus EC, ten Cate H, Heemskerk JW. *Perioperative dilutional coagulopathy treated with fresh frozen plasma and fibrinogen concentrate: a prospective randomized intervention trial.* Vox Sang. **2012**;103:25–34.

8. Bosch Y, Al Dieri R, ten Cate H, Nelemans P, Bloemen S, Hemker C, Weerwind P, Maessen J, Mochtar B. *Preoperative thrombin generation is predictive for the risk of blood loss after cardiac surgery: a research article.* J Cardiothorac Surg. **2013**;8:154.

9. Brummel-Ziedins KE, Wolberg AS. *Global assays of hemostasis.* Curr Opin Hematol. **2014**;21:395–403.

10. Blombäck C, Hessel, Liljeborg, Procyk and Aslund. *Native fibrin gel networks observed by 3d microscopy, permeation and turbidity.* Biochim Biophys Acta **1989**;997(12):96-110.

11. Ali M, Ridger V, Pease R, Howells G, Grant P, Ariens RA and Philippou H. *Establishment of method and image analysis systems to monitor clot formation and FXIII activity in real time using a murine in vivo model of thrombosis.* 21st Int Congress on Fibrinolysis and proteolysis ISFP, Brighton, UK **2012.**

12. Philippou H. *In vivo measurement of FXIII activity and fibrin formation in real time.* SSC Subcommittee ISTH, Liverpool, UK **2012**.

13. Weigandt K, Pozzo D, and Porcar L. *Structure of high density fibrin networks probed with neutron scattering and rheology*. Soft Matter. **2009**;5:4321–4330.

14. Yeromonahos C, Polack B, Caton F. *Nanostructure of the Fibrin Clot* Biophys. J. **2010**; 99(7):2018-27.

15. Yeromonahos C, Marlu R, Polack B, Caton F. *Antithrombin-independent effects of heparins on fibrin clot nanostructure.* Arterioscler Thromb Vasc Biol. **2012**; 32(5):1320-4.

16. Evans PA, Hawkins K, Morris RH, Thirumalai N, Munro R, Wakeman L, Lawrence MJ, and Rhodri Williams P. *Gel point and fractal microstructure of incipient blood clots are significant new markers of hemostasis for healthy and anticoagulated blood.* Blood **2010**;116: 3341-3346

17. Undas A, Ariëns RA. *Fibrin clot structure and function: a role in the pathophysiology of arterial and venous thromboembolic diseases.* Arterioscler Thromb Vasc Biol. **2011**; 31(12):e88-99.

18. Bernocco S, Ferri F, et al. *Polymerization of rod-like macromolecular monomers studied by stopped-flow, multiangle light scattering: set-up, data processing, and application to fibrin formation.* Biophys. J. **2000**;79:561–583.

19. Ferri F, Greco M, et al. *Growth kinetics and structure of fibrin gels.* Phys. Rev. E. **2001**;63:1–3.

20. Ferri F et al. *Structure of fibrin gels studied by elastic light scattering techniques: dependence of fractal dimension, gel crossover length, fiber diameter, and fiber density on monomer concentration.* Phys. Rev. E Stat. Nonlin. Soft Matter Phys. **2002**;66,011913.

21. Carr ME and Hermans, J. *Size and density of fibrin fibres from turbidity*. Macromolecules, **1978**;11:46-50.

22. Casassa, EF. *Light scattering from very long rod-like particles and an application to polymerized fibrinogen*. J Chem Phys. **1955**;23:596-597.

23. Carr ME, and Gabriel DA. *Dextran-induced changes in fibrin fibre size and density based on wavelength dependence of gel turbidity.* Macromolecules. **1980**;1473-1477.

24. Wolberg AS, Gabriel DA and Hoffman M. *Analysing fibrin clot structure using a microplate reader.* Blood Coagul Fibrinolysis. **2002**;13:533-539.

25. Braun PJ, Givens TB, Stead AG, Beck LR, Gooch SA, Swan RJ, Fischer TJ. *Properties of optical data from activated partial thromboplastin time and prothrombin time assays.* Thromb Haemost **1997**;78:1079-1087.

26. Hussain N, Hodson D, Marcus R, Baglin T, Luddington R. *The biphasic transmittance waveform: an early marker of sepsis in patients with neutropenia*. Thromb Haemost. **2008**;100:146-8.

27. Downey C, Kazmi R, Toh CH. *Early identification and prognostic implications in disseminated intravascular coagulation through transmittance waveform analysis.* Thromb Haemost. **1998**;80:65-69.

28. Bakhtiari K, Meijers JC, de Jonge E, Levi M. *Prospective validation of the International Society of Thrombosis and Haemostasis scoring system for disseminated intravascular coagulation.* Crit Care Med **2004**;32:2416-2421.

29. Palareti G, Maccafern M, Manotti C, Tripodi A, Chantarangkul V, Rodeghiero F, Ruggeri M,and Mannucci PM, on behalf of C.I.S.M.E.L. *Fibrinogen Assays: a Collaborative Study of Six Different Methods.* Clin. Chem. **1991**,37/5, 714-719.

30. Mackie IJ, Lawrie AS, Kitchen S, Gaffney PJ, Howarth D, Lowe GD, Martin J, Purdy G, Rigsby P, Rumley A. *A performance evaluation of commercial fibrinogen reference preparations and assays for Clauss and PT-derived fibrinogen.* Thromb Haemost. **2002**;87:997-1005.

31. Hemker HC, Wielders S, Kessels H, Beguin S. *Continuous registration of thrombin generation in plasma, its use for the determination of the thrombin potential*. Thromb Haemost. **1993**;70:617‑24.

32. Dargaud Y et al. *Effect of standardization and normalization on imprecision of calibrated automated thrombography: an international multicentre study*." Brit. J. Haem. **2007**;139(2):303-309.

33. Piechoka IK et al*. Structural hierarchy governs fibrin gel mechanics*. Biophys J. **2010**;98:2281 – 2289.

34. Domingues, M. M., Macrae, F. L., Duval, C., McPherson, H. R., Bridge, K. I., Ajjan, R. A., ... & Ariëns, R. A. (2015). *Thrombin and fibrinogen γ'impact clot structure by marked effects on intrafibrillar structure and protofibril packing*. Blood **2015** 6:652214

Résumé

La formation du caillot de fibrine, processus clé de la coagulation sanguine, implique la polymérisation des monomères de fibrine en un réseau de fibres. Ce réseau contrôle les propriétés mécaniques du caillot et constitue le squelette sur lequel se base la cicatrisation. Si l'influence des conditions de réaction (pH, concentration, …) est bien connue, le rôle de la composition du fibrinogène sur la structure de la fibrine est inexploré. Cet aspect pourrait être important pour les pathologies cardiovasculaires qui présentent toutes une structure de fibrine anormale.

Nous avons étudié la relation entre la composition de plusieurs fibrinogènes et les propriétés structurelles nano- et micro-métriques ainsi que la mécanique des caillots de fibrine. La composition en protéines co-purifiées de ces fibrinogènes a peu d'influence, alors que le profil de polydispersité contrôle la structure multi-échelle de la fibrine. Des mesures de diffusion des rayons x, de spectrophotométrie multi-longueur d'ondes et de microscopie confocale ont mis en évidence que les fibres provenant des fibrinogènes monodisperses sont quasi-cristallines, droites et rigides. Les fibres provenant de fibrinogènes polydisperses sont, elles, beaucoup moins organisées, courbées, avec un module de rigidité faible. Enfin, les propriétés mécaniques de la fibrine a montré que la réponse des caillots aux déformations, aussi que les scenarios de rupture, sont directement liés à sa structure et donc significativement dépendants du profil de polydispersité des fibrinogènes. Ces résultats ouvrent de nouvelles perspectives dans plusieurs domaines, que ce soit pour l'utilisation optimale des fibrinogènes pour les dysfibrinogénémies et hémorragies, mais également pour la reconstruction tissulaire, ainsi que la compréhension du lien entre la structure anormale des caillots et les maladies cardiovasculaires.

Abstract

Fibrin clot formation is one of the major processes leading to blood clotting. It involves the polymerization of fibrin monomers into a network of fibrin fibres. This network controls the mechanical properties of the clot and serves as a skeleton for wound healing. Environmental factors (pH, concentration, …) have been proved to influence polymerization, however the role of fibrinogen composition on the structure of fibrin remains unexplored. This aspect might be important for the case of cardiovascular pathologies, which present abnormal fibrin structures.

We have determined the relation between different sources of fibrinogen with the nano- and micro-metric structural and mechanical properties of fibrin clots. The composition in co-purified proteins of the fibrinogens has no significant importance, however the polydispersity profile controls the multiscale properties of fibrin. Indeed, x-ray scattering, multi-wavelength spectrophotometry and confocal microscopy measurements have proved that fibres from monodisperse fibrinogens are quasi-crystalline, straight and rigid. Fibres from polydisperse fibrinogens are less organised, curbed and less rigid. Finally, the mechanical properties of fibrin showed that the response of clots to deformation, as well as the scenarios of rupture are closely related to the structure, and consequently related to the profiles of polydispersity. This opens outstanding perspectives in many fields such the optimisation of fibrinogen's use on dysfibrinogenemies or haemorrhage, tissue regeneration or the understanding between the abnormal structure of clots and cardiovascular diseases.